การสังเคราะห์และประสิทธิภาพการเร่งปฏิกิริยาเชิงแสงภายใต้แสงช่วงที่ตามองเห็นของวัสดุเชิงประกอบฐานบิสมัทออกซีโบรไมด์

นางสาวตวงพร ประสิทธิกุล

วิทยานิพนธ์นี้เป็นส่วนหนึ่งของการศึกษาตามหลักสูตรปริญญาวิทยาศาสตรมหาบัณฑิต
สาขาวิชาเทคโนโลยีเซรามิก ภาควิชาวัสดุศาสตร์
คณะวิทยาศาสตร์ จุฬาลงกรณ์มหาวิทยาลัย
ปีการศึกษา 2559

SYNTHESIS AND PHOTOCATALYTIC EFFICIENCY UNDER VISIBLE LIGHT OF BiOBr-BASED COMPOSITES

Miss Tuangphorn Prasitthikun

A Thesis Submitted in Partial Fulfillment of the Requirements
for the Degree of Master of Science Program in Ceramic Technology
Department of Materials Science
Faculty of Science
Chulalongkorn University
Academic Year 2016

Thesis Title	SYNTHESIS AND PHOTOCATALYTIC EFFICIENCY UNDER VISIBLE LIGHT OF BiOBr-BASED COMPOSITES
By	Miss Tuangphorn Prasitthikun
Field of Study	Ceramic Technology
Thesis Advisor	Assistant Professor Pornapa Sujaridworakun, D.Eng.
Thesis Co-Advisor	Professor Tsugio Sato, Ph.D.
	Charusporn Mongkolkachit, Ph.D.

Accepted by the Faculty of Science, Chulalongkorn University in Partial Fulfillment of the Requirements for the Master's Degree

.....Dean of the Faculty of Science
(Associate Professor Polkit Sangvanich, Ph.D.)

THESIS COMMITTEE

.....Chairman
(Assistant Professor Dujreutai Pongkao Kashima, D.Eng.)

.....Thesis Advisor
(Assistant Professor Pornapa Sujaridworakun, D.Eng.)

.....Thesis Co-Advisor
(Professor Tsugio Sato, Ph.D.)

.....Thesis Co-Advisor
(Charusporn Mongkolkachit, Ph.D.)

.....Examiner
(Jiaqian Qin, Ph.D.)

.....External Examiner
(Siriporn Larpkiattaworn, Ph.D.)

ตวงพร ประสิทธิกุล : การสังเคราะห์และประสิทธิภาพการเร่งปฏิกิริยาเชิงแสงภายใต้แสงช่วงที่ตามองเห็นของวัสดุเชิงประกอบฐานบิสมัทออกซีโบรไมด์ (SYNTHESIS AND PHOTOCATALYTIC EFFICIENCY UNDER VISIBLE LIGHT OF BiOBr-BASED COMPOSITES) อ.ที่ปรึกษาวิทยานิพนธ์หลัก: ผศ. ดร.พรนภา สุจริตวรกุล, อ.ที่ปรึกษาวิทยานิพนธ์ร่วม: ศ. ดร.ซึกิโอะ ซาโต้, ดร.จรัสพร มงคลขจิต, 97 หน้า.

งานวิจัยนี้มีวัตถุประสงค์ในการปรับปรุงประสิทธิภาพของตัวเร่งปฏิกิริยาเชิงแสงภายใต้แสงช่วงที่ตามองเห็นของวัสดุที่มีบิสมัทออกซีโบรไมด์เป็นฐาน เนื่องจากวัสดุบิสมัทออกซีโบรไมด์เป็นตัวเร่งปฏิกิริยาที่มีแถบช่องว่างพลังงานที่แคบสามารถตอบสนองต่อแสงในช่วงที่ตามองเห็นและมีประสิทธิภาพสูงในการย่อยสลายสารอินทรีย์ที่เป็นพิษ แต่อย่างไรก็ดีจากงานวิจัยที่ผ่านมาพบว่าอนุภาคของบิสมัทออกซีโบรไมด์ที่เตรียมขึ้นมีการกลับมารวมตัวกันอย่างรวดเร็วของอิเล็กตรอนและโฮล ส่งผลให้ประสิทธิภาพการเกิดปฏิกิริยาย่อยสลายเชิงแสงที่ได้ยังไม่สูงเท่าที่ควร จึงมีแนวทางในการแก้ปัญหาดังกล่าวโดยการนำตัวเร่งปฏิกิริยาเชิงแสงชนิดนี้มาเตรียมเป็นวัสดุเชิงประกอบร่วมกับวัสดุอื่นที่มีสมบัติช่วยส่งเสริมการแยกตัวกันของประจุทั้งสอง ได้แก่ กราฟีนออกไซด์ กราฟีนที่ผ่านการรีดิวซ์ และกราฟิติกคาร์บอนไนไตรด์ โดยทำการศึกษาหาสภาวะการเตรียม และสัดส่วนของวัสดุเชิงประกอบที่เหมาะสม

จากผลการศึกษาพบว่าการนำบิสมัทออกซีโบรไมด์ไปเตรียมเป็นวัสดุเชิงประกอบร่วมกับกราฟีนออกไซด์ กราฟีนที่ผ่านการรีดิวซ์ และกราฟิติกคาร์บอนไนไตรด์ ช่วยส่งเสริมประสิทธิภาพการเป็นตัวเร่งปฏิกิริยาเชิงแสงภายใต้แสงช่วงที่ตามองเห็นเมื่อเทียบกับบิสมัทออกซีโบรไมด์ชนิดเดียว โดยปริมาณที่เหมาะสมของวัสดุทั้งสามชนิดในวัสดุเชิงประกอบนั้นเป็นปัจจัยสำคัญต่อการส่งเสริมประสิทธิภาพ ซึ่งวัสดุเชิงประกอบที่ให้ประสิทธิภาพในการย่อยสลายสีย้อมโรดามีนบีและแก๊สไนโตรเจนออกไซด์ที่ดีที่สุดคือ วัสดุเชิงประกอบระหว่างบิสมัทออกซีโบรไมด์กับกราฟิติกคาร์บอนไนไตรด์ที่ปริมาณ 2 เปอร์เซ็นต์โดยน้ำหนัก ซึ่งมีประสิทธิภาพที่สูงกว่าการเตรียมด้วย กราฟีนที่ผ่านการรีดิวซ์ และกราฟีนออกไซด์ตามลำดับ นอกจากนี้ยังพบว่าการเตรียมเป็นวัสดุเชิงประกอบทั้งสามชนิดช่วยเพิ่มเสถียรภาพการเกิดปฏิกิริยาในการนำกลับไปใช้งานซ้ำของตัวเร่งปฏิกิริยาเชิงแสงเมื่อเทียบกับบิสมัทออกซีโบรไมด์ โดยการเตรียมเป็นวัสดุเชิงประกอบกับกราฟิติกคาร์บอนไนไตรด์คงประสิทธิภาพการย่อยสลายโรดามีนบีและไนโตรเจนออกไซด์แก๊สได้สูงที่สุดเมื่อเทียบกับกราฟีนที่ผ่านการรีดิวซ์ และกราฟีนออกไซด์ หลังจากการทดสอบการนำไปใช้ซ้ำสามครั้ง

จากการศึกษานี้แสดงให้เห็นว่าวัสดุเชิงประกอบโฟโตคะตะลิสต์ที่มีบิสมัทออกซีโบรไมด์เป็นฐานทั้งสามชนิดที่เตรียมขึ้นมีศักยภาพในการนำไปประยุกต์ใช้ในการช่วยบำบัดมลพิษทางน้ำและอากาศต่อไป

ภาควิชา วัสดุศาสตร์	ลายมือชื่อนิสิต .....
สาขาวิชา เทคโนโลยีเซรามิก	ลายมือชื่อ อ.ที่ปรึกษาหลัก .....
ปีการศึกษา 2559	ลายมือชื่อ อ.ที่ปรึกษาร่วม .....
	ลายมือชื่อ อ.ที่ปรึกษาร่วม .....

5771991623 : MAJOR CERAMIC TECHNOLOGY
KEYWORDS: BIOBR-BASED COMPOSITES / PHOTOCATALYTIC ACTIVITY / GRAPHENE OXIDE / REDUCED GRAPHENE OXIDE / GRAPHITIC CARBON NITRIDE / VISIBLE LIGHT RESPONSIVE

TUANGPHORN PRASITTHIKUN: SYNTHESIS AND PHOTOCATALYTIC EFFICIENCY UNDER VISIBLE LIGHT OF BiOBr-BASED COMPOSITES. ADVISOR: ASST. PROF. PORNAPA SUJARIDWORAKUN, D.Eng., CO-ADVISOR: PROF. TSUGIO SATO, Ph.D., CHARUSPORN MONGKOLKACHIT, Ph.D., 97 pp.

This research aimed to improve the photocatalytic activity under visible light of BiOBr-based composites. Due to its narrow band gap energy which can be responded to visible light and good performance for decomposition of harmful organic contaminants, BiOBr becomes one of the promising candidate photocatalysts. Anyhow, the easy recombination of generated electron and hole limited its photocatalytic efficiency. To solve this problem, BiOBr hybriding with other materials such as graphene oxide (GO), reduced-graphene oxide (rGO) and graphitic carbon nitride (g-C_3N_4) that can enhance charge carriers separation was proposed.

From this study, it was found that the enhanced photocatalytic activity of BiOBr was successfully achieved by hybriding with GO, rGO and g-C_3N_4. The amount of these 3 materials in the composites had played an important role on their photocatalytic efficiency. The highest photocatalytic degradation of Rh-B and nitrogen oxide gas was obtained from BiOBr/ g-C_3N_4 with 2wt%, which was higher than that of other composites and pure BiOBr. Moreover, these BiOBr-based composites showed high photocatalytic stability after 3 cycles reusing for Rh-B and NO_x degradation, in that the BiOBr/ g-C_3N_4 with 2wt% exhibited the highest reused stability followed by BiOBr/rGO, BiOBr/GO and BiOBr, respectively.

As the results, it can be proposed that the BiOBr-based composites synthesized in this study would be promising visible-light responsive photocatalyst materials for water and air purifications in future.

Department:	Materials Science	Student's Signature	.....
Field of Study:	Ceramic Technology	Advisor's Signature	.....
Academic Year:	2016	Co-Advisor's Signature	.....
		Co-Advisor's Signature	.....

ACKNOWLEDGEMENTS

Foremost, I would like to express my sincere gratitude to my adviser, Asst. Prof. Dr. Pornapa Sujaridworakun a wise and always helpful mentor. This thesis would not have been possible without her guidance, kindness, patience, motivation and support. Her comments and suggestion always broaden the perspective in practical applications as well.

I would like to thank the chairman, Asst. Prof. Dr. Dujreutai Pongkao Kashima and other committee members, Dr. Jiaqian Qin and Dr. Siriporn Larpkiattaworn members of thesis committee for many valuable comments and their perceptive suggestions.

I would like to gratefully acknowledge my co-adviser Dr. Charusporn Mongkolkachit, who provide an opportunity to receive the valuable financial support of the Thailand Graduate Institute of Science and Technology (TGIST, TG-33-09-58-024M), National Science and Technology Development Agency (NSTDA).

I would like to express my thankfulness to the invaluable professional advice and support of my co-advisor Prof. Dr. Tsugio Sato, who has kindly give me very useful suggestions and support in characterization of gas decomposition and experimental experience at Institute of Multidisciplinary Research for Advanced Materials, Tohoku University, Japan and JASSO Student Exchange Support program scholarship for 3 months. I also thankful to Prof. Dr. Shu Yin and Dr. Xiaoyong Wu for insightful comments during every group meeting and for great technical support.

I would like to acknowledge the Ratchadaphiseksomphot Endowment Fund 2015 of Chulalongkorn University (CU-58-043-AM) and the Ratchadaphiseksomphot Endowment Fund 2016 of Chulalongkorn University (CU-59-034-AM) for granting research grants.

I would like to thank all my colleagues and staff members in Department of Materials Science, Faculty of Science, Chulalongkorn University for their friendship and encouragement.

Finally and most importantly, I would like to dedicate this work and effort to my family. I am always going to be eternally grateful to my parents for their unconditional love, irreplaceable moral support and spiritual guidance throughout my life.

CONTENTS

Page

Page

Page

Page

Page

LIST OF TABLES

Page

LIST OF FIGURES

Page

CHAPTER I

INTRODUCTION

1.1. Background and motivation

Nowadays, a wide variety of organic pollutant sources such as industrial, agricultural and chemical spills, including the world population growth have increased the environment pollution, both of air and water, caused by hazardous wastes which is a serious problem in the world.

Currently, the semiconductor-based photocatalytic technology is one of the most promising technologies for the solar energy utilization and purification of various organic pollutants in the environment. Photocatalytic technologies have attracted a large attention owing to their wide applications in decomposing organic compounds for environmental remediation, clean energy production, water splitting, and CO_2 reduction [1-4]. The process of the photocatalytic reaction occurs as follows: when a semiconductor is exposed to the light containing the energy being equal to or larger than the band gap of semiconductor and absorbs a photon, the electron will be excited from the valence band to the conduction band. The activation of the electrons results in the generation of ''holes'' (electron vacancy) in the valence band. In this reaction, h^+ and e^- are the powerful oxidizing and reducing agents, respectively [5].

The most widely used photocatalyst in the past was TiO_2, but this photocatalyst only reacts with ultraviolet (less than 5% of solar light), which limits the application of TiO_2. Thus, there was an attempted to invent and develop photocatalyst materials that can respond to visible light because the visible-light (400 nm $<\lambda<$ 800 nm) occupies the main part of the solar spectrum (accounting for 43% energy in solar spectrum). So, the Visible-light-driven photocatalysts have been receiving attention to harvest the solar energy efficiently [6, 7].

Recently, BiOBr has attracted considerable attention for its potential applications in energy and environment fields due to its unique physical and chemical properties, such as typical nanostructures/ micro- morphologies, optical properties, suitable band gap, high stability, low- cost, etc[8, 9]. Anywise, BiOBr shows the rapid recombination of electrons and holes pairs, which limits its further improvement in photocatalytic activity [10]. Thus, many researches have been attempted to solve this problem by various approaches. Very recently, some carbon- based nano- materials, such as graphene oxide (GO), reduced graphene oxide (rGO) and graphitic carbon nitride (g-C_3N_4), etc. have attracted great interests in fundamental and applied science owing to their fascinating intrinsic properties, such as extremely high electron mobility, high flexible structure, large specific surface area, special micro- morphology and amenable ability to electrochemical modifications [11, 12]. They have been applied to decorate photocatalysts such as Pt/g-C_3N_4 CdS/g-C_3N_4 g-C_3N_4/TiO_2 CdS/Au/g-C_3N_4 etc., which can significantly enhance the photocatalytic performance.

Various synthesis processes have been applied to synthesize photocatalyst materials with different morphologies and size such as hydro- solvothermal, sol- gel, microwave- assisted hydrothermal, chemical vapor deposition, thermal deposition, spray pyrolysis, chemical precipitation. Among these methods, precipitation was the most widely used for the synthesis of fine metal oxide powders because of its simplicity and reproducibility with possibility for large scale production. Moreover, considering about the energy usage, the low temperature precipitation synthesis process was concerned.

Herein, we aimed to synthesize and enhance the photocatalytic activity of BiOBr by hybriding with graphene oxide (GO), reduced graphene oxide (rGO) and graphitic carbon nitride (g- C_3N_4) by precipitation process, and find the optimum preparation conditions to achieve the excellent photocatalytic activity for the nitrogen oxide gas and dye decomposition under visible light irradiation.

1.2. The objective of this research

To synthesize of high efficiency visible-light responsive BiOBr-based composite photocatalysts.

1.3. Expected result

Obtain the excellent photocatalytic activity of the visible-light responsive BiOBr-based composite photocatalyst.

CHAPTER II

LITERATURE REVIEW

2.1 The photocatalytic process

2.1.1 Process and models [13]

Initially, titanium dioxide has been proven as one of the most promising photocatalyst due to its excellent properties such as high oxidation efficiency, high chemical stability and environmental friendly. Moreover, TiO_2 has been used in several applications such as solar cells, transistors, sensor and photocatalyst for cleaning waste water and air pollution.

Photocatalytic process is invented by Fujishima in 1972, when a semiconductor is exposed to the light containing the energy being equal to or larger than the band gap of semiconductor and absorbs a photon, the electron will be excited from the valence band to the conduction band. The activation of the electrons results in the generation of ''holes'' (electron vacancy) in the valence band. In this reaction, h^+ and e^- are the powerful oxidizing and reducing agents, respectively. The products of this process are carbon dioxide (CO_2) and water (H_2O) as shown in Fig 2.1. The principal components of photocatalytic process are as follow:

1) Light energy
2) Catalyst
3) Water
4) Oxygen

The photocatalytic reaction will be activated by photon energy, the photon energy (E) can be calculated by using Planck's equation [14].

$$\boldsymbol{E = h\nu = \frac{hc}{\lambda}} \qquad \text{(Equation 2.1)}$$

When: **E** is photon energy, eV or J

h is Planck's constant = 6.625 x 10^{-34} J·s

ν is light frequency, s^{-1}

λ is light wave length, nm

c is light velocity = 2.997x 10^{8} m/s

The basic of photocatalytic process can be explained as follows, when the light containing the energy being equal to or larger than the band gap of semiconductor, the electron will be excited from the valence band to the conduction band (e^-_{cb}) and generated holes (electron vacancy) in the valence band (h^+_{vb}) of semiconductor as shown in reaction below:

$$Semiconductor\ (photocatalyst) + h\nu \rightarrow e^-_{cb} + h^+_{vb} \quad \text{(Equation 2.2)}$$

Electron can be reacted with oxygen (O_2) to generate super oxide radical (O_2^-) and super oxide radical was changed to hydrogen peroxide when it reacted with water. Then hydrogen peroxide can be changed to super hydroxyl radical as shown in reactions below:

$$e^-_{cb} + O_2 \rightarrow O_2^- \quad \text{(Equation 2.3)}$$

$$O_2^- + 2H_2O \rightarrow 2H_2O_2 \quad \text{(Equation 2.4)}$$

$$2H_2O_2 \rightarrow 2OH^- \quad \text{(Equation 2.5)}$$

Hole (h^+) can be reacted with water (H_2O) and hydroxyl group (OH^-) converting to hydroxyl radical ($OH^\bullet$) as shown in reactions below:

$$h^+_{vb} + H_2O \rightarrow OH^\bullet + H^+ \quad \text{(Equation 2.6)}$$

$$h^+_{vb} + OH^- \rightarrow OH^\bullet \quad \text{(Equation 2.7)}$$

Super oxide radical and hydroxyl radical from this process have efficiency to decompose various organic compounds to carbon dioxide and water, which are not dangerous to environment.

However the photocatalytic performance has been limited due to the high recombination rate of electron and hole pair as shown in reactions below:

$$e_{cb}^{-} + h_{vb}^{+} \rightarrow Semiconductor\ (photocatalyst) + heat \qquad \text{(Equation 2.8)}$$

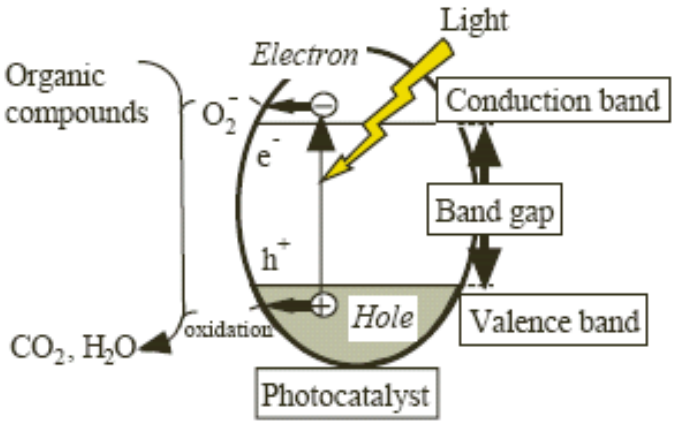

Fig. 2.1 Photocatalytic mechanism [13]

2.1.2 Parameter affecting the photocatalytic activity

The photocatalytic efficiency depends on various operation parameters such as light intensity, pH of aqueous solution, oxygen concentration in system, but the main parameters affecting on the photocatalytic efficiency are particle size, surface area and crystallinity of photocatalyst, the details are as follows:

- **Particle size**

In typical, the small diameter particle size results in higher photocatalytic efficiency because it has a large surface area, which will increase the adsorption ability of photocatalyst. However, the small diameter particle size encourages the recombination of electron-hole pair due to there is too narrow space to separate the electron-hole pair.

- **Surface area and crystallinity**

The large surface area and high crystallinity are the important factors to affecting photocatalytic efficiency because increasing the crystallinity of photocatalyst materials can reduce the recombination of electron-hole pair probability and the large surface area can increase the adsorption ability of organic molecule on surface area of photocatalyst surface. But, the large surface area always has many defects of crystalline, which brings to the lower photocatalytic efficiency.

2.2. Environmental application of photocatalyst

Presently, energy production, consumption, and environmental pollution problems become more serious. As a green technology to solve these problems, the semiconductor photocatalyst has been increased attention and also has been widely used in many fields such as water and air purification, food, medicine, cosmetics, energy conversion, etc. The applications of photocatalyst about water decontamination, air purification, water splitting and self-cleaning have been briefly introduced as follows.

2.2.1 Water decontamination

Recently, lack of safe drinking water, inadequate sanitation and poor hygiene are becoming a big problem owing to rapid industrial growth, environmental pollution, global warming causing abnormal climate changes, depleted water resources, and uncontrolled groundwater development. These issues are becoming a factor that is threatening human health and the environment [15]. Herein, many of methods such as filtration, sedimentation, distillation, slow sand filters, biologically active carbon, flocculation, photocatalysis, etc. have been employed to purify contaminated water. Due to the low cost, environmentally benign and high efficiency, the photocatalysis has attracted a lot of interest over other methods. So research on water decontamination by semiconductor photocatalysis has been enormously carried out [16].

2.2.2 Air purification

Nowadays, the air pollution both of outdoor and indoor has become of the most serious environmental problems in human daily life and much has been paid to control or relieve this issue. The outdoor air pollution are varied and include both natural and man-made such as volcanoes, oceans, biological decay, lightning strikes, forest fires, burning of fossil fuels (oil, coal and gas) from industries, power stations, homes and road vehicles. The air pollutant substances mainly consist of nitrogen oxides, carbon monoxide, sulphur dioxide, volatile organic compounds (VOCs) and etc. [17] The photocatalysis as a green chemical method is still a promising technology for air pollution treatment, albeit many of methods have been offered to treat this outdoor air pollution, owing to its high efficiency for deal with various kinds of toxic gases such as car exhausts NO_x, SO_x, VOCs, etc., low cost, simple treatment, environmentally benign.

2.2.3 Water splitting

The energy depletion has been essential issue in recent times and a renewable of energy source is strongly required [18]. Since Honda–Fujishima effect generated hydrogen by water photo-electrolysis, the hydrogen fuel by solar-chemical energy conversion has been slowly considered as a promising choice for environmentally friendly and renewable energy source, which can be produced from water without the release of CO_2 and other toxic gas.

2.2.4 Self-cleaning

Self-cleaning technology has been inspired from the wings of butterflies and the leaves of lotus from hydrophobic property. The self-cleaning surface coating has been widely applied in many areas such as cement, glass coatings, paints, textiles, building, etc. due to its labor-saving. Especially, combined coating with photocatalyst attracts the increasing interest owing to multi-function.

2.3 Disadvantages (Limitations)

2.3.1 Recombination of electron-hold

Generally, the photocatalytic process was excited by photon, which generated electron to conduction band (e_{cb}^-) and left hole in valence band (h_{vb}^+). In electron and hole recombination process, occur by dropping of the electron across band gap energy to recombine with the hole, that resulting decrease the photocatalytic efficiency [19].

Furthermore, this process occurs in the topic of direct and indirect band gap recombination of semiconductors this can be explained as follows: Direct band gap semiconductors, the minimal-energy state of the conduction band and maximal-energy state of valence band have the same momentum (k), which promotes the recombination of electron and hole. Indirect band gap semiconductors, the minimal-energy state of the conduction band and maximal-energy state of valence band have the different momentum (k), the recombination of electron and hole is more difficult to occur due to the minimal-energy state of the conduction band is not at the same k as maximal-energy state of valence band, its requires a momentum change (Δk) for charge transfer as shown in Fig.2.2.

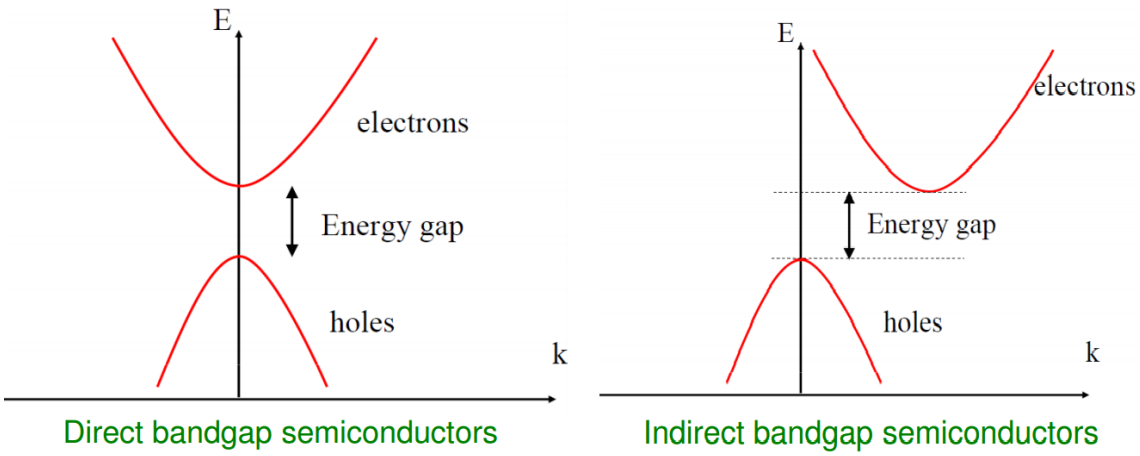

Fig. 2.2 Energy diagram of semiconductors [20]

2.3.2 Absorption of the light

Originally, TiO_2 is the most widely used photocatalyst, which works only with the ultraviolet that is only 4% of the solar spectrum and thus limits its practical applications. Therefore, developing visible light response photocatalysts has recently become one of the focuses in the photocatalysis researches due to the visible-light (400 nm <λ< 800 nm.) occupies the main part of the solar spectrum (accounting for > 43% energy in solar spectrum) as shown in Fig 2.3. Visible-light-driven photocatalysts have been received attention to utilize the solar energy efficiently [21].

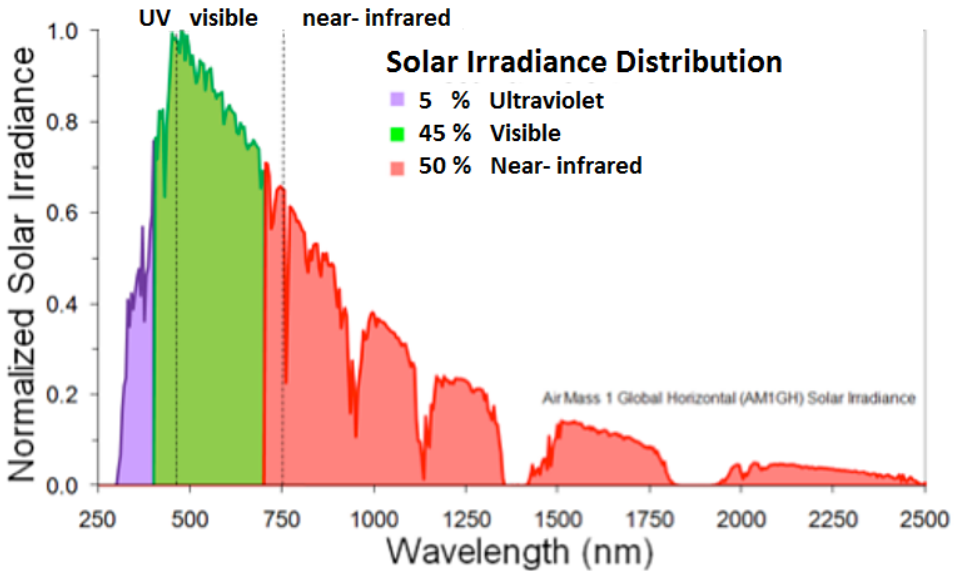

Fig. 2.3 Energy wavelength of light diagram [22]

2.4 Improving photocatalytic reaction

Nowadays, photocatalysts have been developed for solving environmental and energy issues. Nevertheless, the photocatalytic efficiency and light-harvesting ability are still far away from real application. Therefore, large amounts of strategies such as doping, noble metal plasmon, cocatalyst loading, sensitizing and coupling with other semiconductors, etc. have been proposed for improving the performance as much as possible [23]. The followings will give a brief review for doping and coupling with other semiconductors.

2.4.1 Doping

For fully utilize the solar energy, great attempt has been studied to enhancing photocatalytic performance in visible light region. Doping with non-metal ions such as N, C, S, B, P, etc. or metal ions such as Ag, Au, W, Fe, etc. has been widely used to improve photocatalytic activity under visible light irradiation. This method tends to narrow the band gap energy, increases the electron-hole pair separation and inhibits the recombination of electron-hole pair [23, 24].

- **Nonmetal doping**

From literature[25], non-metal ions doping can create a middle-gap state acting as an electron donor or acceptor in the band gap of TiO_2, which introduces lower band gap and shifts the optical absorption of TiO_2 into the visible-light region. Non-metal doping such as C-doped TiO_2 can enhancing the visible light photocatalytic efficiency of TiO_2 by incorporation of additional components in the TiO_2 structure as show in Fig 2.4.

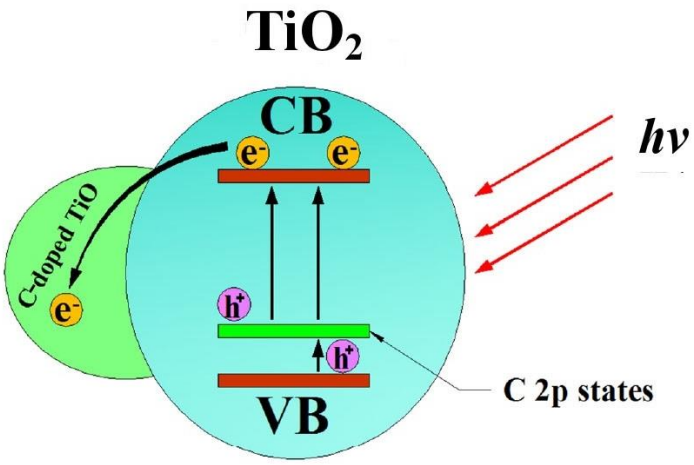

Fig. 2.4 Photocatalysis mechanism of the C-doped TiO_2 under visible-light irradiation [26].

- **Metal doping** [27]

Metal doping is a potential way for the improvement of visible-light driven photocatalysis since metal doping can extend the absorption range of light, increase the photo-induced radicals and reduced the recombination rate of photogenerated electron-hole pairs [28]. W, Nd, Ta, Nb, Fe, Bi, V and Cr, etc. have been common used metal doping elements, but among them, Bi and Fe have attracted the special interest in enhancing visible light responsive photocatalytic performance [29]. The study of Fe doped TiO_2 nanoparticles fabricated by a hydrothermal method. The particles were used to check the photo-activity of para-nitrophenol with the visible light irradiation. After Fe doping, the TiO_2 was capable for the visible light absorption by introducing some impurity levels above the valence band of TiO_2 (as seen in Fig. 2.5). In addition, the band gap energy of TiO_2 could be obviously adjusted by the Fe doping content.

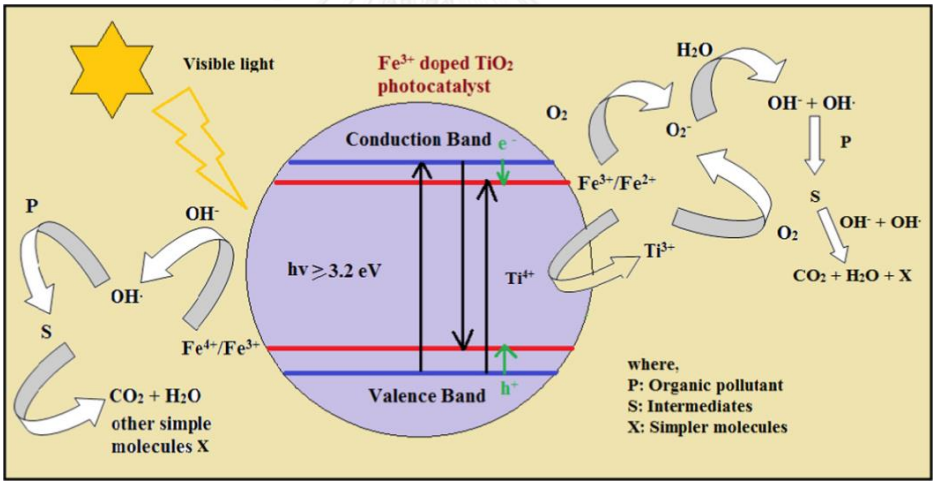

Fig. 2.5 Photocatalysis mechanism of the Fe-doped TiO_2 nanoparticles under visible-light irradiation [27].

- **Oxygen rich** [30]

The induction of oxygen rich in photocatalyst is also a promising way for enhance the visible light driven photocatalyst performance. For example, synthesis the oxygen rich TiO_2 via the addition of H_2O_2n and found that the valence band maximum of TiO_2 could be upward shifted owing to the existence of excessive oxygen. In this case, the band gap could be narrowed by controlling the amount of excessive oxygen in TiO_2 (as seen in Fig. 2.6).

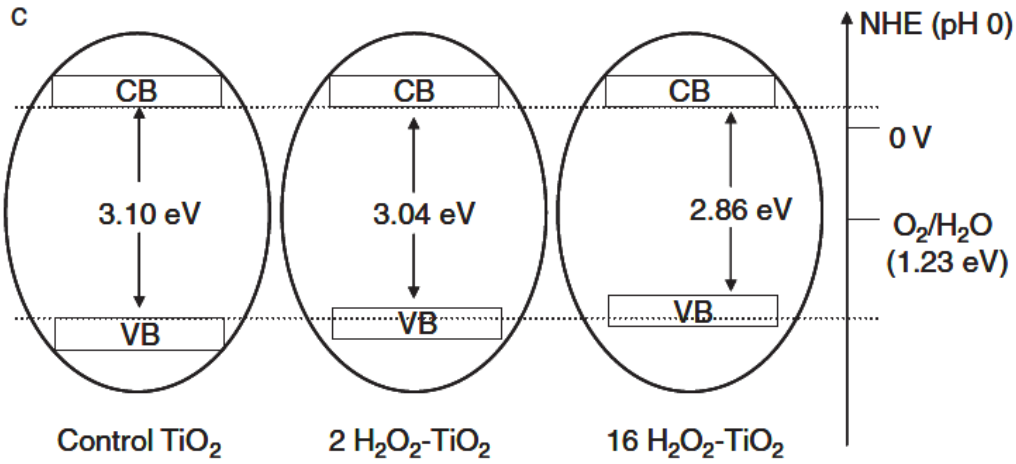

Fig. 2.6 Mechanism of band gap narrowing of oxygen rich TiO_2

2.4.2 Coupling with other semiconductors [31]

Coupling with other semiconductors to improve separation of the electron-hole pair and extend the absorption wavelength of photocatalyst into visible-light region of the solar spectrum. This approach can improve the photocatalytic efficiency. It has been reported that good matching of the conduction and valence bands of two semiconductors could enable efficient charge carrier transfer from one to another. Wide band gap energy of TiO_2 coupling with small band gap semiconductor such as CdS could result in the formation of heterojunctions, the photogenerated the electron transfer from small band gap semiconductor with higher conduction band to another semiconductor with a lower conduction band as show in Fig. 2.7, which can extend photo response to visible light region and reduce of recombination of electron-hole pair.

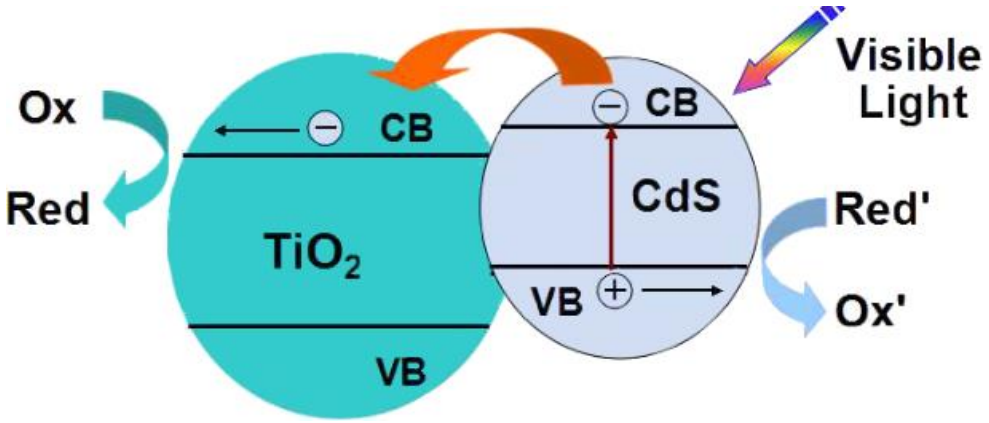

Fig. 2.7 Photocatalytic mechanism of composite semiconductor under sunlight or visible light irradiation [32]

2.5 Bismuth oxybromide (BiOBr)

2.5.1 Physical and chemical properties

Bismuth oxybromide (BiOBr) as a p-type semiconductor, which is known that BiOBr has drawn considerable attention for its shows high photocatalytic activity[33], non-toxicity, facile preparation, chemical stability in photocatalytic oxidation process[34] and it has suitable band gap energy (between 2.64 to 2.91eV) [35-38] for response to visible light in the photocatalytic process.

BiOBr has the unique electrical, optical and photocatalytic activity because of its crystalline layer and structure. The internal electric fields in layered crystalline will promote the charge separation, which can induce redox reactions on the surface of the semiconductor. BiOBr has crystallizes in tetragonal structure that consists of $[Bi_2O_2]$ positive slabs, which are interleaved by double slabs of bromide to form $[Bi_2O_2Br_2]$ layers along the c axis. The permanent static electric fields between $[Bi_2O_2]$ and $[Br_2]$ layers can separate the electron–hole pairs thereby enhancing the photocatalytic activity of these materials (as show in Fig 2.8). [39]

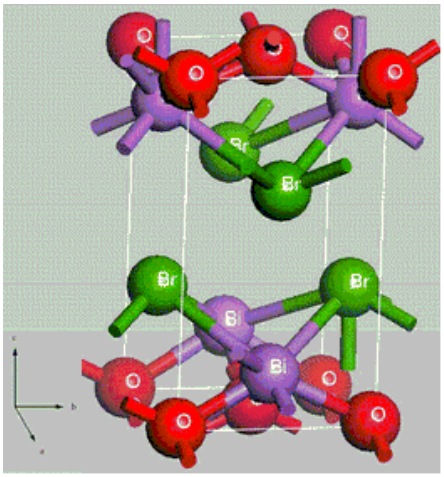

Fig 2.8 Bismuth oxybromide (BiOBr) structure

2.5.2 Applications

BiOBr is a flexible and extensively applicable photocatalyst for environmental applications such as wastewater treatment, air pollution control and splitting of water into hydrogen and oxygen. However, the majority of works published focus on the utilization of BiOBr for water treatment processes.

2.5.3 Disadvantages (Limitations)

Although BiOBr offers high photocatalytic activity, but in some case, BiOBr shows the rapid recombination of photo-generated electrons and holes pairs, and it is easy to deteriorate photocatalyst with light and heat which restricts its further improvement in photocatalytic activity [10]. The considerable efforts have been made to improve its properties by introducing different chemical variations.

2.6 Graphene oxide (GO), Reduce graphene oxide (rGO), Graphitic carbon nitride (g-C_3N_4)

2.6.1 Physical and chemical properties

- **Graphene oxide (GO) and Reduce graphene oxide (rGO)** [40]

From graphite oxide to graphene oxide: The graphite is a 3 dimensional carbon based material compose of millions of layers of graphene. The oxidation process by using strong oxidizing agents can transform graphite to graphite oxide. The oxidization of graphite reduced the mean size and gives unsatisfied property by produced the oxygen functionalities in the graphite structure. This expands the layer separation and makes the graphite oxide is hydrophilic. The hydrophilic property of graphite oxide make it can be dispersed or exfoliated in water by using sonication for produced graphene oxide which contains flakes of monolayer. Thus, the number of layers is the main difference between graphite oxide and graphene oxide. The common methods to turn graphite oxide into graphene oxide by using sonication, stirring or combination of both methods. The sonication is spending a slight time for exfoliating graphite oxide. It is very successful at producing graphene by sonicated, but it can also damage the graphene flakes and reducing its surface size from micrometers to nanometers, and also produces many different of sheet sizes. While the mechanically stirring is not damaging the graphene flakes, but it takes a longer time to complete.

From graphene oxide to reduced graphene oxide (as show in Fig 2.9): There are many techniques to reduce graphene oxide such as chemical, thermal or electrochemical. All of these techniques can produce very high quality of rGO, like original graphene and high quantities of product. The properties of rGO are as follows in Table 2.1.

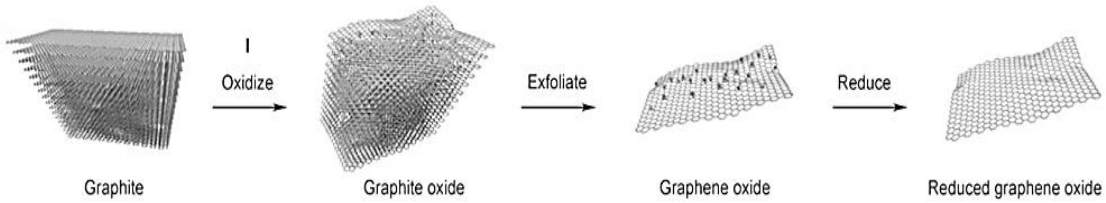

Fig 2.9 Schematic of the transformation of graphite to reduced graphene oxide

Table.2.1. Properties of rGO are as follows: [41, 42]

Reduction method	Chemically reduced
Color	Dark brown or black
Form	Powder
Odor	Odorless
Sheet dimension	Variable
Electrical conductivity	600-700 S/m
Humidity (Karl Fisher, TGA)	3.7 - 4.2 %
BET surface area	422.69 – 499.85 m^2/g

- **Graphitic carbon nitride (g-C_3N_4)** [43]

The graphitic carbon nitride or graphite-like carbon nitride (g-C_3N_4) is a metal-free polymer n-type semiconductor with heptazine ring structure (as show in fig 2.10) and the high condensation degree show many advantages such as unique electrical, optical, structural and good physiochemical properties, along with present the electronic structure combined with a medium band gap (2.7 eV), which encourages g-C_3N_4- based photocatalysts have an interest in the field of visible- light- active photocatalytic.

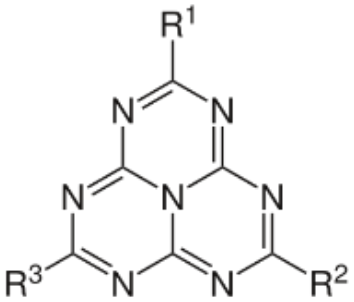

Fig 2.10 The heptazine ring structure of g-C_3N_4

2.6.2 Application of rGO and g-C_3N_4

Applications of rGO: [44]

- Graphene research
- Batteries
- Biomedical
- Super-capacitors
- Printable graphene electronics

Applications of g-C_3N_4-based materials: [45]

- Tribological coatings
- Biocompatible medical coatings
- Chemically inert coatings
- Insulators
- Energy-storage solutions
- Electronic
- Catalytic
- Energy applications

2.7 Literature review of BiOBr/GO, BiOBr/rGO and BiOBr/g-C_3N_4

Sandip P. Patil et al [46] (2016) studied on the preparation of BiOBr-graphene oxide nanocomposite via a facile sonochemical method. The photocatalytic performance of BiOBr/graphene oxide nanocomposite for the degradation of direct

green under UV– Visible light irradiation was investigated. It was found that the BiOBr/ graphene oxide nanocomposite shown significant enhancement in photocatalytic degradation of direct green under UV– Visible light irradiation as compared with pure BiOBr. The Improvement in photocatalytic performance of BiOBr-graphene oxide nanocomposite was due to the reduction in recombination of photo-generated electron and hole pairs and their transfer by graphene oxide sheets as well as combined effect of adsorption and photocatalysis of BiOBr- graphene oxide nanocomposite.

S. Vadivel et al [9] (2014) studied on the efficient photocatalyst for degradation of methylene blue and rhodamine-B dyes under visible light of graphene oxide/BiOBr composites photocatalyst material. Graphene oxide/ BiOBr composite material prepared via a facile method, by mixing BiOBr powder with Graphene oxide solution and sonicated to obtain a homogeneous solution. The photocatalytic performance on the degradation in aqueous solution of methylene blue (MB) and rhodamine-B (Rh- B) and the influence of the GO loadings on the photocatalytic activity was investigated. It was found that this hybrid material showed better and faster degradation than pure BiOBr so far and it can be assumed that the enhanced photocatalytic efficiency of graphene oxide/ BiOBr composite materials were due to the effective separation of electron and hole pairs by the graphene oxide sheets.

Wendong Zhang et al [10] (2014) studied on the enhancement the visible light photocatalytic performance of BiOBr/ graphene and BiOBr/ graphene oxide nanocomposites. The nanocomposites were prepared by a cost effective precipitation–deposition route method at room temperature. The obtained BiOBr/ graphene and BiOBr/ graphene oxide nanocomposites demonstrate significantly enhanced photocatalytic activity for the degradation of rhodamine-B (Rh- B) dye and removal of nitrogen oxide gas under visible light irradiation when compare with the pure BiOBr. Furthermore, BiOBr/graphene oxide materials show superior photodegradation activity than the BiOBr/graphene materials which can be generalized to the larger surface areas

and pore volumes, and effective separation and transfer of the photo-generated electron and hole pairs.

Zhihui Ai et al [6] (2011) studied on the efficient visible light photocatalytic removal of gaseous nitrogen monoxide (NO) with BiOBr-graphene nanocomposites which, prepared by solvothermal method with various molar ratios of Bi and graphene of 10:1, 20:1, 50:1 and 100:1. The photocatalytic efficiency for NO removal was evaluated by comparing pure BiOBr with BiOBr-graphene nanocomposites. It was found that BiOBr-graphene nanocomposites exhibit a superior performance on photocatalytic removal of gaseous NO to pure BiOBr under visible light irradiation (λ > 420 nm). The reasons for the enhanced photocatalytic activity of the BiOBr-graphene nanocomposites were charge transportation and the effective separation of the photo-generated electron and hole pairs.

S. Vadivel et al [37] (2014) studied on the efficient photocatalytic performance for methyl orange degradation of Sm-doped BiOBr/reduced graphene oxide (RGO) composite. The Sm-doped BiOBr/reduced graphene oxide composite was synthesis via solvothermal method using methanol as solvent. The degradation of methyl orange (MO) which is anionic dye, by the synthesized composites materials was evaluated under visible light irradiation. The results show that Sm-BiOBr/reduced graphene oxide composite show superior photocatalytic activity than pure BiOBr and BiOBr/ reduced graphene oxide composite.

Liqun Ye et al [47] (2013) studied on the enhancement the visible light photocatalytic activity of BiOBr/g-C_3N_4 composite which prepared via one-step chemical bath method at low temperature by dropped the mixture solution of $Bi(NO_3)_3 \cdot 5H_2O$ and CTAB in g-C_3N_4 suspension. Then the mixture was stirred and heated in water bath at 80 °C, the obtained BiOBr/g-C_3N_4 composite will contains 50% of BiOBr and 50% of g-C_3N_4. When comparing with pure BiOBr and g-C_3N_4, the BiOBr/g-C_3N_4 composite photocatalyst material showed enhanced photodegradation activity to rhodamine-B (Rh-B) dye under visible light irradiation. It was found that, the interaction between BiOBr and g-C_3N_4 is facets coupling can promote the photo-generated

electron and hole pairs transfer between BiOBr and g-C_3N_4 that resulting in an enhancement of the photocatalytic activity for rhodamine-B dye degradation.

Jiexiang Xia et al [48] (2014) studied on the enhancement the visible light photocatalytic activity of sphere-like g-C_3N_4/BiOBr composites via the EG- assisted the solvothermal process by used ionic liquid 1-hexadecyl-3-methylimidazolium bromide ([C_{16}mim] Br) as important solvent, reactant and template at the same time. The photocatalytic activities of g-C_3N_4/BiOBr composites were examined for the degradation of bisphenol A (BPA) and rhodamine-B (Rh- B) dye under visible light irradiation. The result showed that a loading amount of g- C_3N_4 over BiOBr in g- C_3N_4/ BiOBr photocatalysts materials lead to an increase of photocatalytic activity on the degradation of BPA and Rh- B under visible light irradiation when compared with pure BiOBr sample and g- C_3N_4. It can suppose that the enhanced photocatalytic performance were due to the effective separation of the photo-generated electron and hole pairs.

Yanjuan Sun et al [49] (2014) studied on the enhancement the visible light photocatalytic activity of BiOBr/ g- C_3N_4 two- dimensional nanojunctions by self-assembly of BiOBr nanosheets on g- C_3N_4 nanosheets by a chemical precipitation method at room temperature. The photocatalytic activity of the obtained BiOBr/g-C_3N_4 nanojunctions was evaluated by removal of nitrogen monoxide (NO) in gas phase under visible light irradiation. The result showed that the coupling of BiOBr with g-C_3N_4 lead to strong electronic interaction between the two components with well-matched band structures and the BiOBr/ g- C_3N_4 nanojunctions photocatalyst showed significant enhancement in photocatalytic activity for removal of NO gas under visible light irradiation, which can be supposed to the effective separation of the photo-generated electron and hole pairs.

CHAPTER III

EXPEIMENTAL PROCEDURE

3.1 Chemicals used in this research

1. Bismuth nitrate pentahydrate (Bi $(NO_3)_3 \cdot 5H_2O$), Sigma-Aldrich Pte. Ltd.

2. Potassium Bromide (KBr), Ajax Finechem Pty. Ltd.

3. Glycerol, Ajax Finechem Pty. Ltd.

4. Graphene oxide (GO), XF NANO, INC Advance Material Supplier, China.

5. Sodium borohydride ($NaBH_4$), Sigma-Aldrich Pte. Ltd.

6. NaOH, Ajax Finechem Pty. Ltd.

7. HCl 36%, Ajax Finechem Pty. Ltd.

8. Urea, Ajax Finechem Pty. Ltd.

9. Ethanol, RCI Labscan Ltd.

10. Distilled water

11. Rhodamine B (Rh-B), Loba chemie Pvt. Ltd.

3.2 Synthesis of BiOBr

BiOBr was synthesized via a precipitation method at room temperature. In a typical process, the first solution made by dissolving 0.8 mmol of (Bi $(NO_3)_3 \cdot 5H_2O$) in aqueous solution containing 10 ml of distilled water and 20 ml of glycerol and stirred until it became homogeneous. Next, the second solution made by dissolving 0.8 mmol of KBr in 30 ml of distilled water and stirred until it became transparent. After that, the first solution was added to the second solution, then stirred and aged for 2 hr.

Thereafter, the precipitates (BiOBr) were washed thoroughly for several times with distilled water and ethanol. Finally, precipitates were dried at 60 °C in vacuum oven. The synthesis diagram is shown in Fig 3.1.

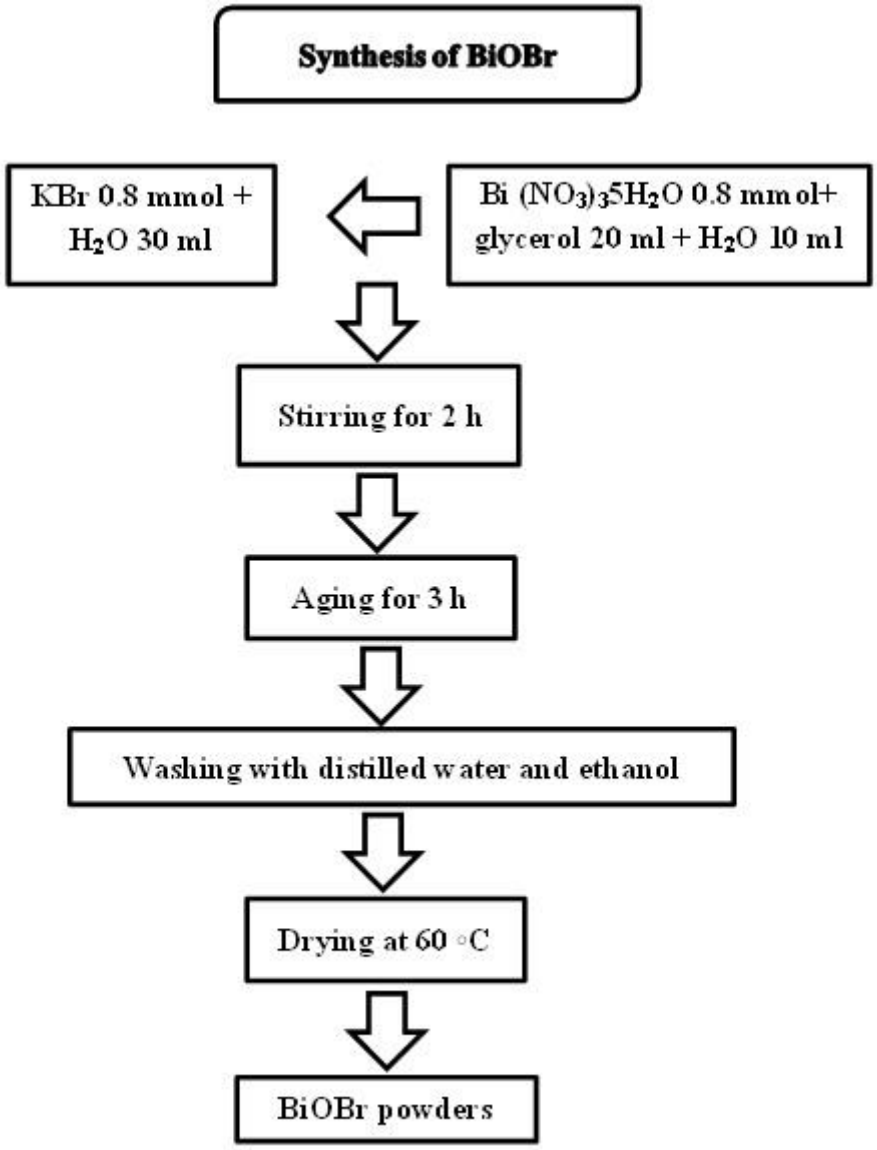

Fig 3.1 The synthesis diagram of pure BiOBr.

3.3 Synthesis of composites materials

3.3.1 Synthesis of BiOBr/GO composites

BiOBr/GO composites were synthesized via a precipitation method at room temperature. In a typical process, the first solution made by added 0.1, 0.25, 0.5, 1 and 2 wt% of graphene oxide (GO, XF NANO, INC Advance Material Supplier, China) in 10 ml of distilled water and sonicated until it became completely disperse. Then dissolving 0.8 mmol of ($Bi(NO_3)_3 \cdot 5H_2O$) in GO suspension with 20 ml of glycerol and stirred until it became homogeneous. Next, the second solution made by dissolving 0.8 mmol of KBr in 30 ml of distilled water and stirred until it became transparent. After that, the first solution was added to the second solution, then stirred and aged for 2 hr. Thereafter, the precipitates (BiOBr/GO composites) were washed thoroughly for several times with distilled water and ethanol. Finally, precipitates were dried at 60 °C in vacuum oven.

3.3.2 Synthesis of BiOBr/rGO composites

3.3.2.1 Synthesis of rGO [50]

2.5 M $NaBH_4$ solution was prepared by dissolving the required amount of $NaBH_4$ into a diluted NaOH solution, where the solution pH was adjusted to 11–12 in order to suppress the hydrolysis of borohydride. Then, 50 ml of the desired amount of GO solution was ultrasonically dispersed for 1 h in a beaker. After that, 12.5 ml of 2.5 M $NaBH_4$ aqueous solution was dropped into the mixed solution at 25 ℃ for 1 h. The solution pH was adjusted to 6 by adding 3 M HCl solution. After the reaction, the powder was washed by methanol for several times. The process for synthesis rGO was shown in Fig 3.2.

3.3.2.2 Synthesis of BiOBr/rGO composites

BiOBr/rGO composites were synthesized via a precipitation method at room temperature. In a typical process, the first solution made by added 0.1, 0.25, 0.5, 1 and 2 wt% of reduced graphene oxide (rGO) in 10 ml of distilled water and sonicated

until it became completely disperse. Then dissolving 0.8 mmol of (Bi $(NO_3)_3$•$5H_2O$) in rGO suspension with 20 ml of glycerol and stirred until it became homogeneous. Next, the second solution made by dissolving 0.8 mmol of KBr in 30 ml of distilled water and stirred until it became transparent. After that, the first solution was added to the second solution, then stirred and aged for 2 hr. Thereafter, the precipitates (BiOBr/rGO composites) were washed thoroughly for several times with distilled water and ethanol. Finally, precipitates were dried at 60 °C in vacuum oven.

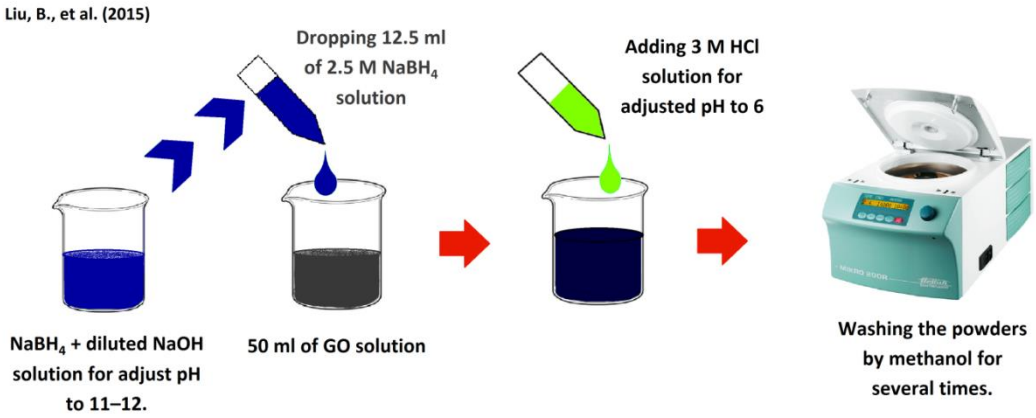

Fig. 3.2 Schematic diagram to show the synthesis process of the rGO.

3.3.3 Synthesis of BiOBr/g-C_3N_4

3.3.3.1 Synthesis of g-C_3N_4[51]

Urea was put in a crucible with a cover and heated in a muffle furnace under static air at 550 °C for 4 h with a heating rate of 1.5°C·min^{-1}. The synthesis procedure was shown in Fig. 3.3.

3.3.3.2 Synthesis of BiOBr/g-C_3N_4

BiOBr/g-C_3N_4 composites were synthesized via a precipitation method at room temperature. In a typical process, the first solution made by added 0.1, 0.25, 0.5, 1 and 2 wt% of graphitic carbon nitride (g-C_3N_4) in 10 ml of distilled water and sonicated until it became completely dispersed. Then dissolving 0.8 mmol of (Bi $(NO_3)_3$•$5H_2O$) in

g-C_3N_4 suspension with 20 ml of glycerol and stirred until it became homogeneous. Next, the second solution made by dissolving 0.8 mmol of KBr in 30 ml of distilled water and stirred until it became transparent. After that, the first solution was added to the second solution, then stirred and aged for 2 hr. Thereafter, the precipitates (BiOBr/g-C_3N_4 composites) were washed thoroughly for several times with distilled water and ethanol. Finally, precipitates were dried at 60 °C in vacuum oven.

Fig. 3.3 Schematic diagram to show the synthesis process of the g-C_3N_4.

The synthesis diagram of BiOBr composite with GO, rGO and g-C_3N_4 is shown in Fig 3.4.

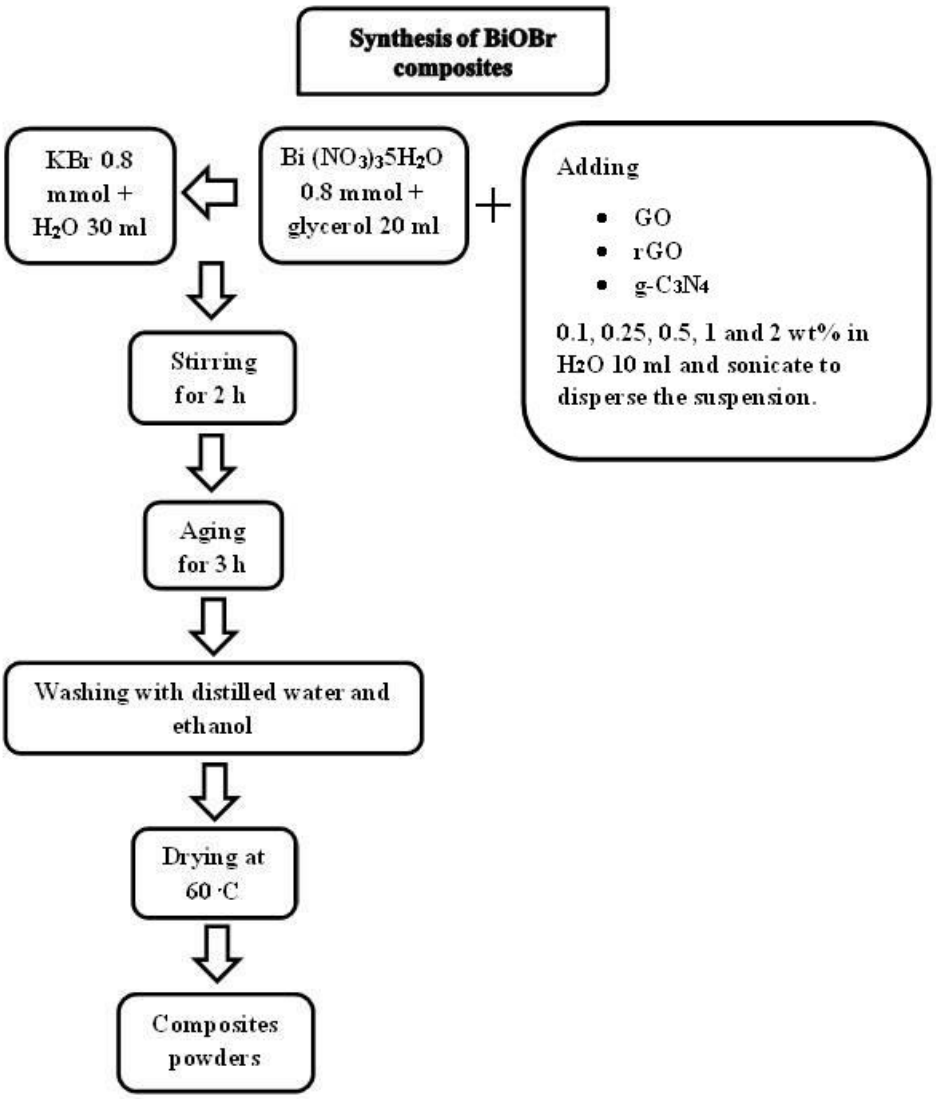

Fig 3.4 The synthesis diagram for BiOBr-based composites.

3.4 Catalyst characterization

3.4.1. X-ray diffraction (XRD, Bruker D2 PHASER)

Crystalline phase structure of as-synthesized samples were characterized by X-ray diffraction (XRD) using Cu-K_α radiation with 30 kV, 10 mA. Scanning rate is 2.4 degree/min from 2θ at 5 to 80 degree. The obtained peaks were matched JCPDS (Joint Committee on Powder Diffraction standard files):

Debye Scherrer equation: $$D_c = \frac{K\lambda}{\beta cos\theta}$$ (Equation 3.1)

When D_c is average crystalline size (nm)

K is Debye Scherrer constant (usually taken as 0.89)

λ is wavelength of x-ray radiation (Cu-K_α = 0.154 nm)

β is line width at half-maximum height of the broadened peak (full width at half maximum (FWHM))

θ is the half diffraction angle of the centroid of the peak (degree)

3.4.2. Field emission Scanning Electron Microscopy and Energy-dispersive X-ray spectroscopy analysis (FE-SEM-EDS, JEOL JSM-7610F)

The surface morphology of as-synthesized samples were obtained by FE-SEM and the elemental analysis of as-synthesized samples were detected by EDS. The obtained samples were prepared as follows

1) Cut a small piece of glass slide to size 5x5 mm.

2) Cleaned the pieces of glass slide by ultrasonication with distilled water and ethanol for 10-15 minutes and dried it.

3) Dispersed the as-synthesized powder 0.01 g in 10 ml of ethanol by ultrasonication for 15 minutes.

4) The suspensions was dropped on prepared glass slide and dried in desiccator at room temperature.

5) The obtained glass slide was mounted on the cradle by a carbon tape and coated the surface of obtained glass slide by gold.

6) FE-SEM was performed at 5-15 kV with magnification of 10,000-50,000.

3.4.3. Transmission Electron Microscope analysis (TEM, JEM-2100)

The morphology of as-synthesized samples were obtained by TEM. The as-synthesize samples were prepared by similar procedure was described in section 3.4.2, but the suspensions was dropped on copper grids and prepared grids were dried in desiccator at room temperature at least 24 hr.

3.4.4. Fourier transforms infrared spectroscopy analysis (FT-IR, NICOLET 6700)

The infrared spectra of absorption of as-synthesized samples were measured by using the FT-IR spectrometer. The samples for FT-IR analysis were prepared in the form of a pellet, by mixing the dry form of as-synthesized samples with KBr (99%, FT-IR grade).

3.4.5. The Brunauer-Emmett-Teller (BET: Quantachrome NOVA-4200E system)

The Brunauer-Emmett-Teller (BET) specific surface area was determined by the nitrogen adsorption-desorption isotherm on the Quantachrome NOVA-4200E system. The 0.2 grams of as-synthesized powder sample was put into glass tube and dried in vacuum at 220 °C for 60 minutes. After that, the glass tube contained the sample was placed in liquid nitrogen to measure the adsorption ability for liquid nitrogen on surface.

3.4.6. UV-Vis diffuse reflectance analysis (UV-670)

UV- Vis diffuse reflectance (DRS) spectra were recorded on a UV- Vis Spectrophotometer (UV- 670) with $BaSO_4$ as an internal standard between the wavelength ranges of 200 - 900 nm. The as- synthesized samples were prepared by pressing in sample holder as shown in Fig 3.5.

Fig. 3.5 As-synthesized powder in sample holder for UV-Vis diffuse reflectance analysis.

From the diffuse reflectance spectrum and the absorbance measurement can calculated from Kubelka-Munk (KM) equation [52]:

$$\boldsymbol{F(R) = \frac{(1-R)^2}{2R}} \qquad \text{(Equation 3.2)}$$

When **F(R)** is Kubelka-Munk (KM) function (In this case is A, Absorbance)

R is reflectance

Thus, in this case, the relational function become

$$\boldsymbol{A = \frac{(1-R)^2}{2R}} \qquad \text{(Equation 3.3)}$$

Tauc, Davis and Mott gave an equation derived for the absorption constant relationship with excitation energy ($\mathbf{E_{exc}} = \mathbf{h\nu}$) as [53]:

$$\boldsymbol{\alpha h\nu = k(h\nu - E_g)^n} \qquad \text{(Equation 3.4)}$$

When **α** is Absorption constant

h is Planck's constant = 6.626×10^{-34} J·s, 4.135×10^{-15} eV.s

ν is frequency of vibration

k is constant which does not depend on photo energy

E_g is optical band gap

n is 2 for the indirect transition

The **α** in Tauc equation can be substituted with A, which is the absorption coefficient from equation 3.3. Thus, the equation can be derived as fallow:

When $\alpha \sim A$: Thus $$Ah\nu = k(h\nu - E_g)^n$$

$$(Ah\nu)^{1/n} = k(h\nu - E_g) \quad \text{(Equation 3.5)}$$

3.5 Photocatalytic activity evaluations

3.5.1. Rhodamine B (Rh-B) degradation

The photocatalytic activities of as-prepared samples were determined by the decomposition of Rhodamine B (Rh-B) aqueous solution under the visible light irradiation was shown in Fig 3.6. A solar simulator (ASAHI spectra HAL-302, 300W Xenon arc lamp) was used as a light source, and the light intensity was set at 360 W/m^2. The cutoff filter was placed on the beaker containing the solution to completely remove any radiation below the wavelength of 420 nm to provide visible light irradiation, and the Xenon lamp was mounted on top of beaker and filter. In the Rh-B decomposition process 0.1 g of photocatalyst was added into a 200 mL of 15 mg/L Rh-B solution. Before irradiation, the solution was stirred for 5 h in darkness to reach the adsorption-desorption equilibrium of Rh-B. Every 10 min of irradiation time intervals, about 5 mL suspensions were collected, and then centrifuged to remove the photocatalyst

particles. The concentrations of Rh-B were examined in the way of checking the absorbance of solution during the photodegradation process.

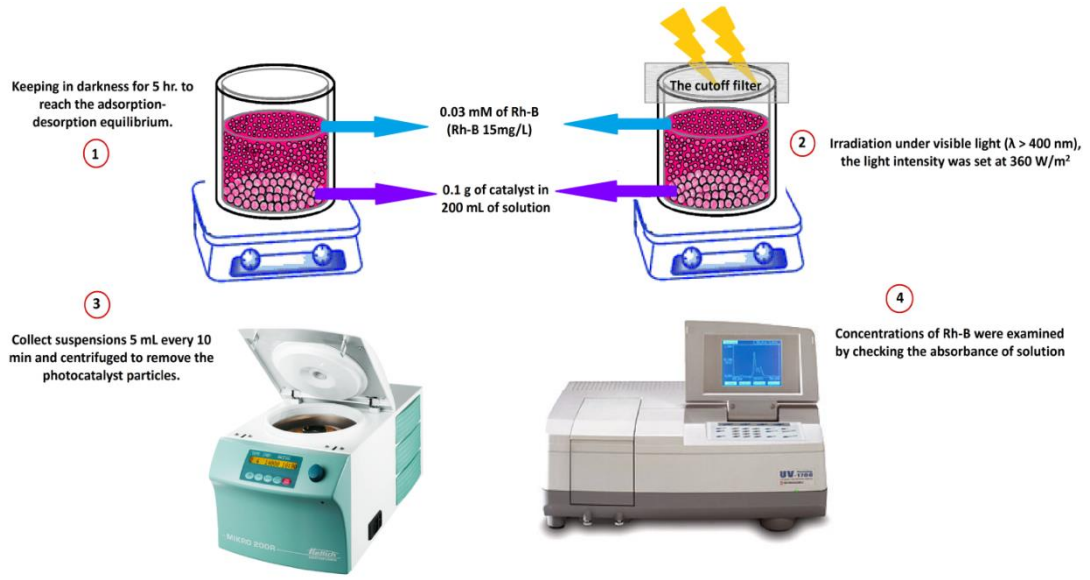

Fig.3.6 The measurement photocatalytic activity process for dye degradation.

3.5.2. Removal of nitrogen oxide gas (NO_x)

The photocatalytic activity of as-prepared samples were determined by evaluating the decomposition of NO ($deNO_x$) using a flow type reactor under visible light irradiation of a solar simulator (ASAHI spectra HAL-302, 300W Xenon arc lamp) at room temperature. The photocatalyst was spread in the hollow (20 mm x 16 mm x 0.5 mm) of a glass plate and then was placed at the bottom center of the reactor (373 cm^3 of internal volume) in which 1:1 mixed gas of air and nitrogen containing 1ppm of NO was flowed at the rate of 200 cm^3 min^{-1}. The sample was kept in the dark for 10 min to reach the adsorption-desorption equilibrium of NO gas. After that, the solar simulator was turned on to irradiate the sample, where the light wavelength was controlled by filter (Kenko L41 Super Pro (W) filter> 400 nm). The measuring time for each sample was 10 min. The concentration of NO_x was checked by a NO_x analyzer (Yanaco, ECL-88A). The process for estimation of the photocatalytic activity of materials through oxidation of NO_x was shown in Fig 3.7.

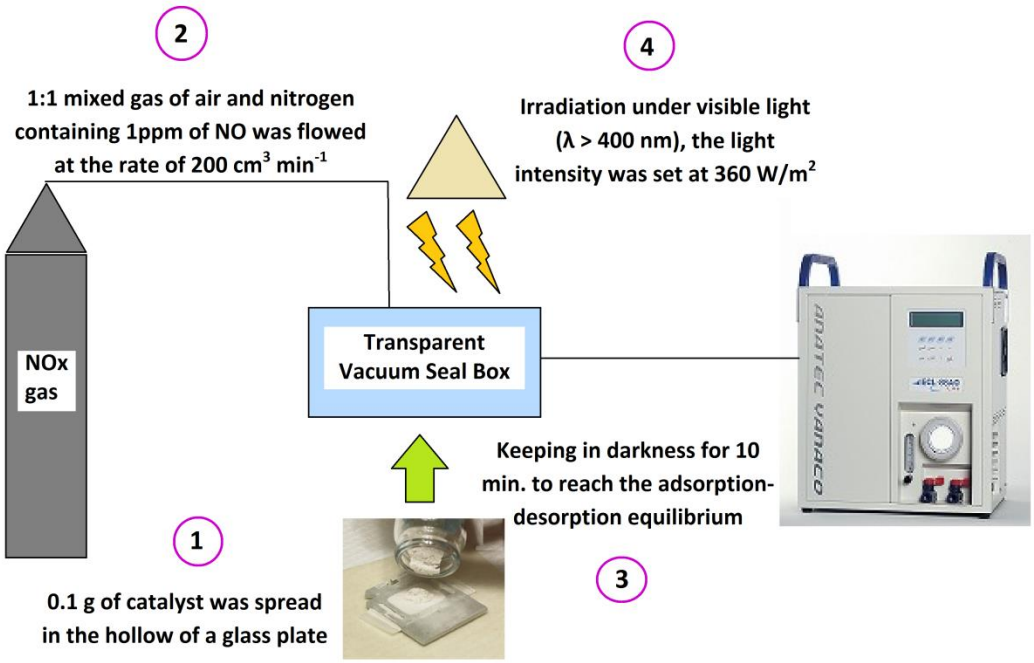

Fig.3.7 The process for estimation of the photocatalytic activity of materials through oxidation of NO_x

CHAPTER IV

RESULTS AND DISCUSSION

In this research, the preparation of pure BiOBr, BiOBr/GO composites, BiOBr/rGO composites, BiOBr/g-C_3N_4 composites were studied. The effect of amount of graphene oxide (GO), reduced graphene oxide (rGO) and graphite like carbon nitride (g-C_3N_4) in the composite that affects to photocatalytic efficiency was investigated. Furthermore, the characteristic of obtained materials such as morphology, phase composition, specific surface area, energy bands and optical properties of composite were examined. Eventually, the photocatalytic activity of as-synthesized photocatalysts for degradation of rhodamine-B (Rh-B) dye and removal of nitrogen oxide (NO_x) gas under visible light was evaluated.

4.1 Synthesized BiOBr

4.1.1 X-ray diffraction study

The XRD pattern of the as-synthesized BiOBr was shown in Fig. 4.1. All the detectable diffraction peaks of the as-synthesized sample at 11.871, 23.691, 26.021, 32.671, 32.741, 40.831, 46.851, 48.771, 54.081, 58.681 and 68.171 degree can be assigned to the tetragonal phase of BiOBr (JCPDS file Card No. 73-2061). No other crystalline phases are observed indicating a high purity of the as-synthesized sample.

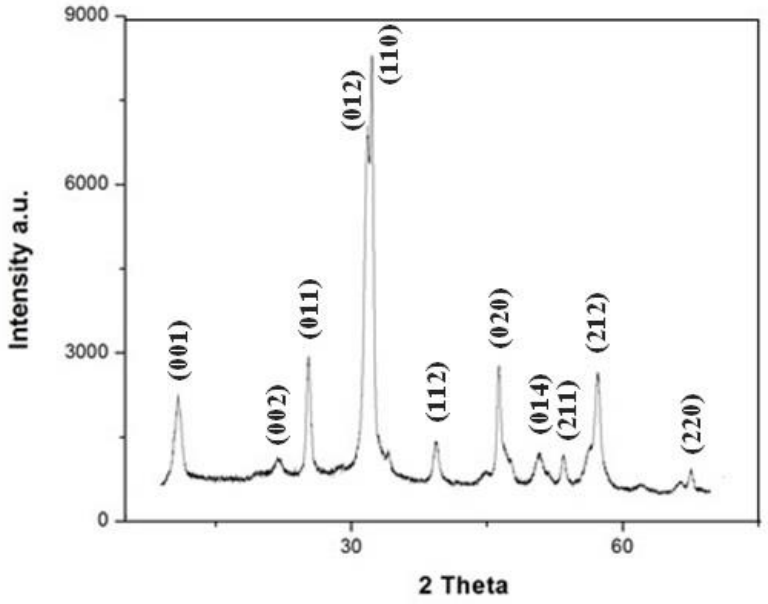

Fig.4.1 XRD pattern of the as-synthesized BiOBr.

4.1.2 FE-SEM and TEM analysis

The FE-SEM image of as-synthesized BiOBr as shown in Fig. 4.2 (a). Apparently each microstructured particle is composed of numerous fine plates. Further characterized by TEM as show in Fig. 4.2 (b). It can be seen that there are many plate in the microstructure of as-synthesized BiOBr, which was corresponding to FE-SEM result.

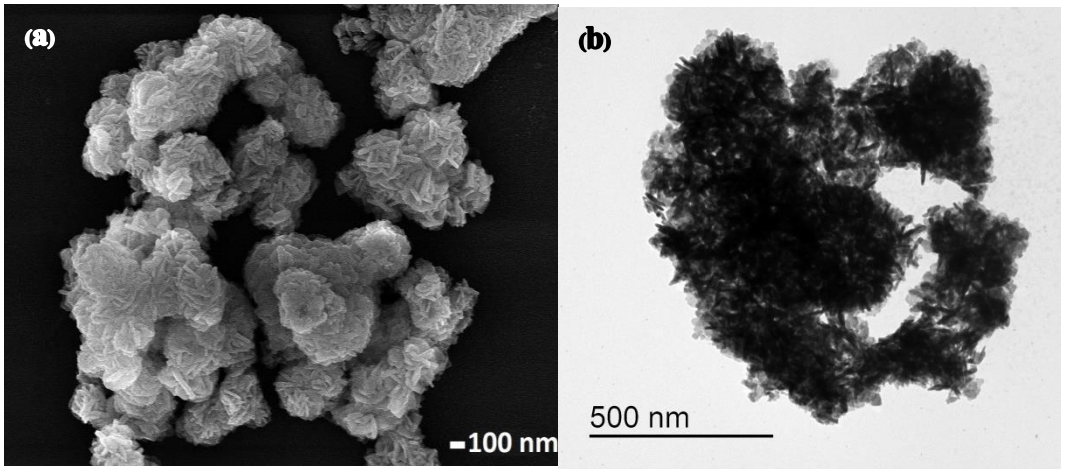

Fig.4.2 (a).FE-SEM and (b).TEM image of as-synthesized BiOBr.

4.1.3 FT-IR analysis

The FTIR spectrum of pure BiOBr was described in Fig. 4.3. The spectrum of pure BiOBr shows very sharp peak at 512 cm^{-1}. This is primarily due to the Bi-O stretching vibration mode in BiOBr.

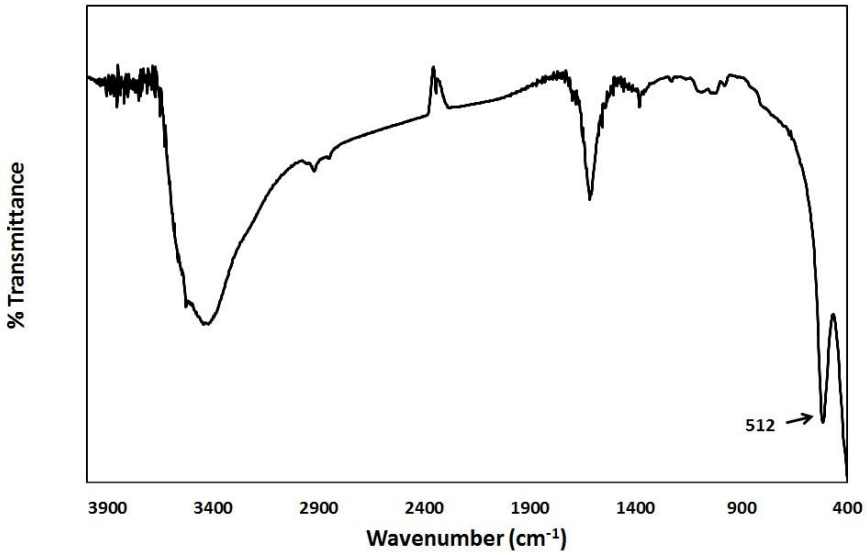

Fig.4.3 The FT-IR spectrum of pure BiOBr.

4.1.4 Specific surface area

The specific surface area is an important factor to determine the adsorptive capability of the photocatalysts toward organic contaminant such as dyes. From the results of the nitrogen adsorption-desorption tests, the specific surface area of as-synthesized BiOBr was calculated to be 20.663 m^2/g. It is widely accepted that the larger specific surface areas could provide more reactive center sites and absorb more reactants, resulting in an improved photocatalytic activity.

4.1.5 Optical properties

Absorption spectra measurement

The UV-Vis diffuse reflectance spectrum result of the as-synthesized BiOBr prepared by the precipitation method as shown in Fig. 4.4. Sample showed the strong absorption edge in the visible-light region with wavelength at about 430 nm corresponding to its band gap energy (2.9 eV).

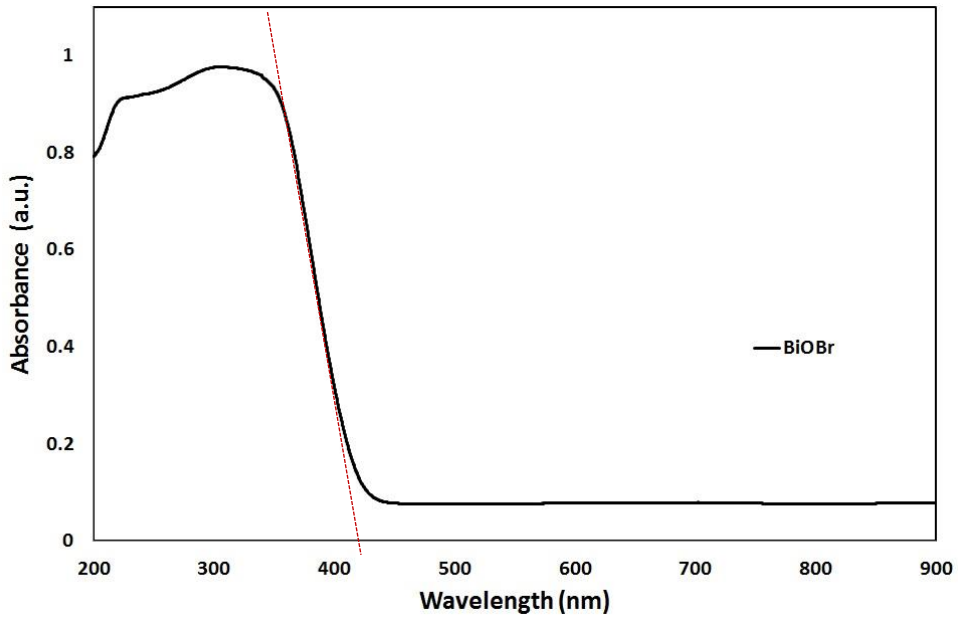

Fig.4.4 UV–Vis diffuse reflectance spectrum of the as-synthesized BiOBr.

Band gap energy

The optical band gap energy value of as-synthesized BiOBr estimated by linear extrapolation from the inflection point of the $(h\nu A)^{1/2}$ versus $h\nu$ graph to the x-axis was shown in Fig. 4.5. It was indicated that the as-synthesized BiOBr has small band gap energy about 2.9 eV and it can be expected that this sample could be activated under visible light due to its narrow band gab energy.

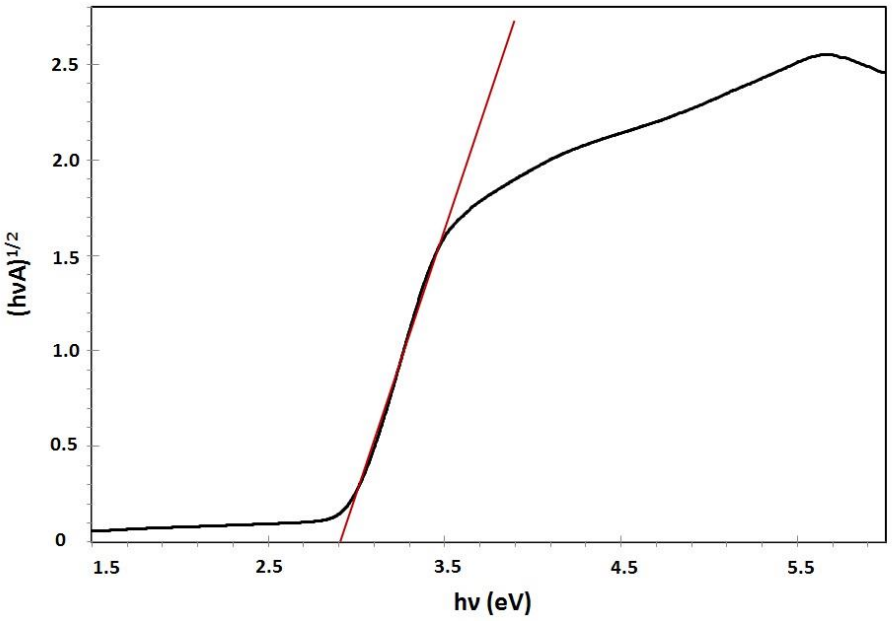

Fig.4.5 Band gap energy of the as-synthesized BiOBr.

4.1.6 Photocatalytic activity evaluation

4.1.6.1 Rhodamine B (Rh-B) degradation

The result in Fig. 4.6 demonstrate that the adsorption–desorption equilibrium of the Rh-B dye on the surface of BiOBr was attained at 45 min in the dark. The residual concentration of Rh-B decreased gradually during the beginning of the adsorption process and remained constant after reaching adsorption–desorption equilibrium.

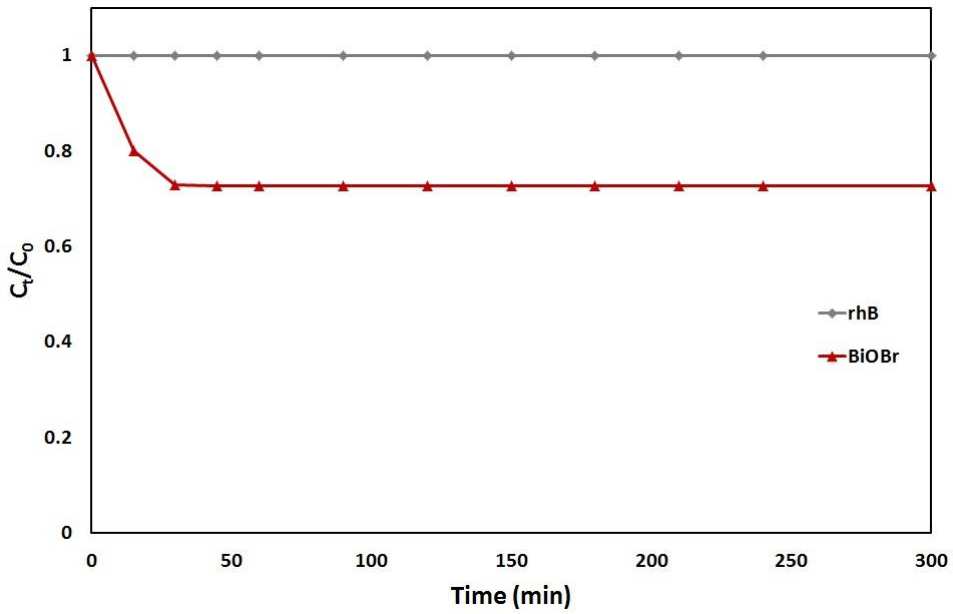

Fig.4.6 The change in concentration of Rh-B solution under darkness with time in the presence of BiOBr.

It is shown in Fig. 4.7 that the concentration of Rh-B remains unchanged during experiment under irradiation, indicating that there is no photolysis effect on Rh-B. On the other hand, the abrupt decrease in concentration of Rh-B in the presence of BiOBr after visible-light irradiation was observed. The highest decomposition efficiency of Rh-B in presence of BiOBr under visible light irradiation as shown in Fig. 4.7 was found to be 86.87% within 60 min (where C_0 and C_t is initial and residual concentration of Rh-B, respectively), and almost no degradation was obtained after that. The calculated photodegradation efficiency (%) for degradation of Rh-B solution of BiOBr is shown in Table 4.1.

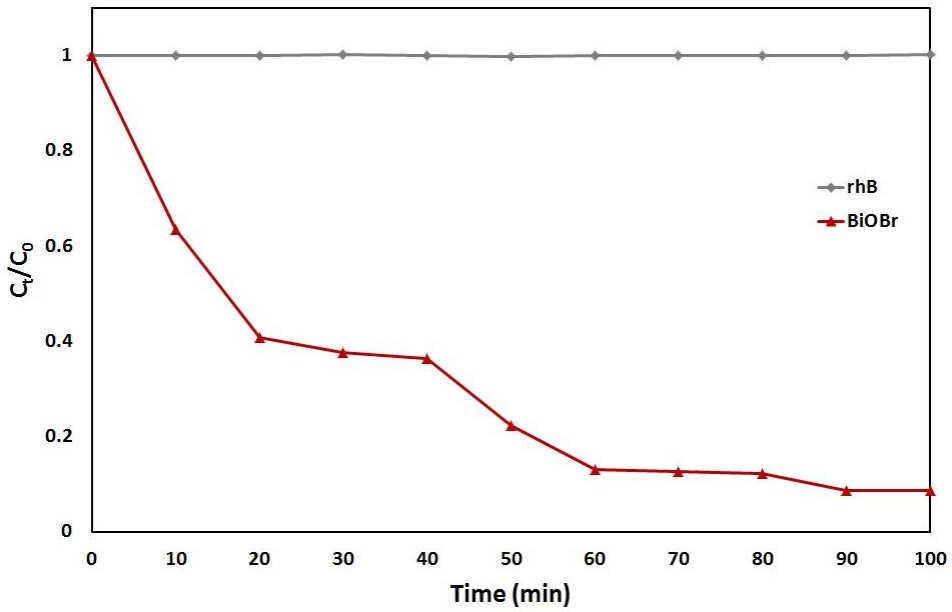

Fig.4.7 The photocatalytic activities for degradation of Rh-B under visible-light irradiation of as-synthesized BiOBr.

Table 4.1 Photodegradation efficiency (%) for degradation of Rh-B solution of BiOBr

Time (min)	Photodegradation efficiency (%)
10	36.50
20	59.16
30	62.49
40	63.68
50	77.77
60	86.87

4.1.6.2 Decomposition of nitrogen oxide gas (NO_x)

The nitrogen oxide gas (NO_x) decomposition test result of the prepared sample is presented in Fig. 4.8. Under visible light, the BiOBr sample showed photodegradation efficiency with 36.84 % of NO_x in 10 min. This result showed that the BiOBr has a potential to perform as photocatalyst for air purification under visible light irradiation.

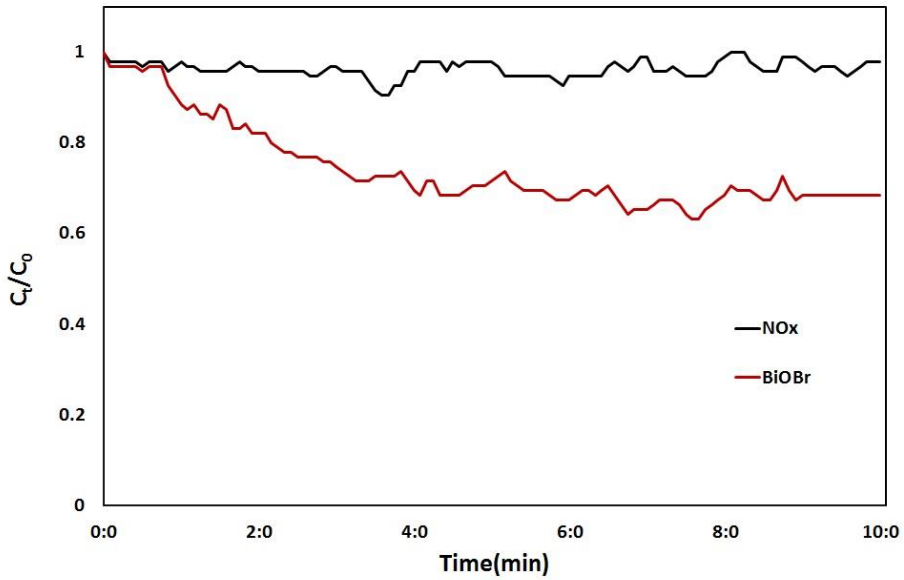

Fig.4.8 Photocatalytic degradation of the nitrogen oxide gas by the as-synthesized BiOBr under visible light irradiation.

4.2 BiOBr/GO Composites

4.2.1 X-ray diffraction study

The XRD patterns of the as-synthesized pure BiOBr and BiOBr/GO composites with 0.1, 0.25, 0.5, 1 and 2 % of GO, respectively are shown in Fig. 4.9. All the detectable diffraction peaks of the BiOBr sample comprising peaks at the 2θ values of 11.871, 23.691, 26.021, 32.671, 32.741, 40.831, 46.851, 48.771, 54.081, 58.681, and 68.171 degree could be assigned to the tetragonal phase of BiOBr (JCPDS file Card No. 73-2061). No characteristic peaks of other impurities were observed, which was indicating a high purity of the sample. For BiOBr/GO samples, it can be found that the XRD patterns are the same as the BiOBr sample. Furthermore, no typical diffraction peaks of GO could be observed in the nanocomposites on the XRD patterns, probably due to the small content of GO in composites.

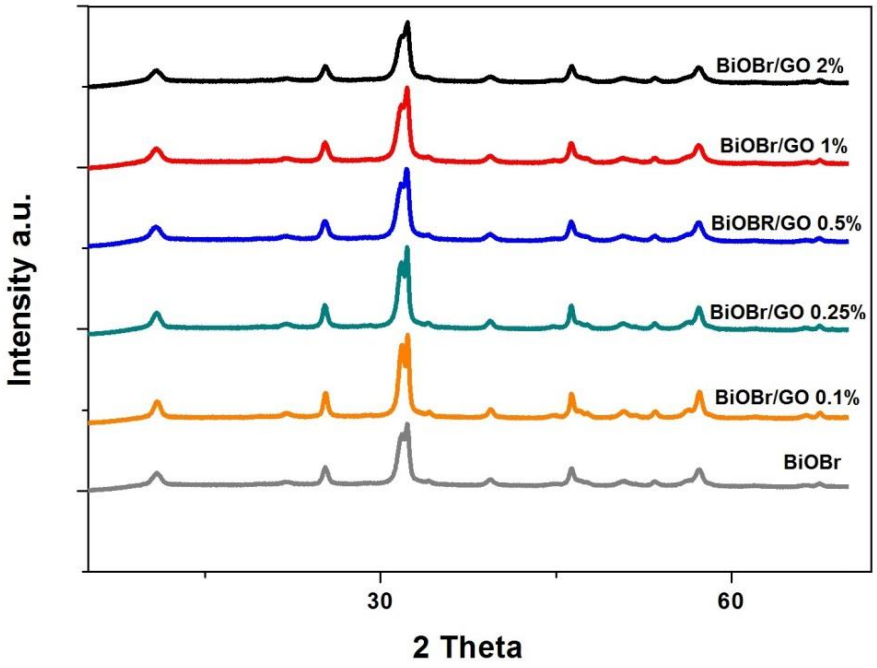

Fig.4.9 XRD diffraction patterns of pure BiOBr and BiOBr/GO composites with various amount of GO.

4.2.2 FE-SEM and TEM analysis

The FE-SEM images in Fig. 4.10 (a-c) show the surface morphologies of pure graphene oxide (GO), pure BiOBr and BiOBr/GO composites (2 % GO), respectively. As shown in Fig. 4.10 (a), GO sheet has thin wavy and wrinkled morphology. Fig. 4.10 (b) shows the FE-SEM image of BiOBr, and it was found that each microstructure of particle is composed of numerous fine plates. In Fig. 4.10 (c), the FE-SEM images of BiOBr/GO composites show that the BiOBr particles are dispersed on the wrinkled surface of GO sheets. This is evident that surface of GO sheets interacts with surface of BiOBr particles perfectly, which should effectively promote the charge transportation and separations for enhancing the photocatalytic activity.[11]

The TEM image of pure GO was shown in Fig. 4.10 (d), it demonstrates crinkle and transparent sheet. In Fig. 4.10 (e), it can be seen that there are many plates combined together in microstructure of the as-synthesized BiOBr. Fig. 4.10 (f) shows that the BiOBr plates are randomly dispersed on crinkled GO sheets, which was corresponding to FE-SEM result.

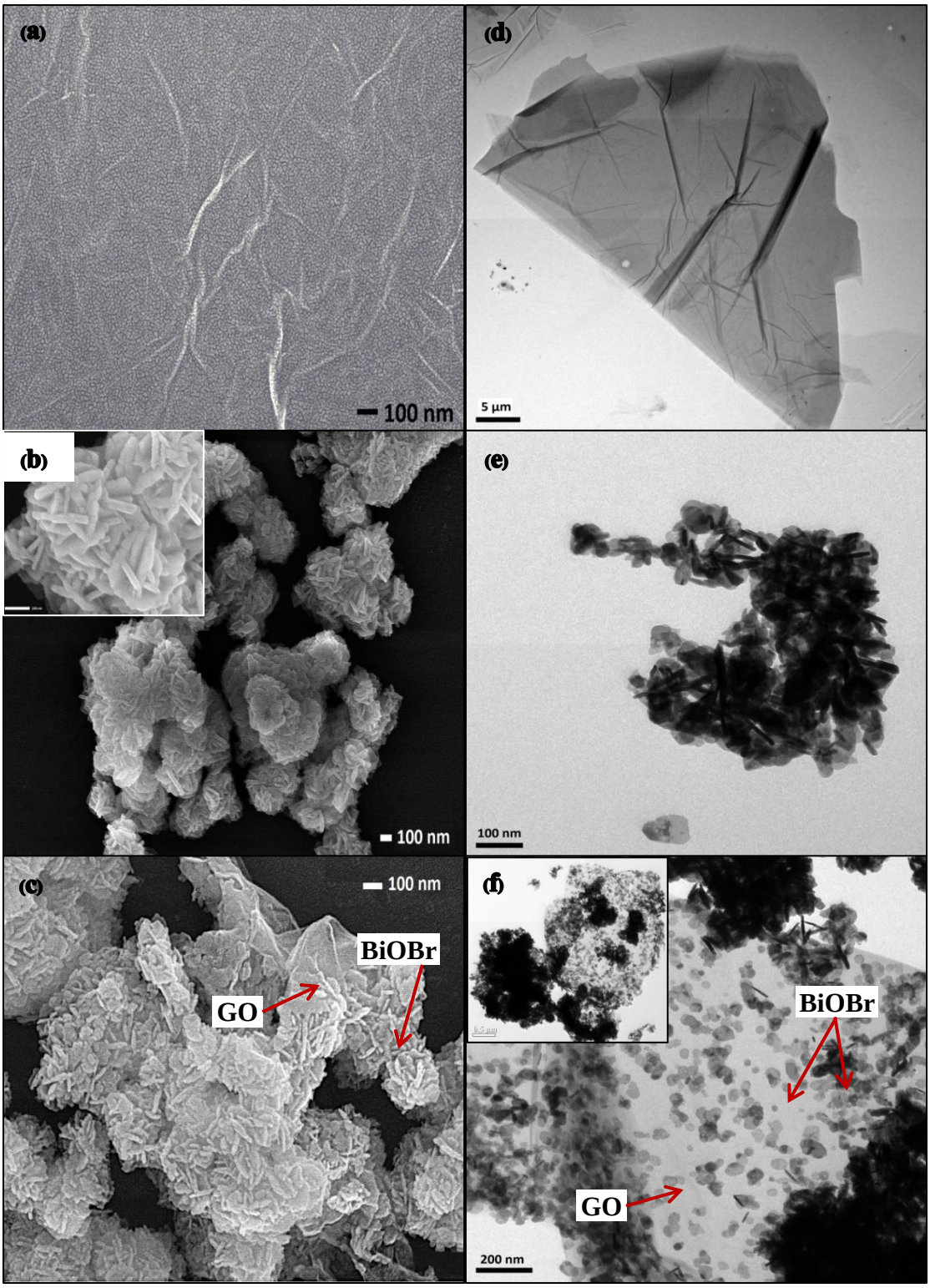

Fig.4.10 FE-SEM images of (a) pure graphene oxide (GO), (b) pure BiOBr, (c) BiOBr/GO composites (2 % GO) and TEM images of (d) pure graphene oxide (GO), (e) pure BiOBr, (f) BiOBr/GO composites (2 % GO).

4.2.3 FT-IR analysis [9]

The FTIR spectra of pure GO, BiOBr/GO composites and pure BiOBr were described in Fig. 4.11. The spectrum of GO shows broad peak around 3414 cm^{-1} related to O-H stretching vibration, a peak at 1719 cm^{-1} is due to the carbonyl stretching vibration, the peaks at 1383 cm^{-1} and 1218 cm^{-1} related to C-O-H and C-O-C stretching vibrations respectively. The peak around 1052 cm^{-1} is due to the C-O stretching vibrations and peak at 1618 cm^{-1} is attributed to vibration of the adsorbed water molecules and due to the vibrations of graphite. The spectrum of pure BiOBr shows peak at 512 cm^{-1} which is primarily due to the Bi-O stretching vibration mode in BiOBr.The FT-IR spectra of BiOBr/GO composites reveals the existence of GO along with BiOBr in the composite due to the appearance of the peak at 512 cm^{-1} corresponding to Bi-O vibrations and the peak corresponding to GO stretching vibrations appears at the synthesized composites.

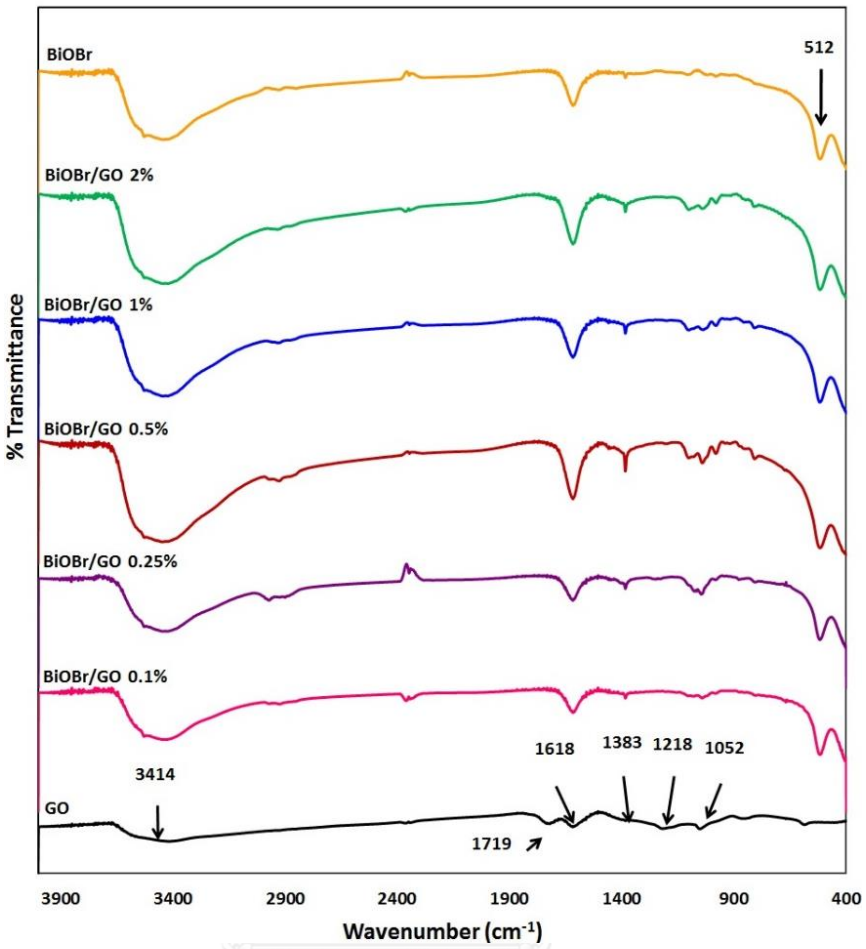

Fig.4.11 FTIR spectra of pure graphene oxide (GO), BiOBr/GO composites and pure BiOBr.

4.2.4 Specific surface area

From the results of the nitrogen adsorption-desorption tests, the specific surface area of pure BiOBr and BiOBr/GO composites with amount of GO 0.1, 0.25, 0.5, 1 and 2 wt% were shown in Table 4.2. It was shown that the specific surface area of composites was higher than that of pure BiOBr, in that the increasing in surface area from 20 to 35 m^2/g as the increasing amount of GO from 0 to 2.0 wt% was obtained.

Table 4.2 Specific surface area and band gap energy value (Eg) of pure BiOBr and BiOBr/GO composites.

Amount of GO (wt %)	0 %	0.1%	0.25%	0.5%	1.0%	2.0%
Specific surface area (m^2/g)	20.66	23.40	26.70	30.85	35	35.55
Band energy (eV)	2.9	2.9	2.9	2.86	2.94	2.94

4.2.5 Optical properties

Absorption spectra measurement

The UV-Vis diffuse reflectance spectrum results of the as-synthesized BiOBr and BiOBr/GO composites prepared by the precipitation method are shown in Fig. 4.12. All samples show the strong absorption edge in the visible-light region with wavelength about 420-450 nm.

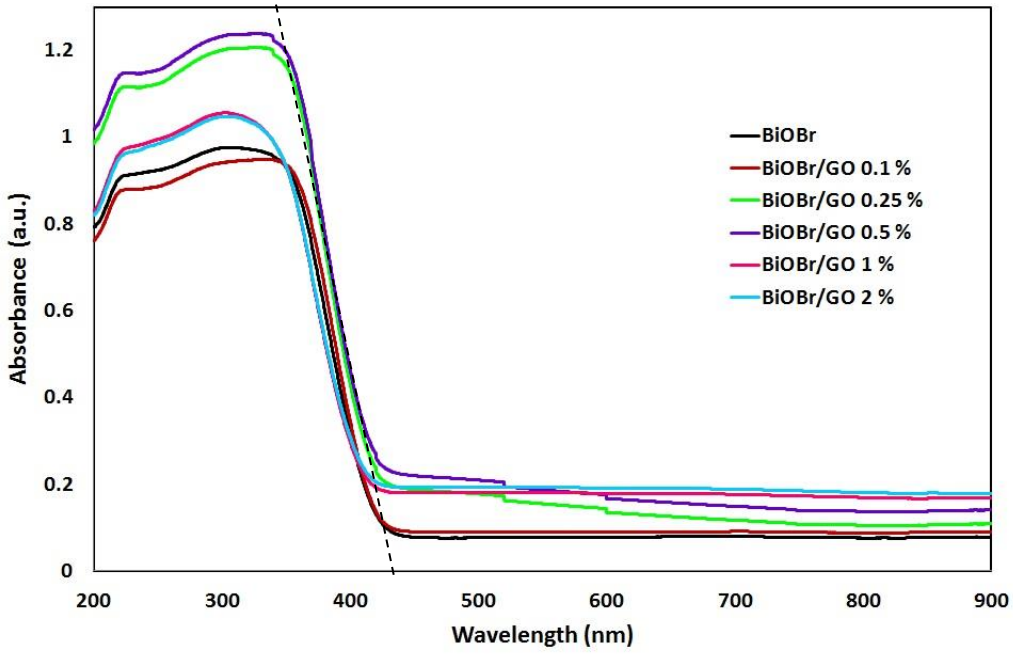

Fig.4.12 Display the UV-Vis diffuse reflectance spectra of pure BiOBr and BiOBr/GO composites.

Band gap energy

The optical band gap energy value of as-synthesized BiOBr and BiOBr/GO composites estimated by linear extrapolation from the inflection point of the $(h\nu A)^{1/2}$ versus $h\nu$ graph to the x-axis was shown in Fig. 4.13. It was demonstrated that pure BiOBr and BiOBr/GO composites have narrow band gap energy about 2.86-2.94 eV, indicating that BiOBr/GO composites are responsive visible light region.

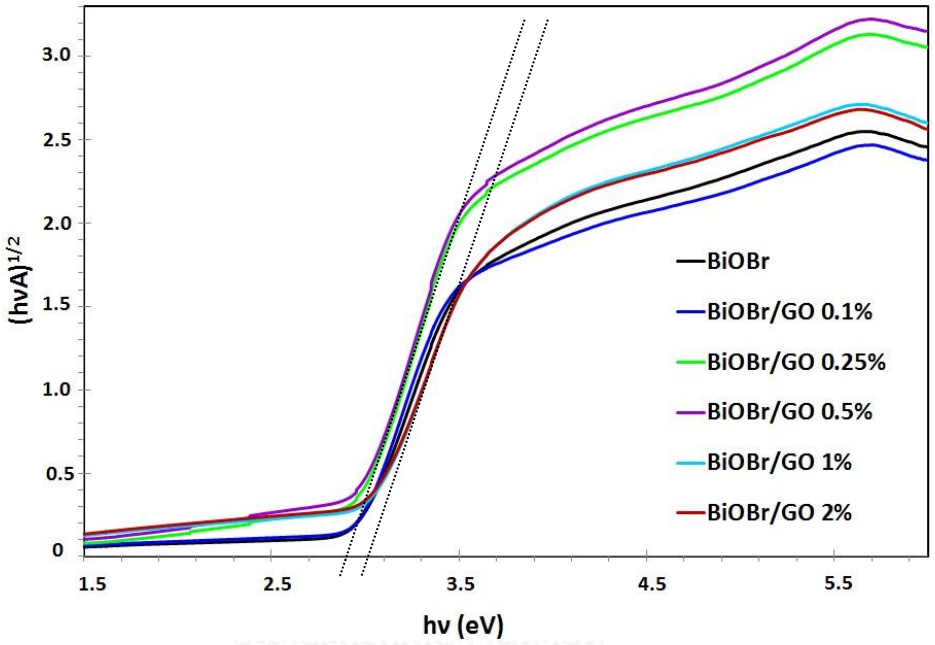

Fig.4.13 Band gap energy of pure BiOBr and BiOBr/GO composites.

4.2.6 Photocatalytic activity evaluation

4.2.6.1 Rhodamine B (Rh-B) degradation

In order to obtain the adsorption-desorption equilibrium of the Rh-B dye on the surface of BiOBr and BiOBr/GO composites, the experiment was done by suspending samples in Rh-B solution and kept in darkness until there was no change in concentration of Rh-B solution. The results of all samples are shown in Fig. 4.14. It demonstrated that the adsorption-desorption equilibrium of the Rh-B dye on the surface of BiOBr and BiOBr/GO composites with different amount of GO were attained at different time, indicating the effect of adsorption performance. However, the

concentration of Rh-B solution in the presence of all samples remains unchanged after keeping in dark for 300 min, confirming they were in equilibrium. It can be observed the increasing in adsorption ability with increasing amount of GO in composites in that the time requirement to attain the adsorption-desorption equilibrium was increased as increasing amount of GO. The enhanced adsorption ability might be caused by the increasing in surface area of composite when coupling with GO as shown in 4.2.4, since the surface area of photocatalyst plays an important role on the adsorption.

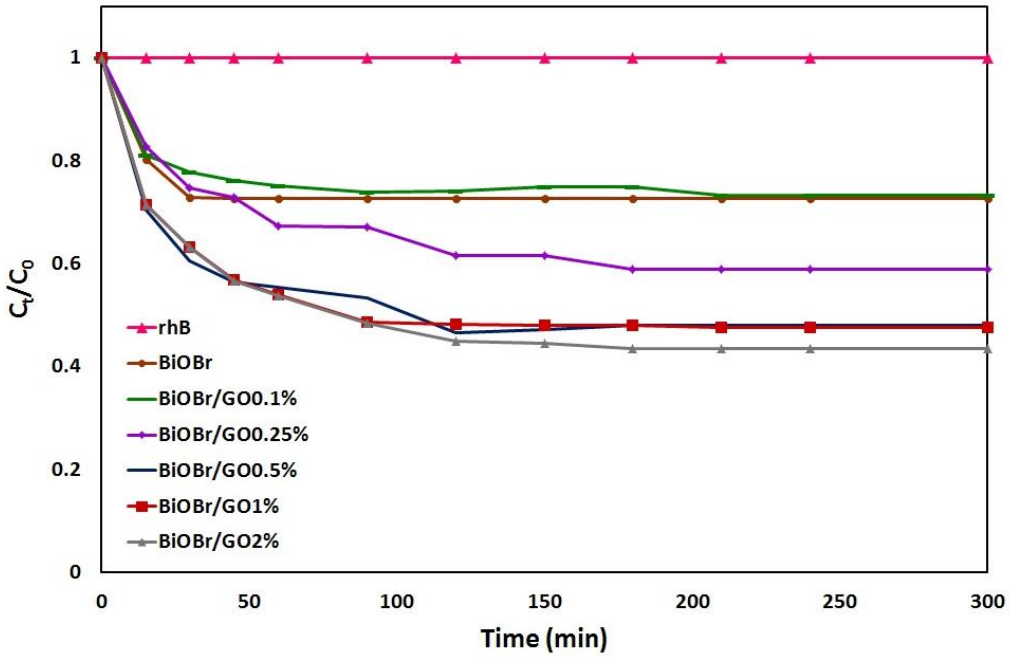

Fig.4.14 The change in concentration of Rh-B solution with time in the presence of BiOBr and BiOBr/GO composites in dark.

The photocatalytic activities of the as-synthesized samples were evaluated by measuring the degradation of Rhodamine B (Rh-B) in the aqueous solution under visible light irradiation. The changes in the concentration of Rh-B were checked by examining the variations in maximal absorption in UV-Vis spectra at 556 nm. It can be seen in Fig. 4.15 and Table 4.3 that the composite samples consisted of GO 0.25-1wt% exhibited higher Rh-B degradation efficiency than that of pure BiOBr, where the highest efficiency reached at 100% in 60 min was obtained with BiOBr/GO 1 % composite. This indicated that the optimum amount of GO (1%) played a crucial factor on the

photocatalytic activity enhancement. The improved photolytic efficiency could be attributed to the increasing dye adsorption and charge mobility performance by coupling with GO. However, the decreasing in degradation efficiency after addition amount of GO was increased to 2 wt% might be caused by the excessive adsorption of Rh-B molecules on the surface of catalyst powder until it was fully covered surface of catalyst, which would inhibit catalyst from absorbing light. Thus, this would limit the radicals that could attack certain dye molecules and leading to decrease in the degradation efficiency.

It can be confirmed the degradation efficiency of BiOBr that not derived from photosensitization reaction by observing the color of BiOBr photocatalyst powders, since it was changed from pink (adsorbed Rh-B molecule) to light gray which is the original color of BiOBr/GO composite, after irradiation. This evidence showed that although the GO plate has very high absorption ability, but the photocatalytic reaction of BiOBr could almost completely eliminate the dye molecule on their surface.

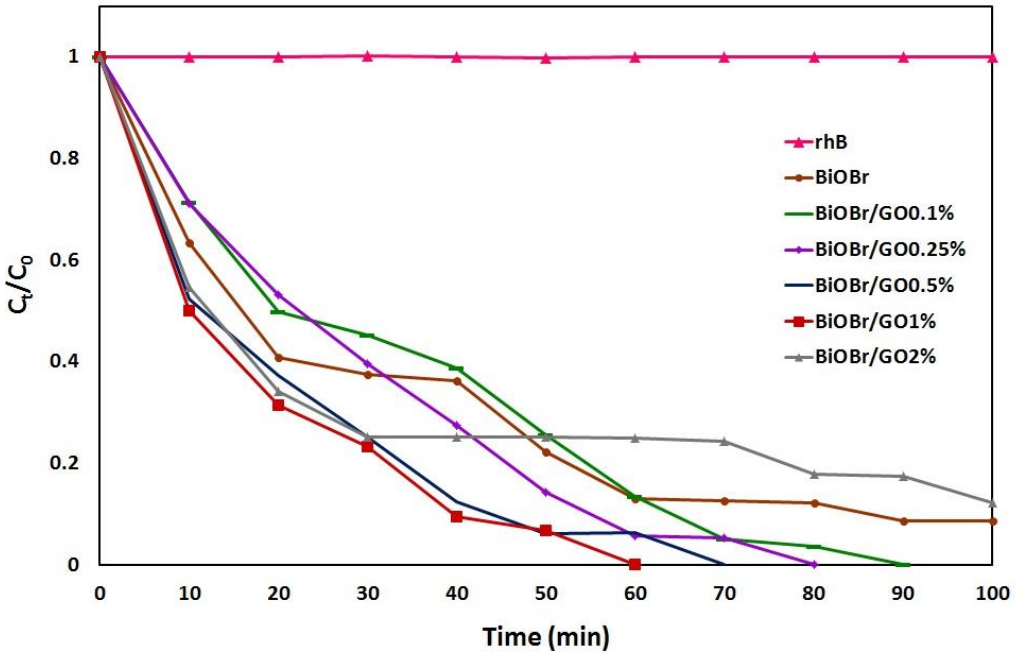

Fig.4.15 The photocatalytic activities for degradation of Rh-B under visible-light irradiation of as-synthesized BiOBr and BiOBr/GO composites.

Table 4.3 Photodegradation efficiency (%) for degradation of Rh-B solution of pure BiOBr and BiOBr/GO composites.

Time (min)	Photodegradation efficiency (%)					
	BiOBr	BiOBr/GO 0.1%	BiOBr/GO 0.25%	BiOBr/GO 0.5%	BiOBr/GO 1%	BiOBr/GO 2%
10	36.50	28.64	28.82	47.76	49.91	45.19
20	59.16	50.28	46.91	62.63	68.61	65.75
30	62.49	54.75	60.38	74.80	76.82	74.78
40	63.68	61.17	72.51	87.62	90.55	74.79
50	77.77	74.47	85.72	93.84	93.14	74.80
60	86.87	86.54	94.22	93.66	100.0	74.83

4.2.6.2 Decomposition of nitrogen oxide gas (NO_x)

The nitrogen oxide gas (NO_x) decomposition efficiency of the prepared samples are presented in Fig. 4.16. Under visible light, the BiOBr/GO composite samples showed higher $DeNo_x$ activity than that of pure BiOBr. The BiOBr/GO composite with 0.1 % GO performed the highest NO_x gas decomposition efficiency with 46.60 % in 10 min. This results show the improved photocatalytic activity of the BiOBr/GO 0.1 % composites in terms of air purification under visible light irradiation. The calculated photodegradation efficiency (%) for removal nitrogen oxide gas in 10 min of pure BiOBr and BiOBr/GO composite were shown in Table 4.4.

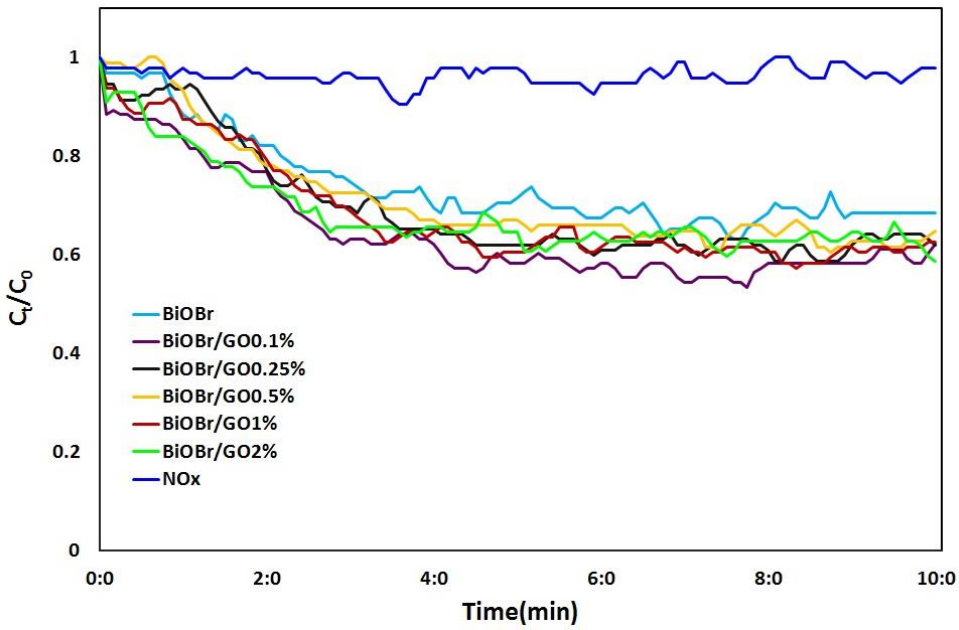

Fig.4.16 Photocatalytic degradation of the nitrogen oxide gas by the as-synthesized BiOBr and BiOBr/GO composites under visible light irradiation.

Table 4.4 Nitrogen oxide gas decomposition efficiency (%) of pure BiOBr and BiOBr/GO composites.

Catalyst	% Degradation
BiOBr	36.84
BiOBr/GO 0.1%	46.60
BiOBr/GO 0.25%	41.30
BiOBr/GO 0.5%	39.56
BiOBr/GO 1%	42.70
BiOBr/GO 2%	43.43

4.3 BiOBr/rGO Composites

4.3.1 X-ray diffraction study

The XRD patterns of the as-synthesized pure BiOBr and BiOBr/rGO composites (0.1, 0.25, 0.5, 1 and 2 %), respectively are shown in Fig. 4.17. All the detectable diffraction peaks for the BiOBr sample at 11.871, 23.691, 26.021, 32.671, 32.741, 40.831, 46.851, 48.771, 54.081, 58.681, and 68.171 degree can be assigned to the tetragonal phase of BiOBr (JCPDS file Card No. 73-2061), indicating a high purity of the sample. For BiOBr/rGO samples, it can be found that the XRD patterns are the same as the BiOBr sample. Furthermore, no typical diffraction peaks of rGO could be observed in the nanocomposites on the XRD patterns, probably due to the low amount of rGO.

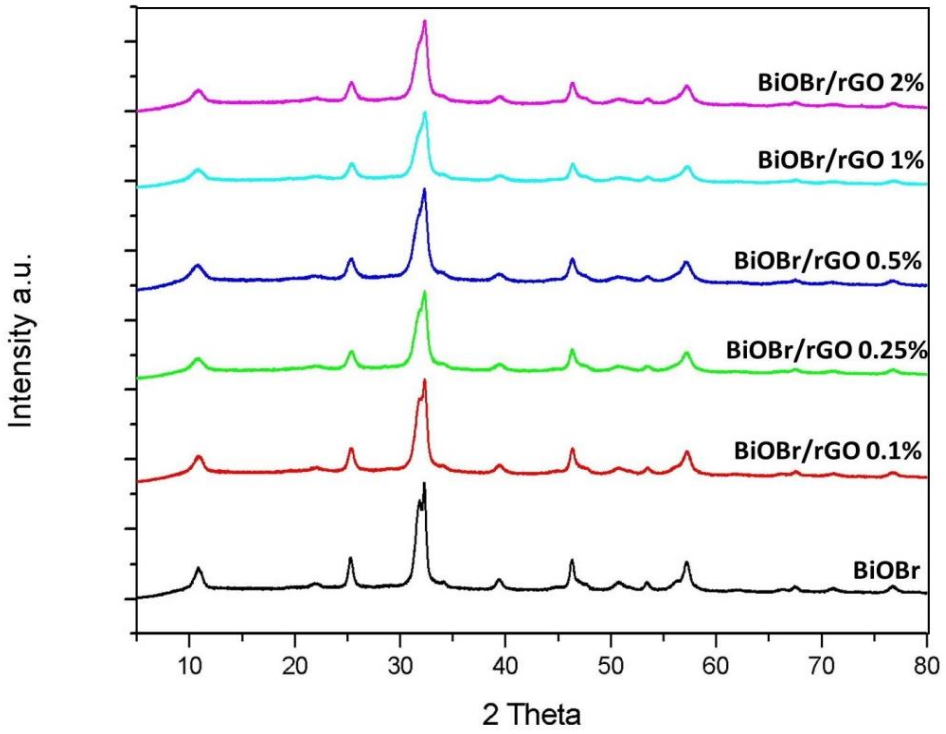

Fig.4.17 XRD diffraction patterns of pure reduced graphene oxide (rGO), pure BiOBr and BiOBr/rGO composites with various amount of rGO.

4.3.2 FE-SEM and TEM analysis

The FE-SEM images in Fig. 4.18 (a-c) show the surface morphologies of reduced graphene oxide (rGO) sheets, pure BiOBr and BiOBr/rGO composites (2 % rGO), respectively. The FE-SEM image in Fig. 4.18 (a) shows that rGO sheet has thin wavy and crinkled morphology. Fig. 4.18 (b) shows the FE-SEM image of BiOBr, and it was found that each microstructure of particle was composed of numerous fine plates. In Fig. 4.18 (c) the FE-SEM images of BiOBr/rGO composites shows that the BiOBr particles are well dispersed on the crinkled surface of rGO sheets. This is evident that surface of rGO sheets interacts with surface of BiOBr particles very well, which should effectively promote the charge transportation and separations for enhancing the photocatalytic activity.

The result in Fig. 4.18 (d) show the TEM image of pure rGO sheet, it demonstrates wrinkled and transparent morphology. In Fig. 4.18 (e) it can be seen that the microstructure of as-synthesized BiOBr is composed of many plates. Fig. 4.18 (f) the TEM image showing the BiOBr plates are randomly dispersed on wrinkled rGO sheets, which was corresponding to FE-SEM result. And the results show that the morphology of BiOBr/rGO is resembled as BiOBr/GO.

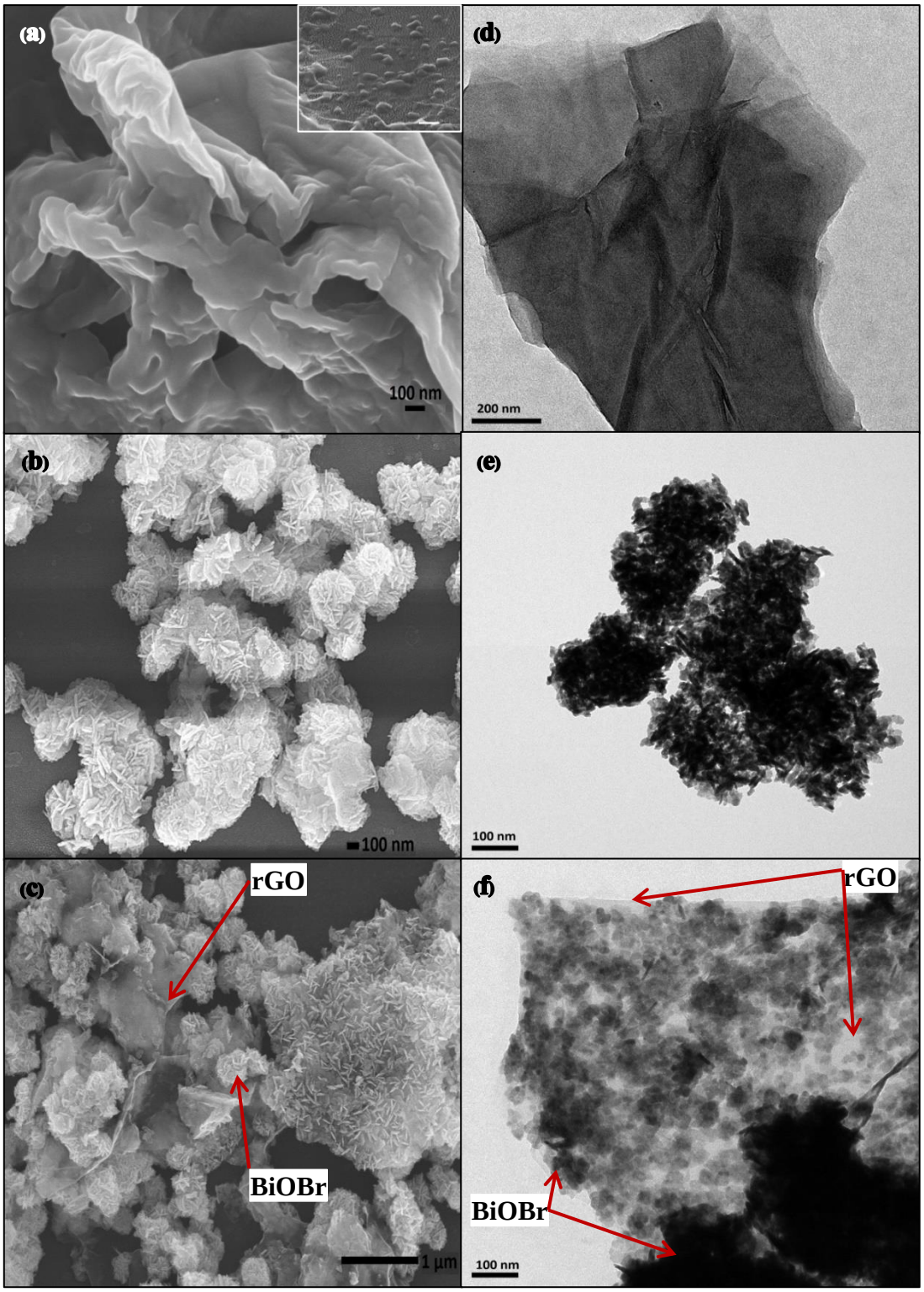

Fig.4.18 FE-SEM images of (a) pure reduced graphene oxide (rGO), (b) pure BiOBr, (c) BiOBr/rGO composites (2 % rGO) and TEM images of (d) pure reduced graphene oxide (rGO), (e) pure BiOBr, (f) BiOBr/rGO composites (2 % rGO).

4.3.3 FT-IR analysis [37]

The FTIR spectra of pure rGO, BiOBr/rGO composites and pure BiOBr were described in Fig. 4.19. The spectrum of rGO shows broad peak around 3421 cm^{-1}coresponds to O-H stretching vibration, a peak at 1718 cm^{-1} was due to the carbonyl stretching vibration respectively, the peaks at 1383 cm^{-1} corresponds to C-O-H stretching vibrations. The peak around 1107 cm^{-1} is due to the C-O stretching vibrations and peak at 1617 cm^{-1} is attributed to vibration of the adsorbed water molecules and due to the vibrations of graphite. The spectrum of pure BiOBr shows peak at 512 cm^{-1} is observed which is primarily due to the Bi–O stretching vibration mode in BiOBr. The FTIR spectrum of BiOBr/rGO composites reveals that the rGO the as-synthesized nanocomposites have been composed of two fundamental components of BiOBr and rGO because the spectrum shows the peak at 512 cm^{-1} corresponds to (Bi-O) vibrations and also the peak corresponding to rGO stretching vibrations appears at the synthesized composites.

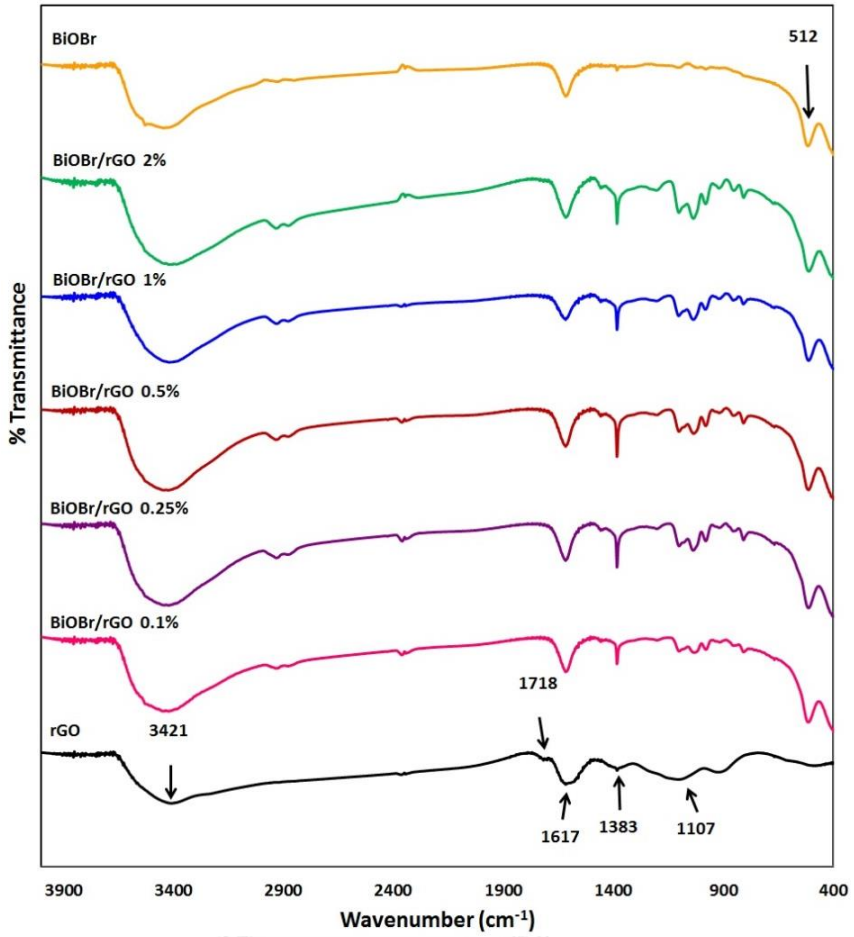

Fig. 4.19 FTIR spectra of pure reduced graphene oxide (rGO), BiOBr/rGO composites and pure BiOBr.

4.3.4 Specific surface area

The specific surface area is an important factor to determine the adsorptive capability of the photocatalysts toward organic contaminant such as dyes. From the results of the nitrogen adsorption-desorption tests, the specific surface area of pure BiOBr and BiOBr/rGO composites with amount of rGO 0.1, 0.25, 0.5, 1 and 2 wt% were shown in Table 4.5. The specific surface area of composites was higher than that of pure BiOBr, in that the increasing in surface area from 20-36 m^2/g, which was related to the increasing amount of rGO from 0-2.0 wt%. In addition, the specific surface areas of BiOBr/rGO composites are close to that of BiOBr/GO composites.

Table 4.5 Specific surface area and band gap energy value (Eg) of pure BiOBr and BiOBr/rGO composites.

Amount of rGO (wt %)	0 %	0.1%	0.25%	0.5%	1%	2%
Specific surface area (m^2/g)	20.66	24.50	27.39	31.39	35.05	36.08
Band energy (eV)	2.9	2.94	2.92	2.9	2.9	2.86

4.3.5 Optical properties

Absorption spectra measurement

The optical absorption of all as-synthesized BiOBr and BiOBr/rGO composites samples were measured by a UV-Vis spectrometer. The results in Fig.4.20 show the UV-Vis diffuse reflectance spectra of the pure BiOBr and BiOBr/rGO composites prepared by the precipitation method. It can be observed that the shift of absorption edge to the visible region slightly increased as the amount of rGO in composites increased. Moreover, for BiOBr/rGO composites, there is an enhanced absorption in the visible light region corresponding to its band gap energy results (2.86- 2.94 eV) as shown in Table 4.5.

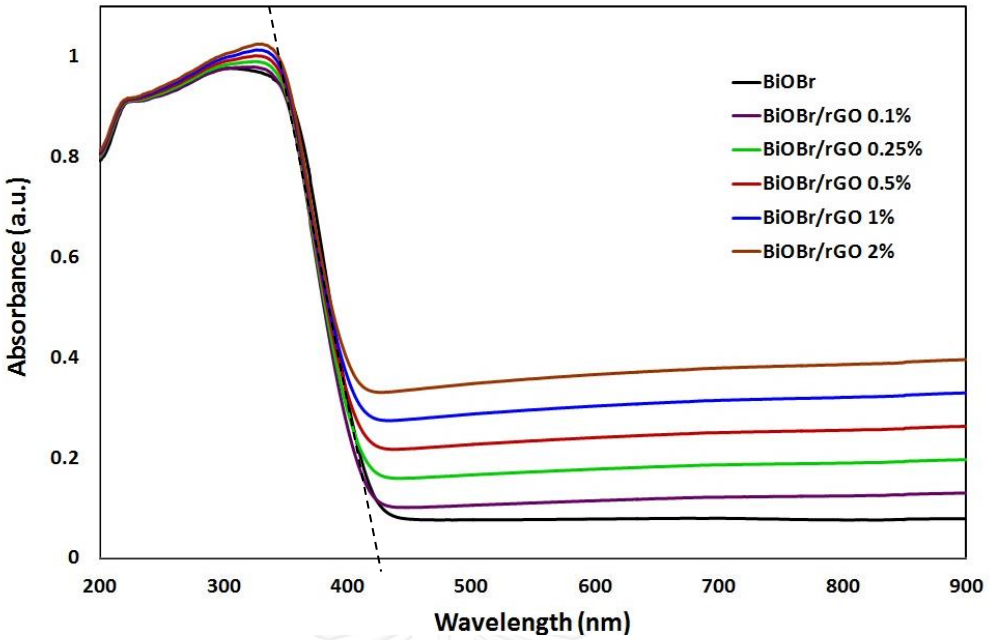

Fig.4.20 The UV-Vis diffuse reflectance spectra of the pure BiOBr and BiOBr/rGO composites

Band gap energy

The optical band gap energy value of as-synthesized BiOBr and BiOBr/rGO composites estimated by linear extrapolation from the inflection point of the $(h\nu A)^{1/2}$ versus $h\nu$ graph to the x-axis was shown in Fig. 4.21. It was indicated that pure BiOBr and BiOBr/rGO composites have small band gap energy about 2.86- 2.94 eV and the band gap energy was slightly decreased as increasing of rGO in composites as shown in Table 4.5. It can be expected that this sample could be responded under visible light.

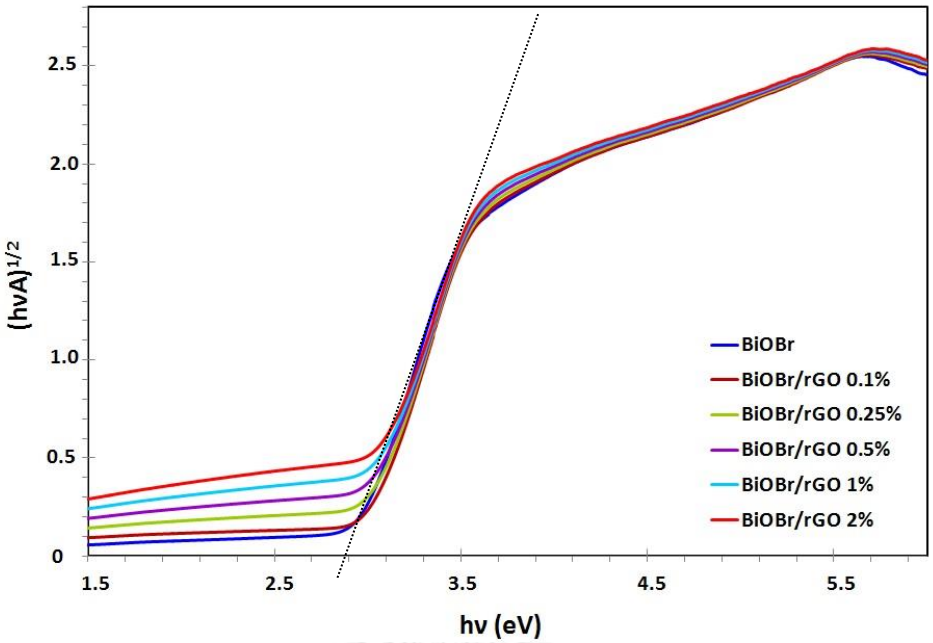

Fig.4.21 Band gap energy of pure BiOBr and BiOBr/rGO composites.

4.3.6 Photocatalytic activity evaluation

4.3.6.1 Rhodamine B (Rh-B) degradation

The results in Fig. 4.22 demonstrate the adsorption–desorption equilibrium of the Rh-B dye on the surface of BiOBr and BiOBr/rGO composites after keeping in dark for 300 min. During experimentation the sample suspensions were kept in dark until there were no change in concentration of Rh-B solution to confirm that they were in equilibrium. The results of adsorption-desorption equilibrium of the Rh-B dye on the surface of BiOBr and BiOBr/rGO composites were attained at a different time with different amount of rGO. It can be observed that the time requirement to attain the adsorption-desorption equilibrium of composites were increased as increasing amount of rGO in composites. Since the surface area of photocatalyst plays an important role on the adsorption, so the adsorption-desorption equilibrium time increased might be caused by the increasing in surface area of composite when coupling with rGO.

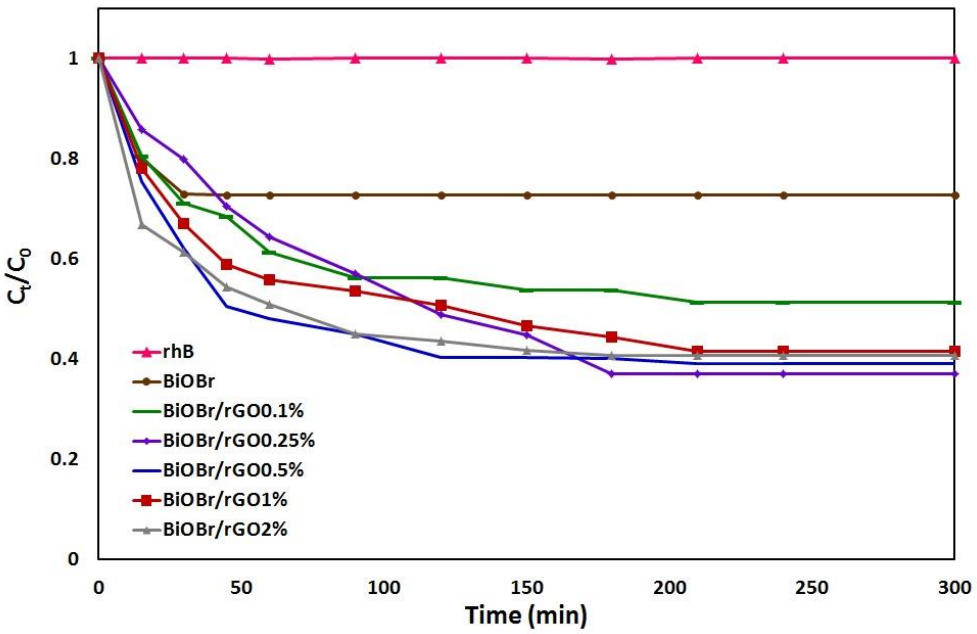

Fig.4.22 The change in concentration of Rh-B solution with time in the presence of BiOBr and BiOBr/rGO composites in dark.

The photocatalytic activities of the as-synthesized samples were evaluated by measuring the degradation of Rhodamine B (Rh-B) in the aqueous solution under visible light irradiation. The changes in the concentration of Rh-B were checked by examining the variations in maximal absorption in UV-Vis spectra at 556 nm. As shown in Fig.4.23 and Table 4.6, the composite samples consisted of rGO 0.25-1wt% exhibited higher Rh-B degradation efficiency than that of pure BiOBr. When added 1 % of rGO the composite displayed the highest catalytic efficiency for Rh-B photodegradation, which is 100% in 50 min. This indicated that the optimum amount of rGO on the photocatalytic activity enhancement is 1%. It supposed that the increase in photocatalytic degradation of Rh-B was attributed to the enhanced dye adsorption and charge transportation performance by coupling with rGO. However excessive absorption of Rh-B molecules on the surface of BiOBr/rGO (2 %) composite resulted in decrease the photodegradation efficiency. It could be described reason by the same explanation as in a case of BiOBr/GO.

Since BiOBr color was changed from pink (adsorbed Rh-B molecule) to light gray which is the original color of BiOBr/rGO composite, after irradiation. This result can be confirmed that BiOBr could almost completely eliminate the dye molecule on their surface by its photocatalytic reaction.

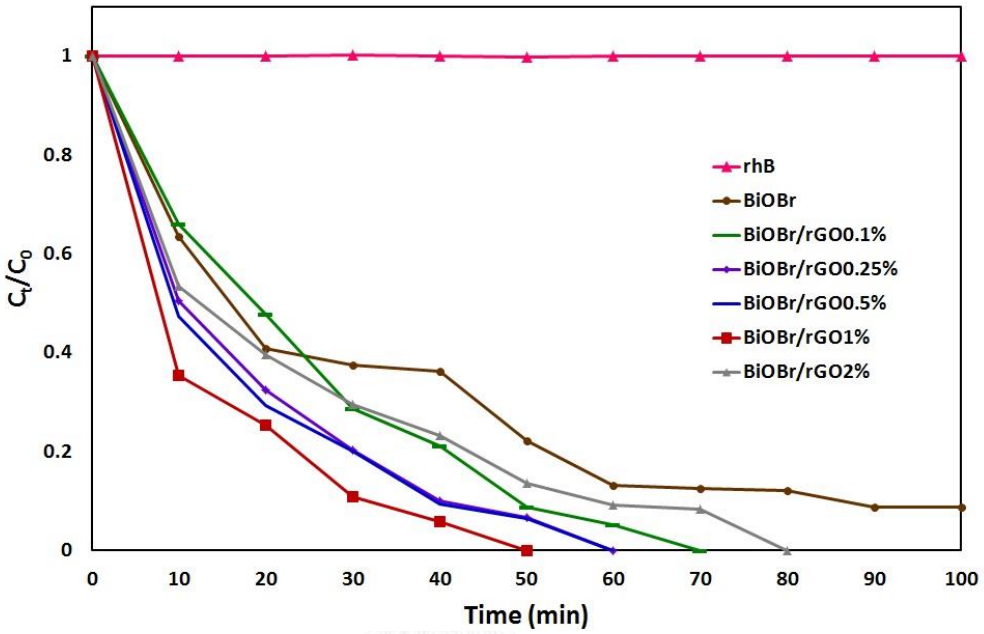

Fig.4.23 The photocatalytic activities for degradation of Rh-B under visible-light irradiation of as-synthesized BiOBr and BiOBr/rGO composites.

Table 4.6 Photodegradation efficiency (%) for degradation of Rh-B solution of pure BiOBr and BiOBr/rGO composites.

Time (min)	Photodegradation efficiency (%)					
	BiOBr	BiOBr/rGO 0.1%	BiOBr/rGO 0.25%	BiOBr/rGO 0.5%	BiOBr/rGO 1%	BiOBr/ rGO 2%
10	36.50	39.54	67.06	58.82	72.67	51.53
20	59.16	56.29	78.81	74.44	80.40	64.04
30	62.49	73.66	86.83	82.41	91.63	73.18
40	63.68	80.62	93.44	91.75	95.39	78.92
50	77.77	91.95	95.69	94.31	100	87.72
60	86.87	95.26	100	100	-	91.70

4.3.6.2 Decomposition of nitrogen oxide gas (NO_x)

The nitrogen oxide gas (NO) decomposition results of the prepared sample are presented in Fig. 4.24. Under visible light, the sample BiOBr/rGO 0.25 % showed the highest efficiency with 50 % of NO_x in 10 min. This result improved the NO_x decomposition performance of the BiOBr/rGO 0.25 % composites under visible light irradiation. The results of photodegradation efficiency (%) for removal nitrogen oxide gas of pure BiOBr and BiOBr/rGO composite were shown in Table 4.7.

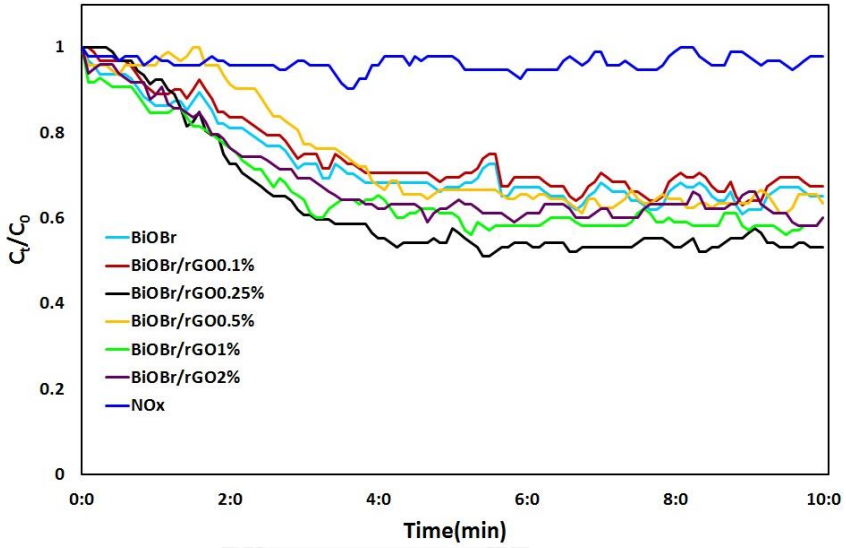

Fig.4.24 Photocatalytic degradation of the nitrogen oxide gas by the as-synthesized BiOBr and BiOBr/rGO composites under visible light irradiation

Table 4.7 Nitrogen oxide gas decomposition efficiency (%) of pure BiOBr and BiOBr/rGO composites.

Catalyst	% Degradation
BiOBr	36.84
BiOBr/rGO 0.1%	38.04
BiOBr/rGO 0.25%	50
BiOBr/rGO 0.5%	38.70
BiOBr/rGO 1%	43.87
BiOBr/rGO 2%	41.83

4.4 BiOBr/g-C_3N_4 Composites

4.4.1. X-ray diffraction study

The XRD patterns of the as- synthesized pure BiOBr and BiOBr/ g- C_3N_4 composites (0.1, 0.25, 0.5, 1 and 2 %) are show in Fig. 4.25. The pure g-C_3N_4 sample presents two typical diffraction peaks at 13.03 and 27.60 degree, which can correspond to the indexed as (002) and (100) diffraction planes (JCPDS 87-1526), respectively (see appendix B). All the detectable diffraction peaks for the BiOBr sample at 11.871, 23.691, 26.021, 32.671, 32.741, 40.831, 46.851, 48.771, 54.081, 58.681, and 68.171 degree can be assigned to the tetragonal phase of BiOBr (JCPDS file Card No. 73-2061), indicating a high purity of the sample. For BiOBr/ g- C_3N_4 samples, it can be found that the XRD patterns are the same as the pure BiOBr sample. Furthermore, no typical diffraction peaks of g- C_3N_4 could be observed in the composites on the XRD patterns, probably due to the small amount of g-C_3N_4 in composites.

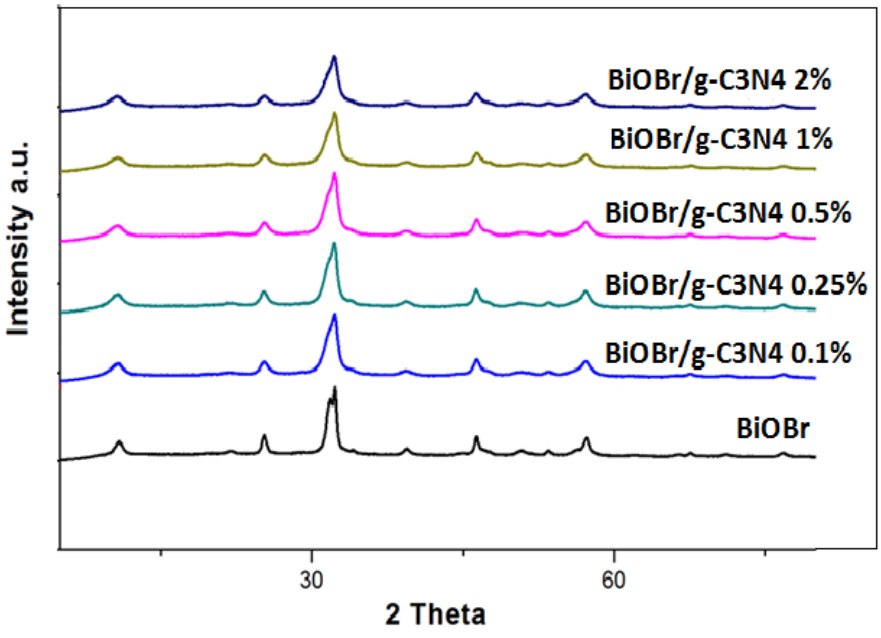

Fig. 4.25 XRD diffraction patterns of pure BiOBr and BiOBr/g-C_3N_4 composites with various amount of g-C_3N_4.

4.4.2 SEM and TEM analysis

The FE-SEM images in Fig. 4.26 (a-c) show the surface morphologies of pure graphite like carbon nitride (g-C_3N_4), pure BiOBr and BiOBr/ g-C_3N_4 composites (2 % g-C_3N_4), respectively. The FE-SEM image in Fig. 4.26 (a) shows that the morphology of g-C_3N_4 sheets is composed of lamellar structure. Fig. 4.26 (b) shows the FE-SEM images of pure BiOBr, and it found that each microstructured particle is composed of numerous fine plates. In Fig. 4.26 (c) the FE-SEM images of BiOBr/ g-C_3N_4 composites shows that the BiOBr particles are well dispersed on the wrinkle surface of g-C_3N_4 sheets. This is evident that g-C_3N_4 have surface interaction with BiOBr excellently.

Fig. 4.26 (d) shows the TEM image of pure g-C_3N_4 sheets which is wrinkle and transparent morphology. In Fig. 4.26 (e), it can be seen that the microstructure of as-synthesized BiOBr is composed of many fine plates. Fig. 4.26 (f) clearly demonstrates the existence of BiOBr particles on g–C_3N_4 sheet which is good agreement with FESEM results.

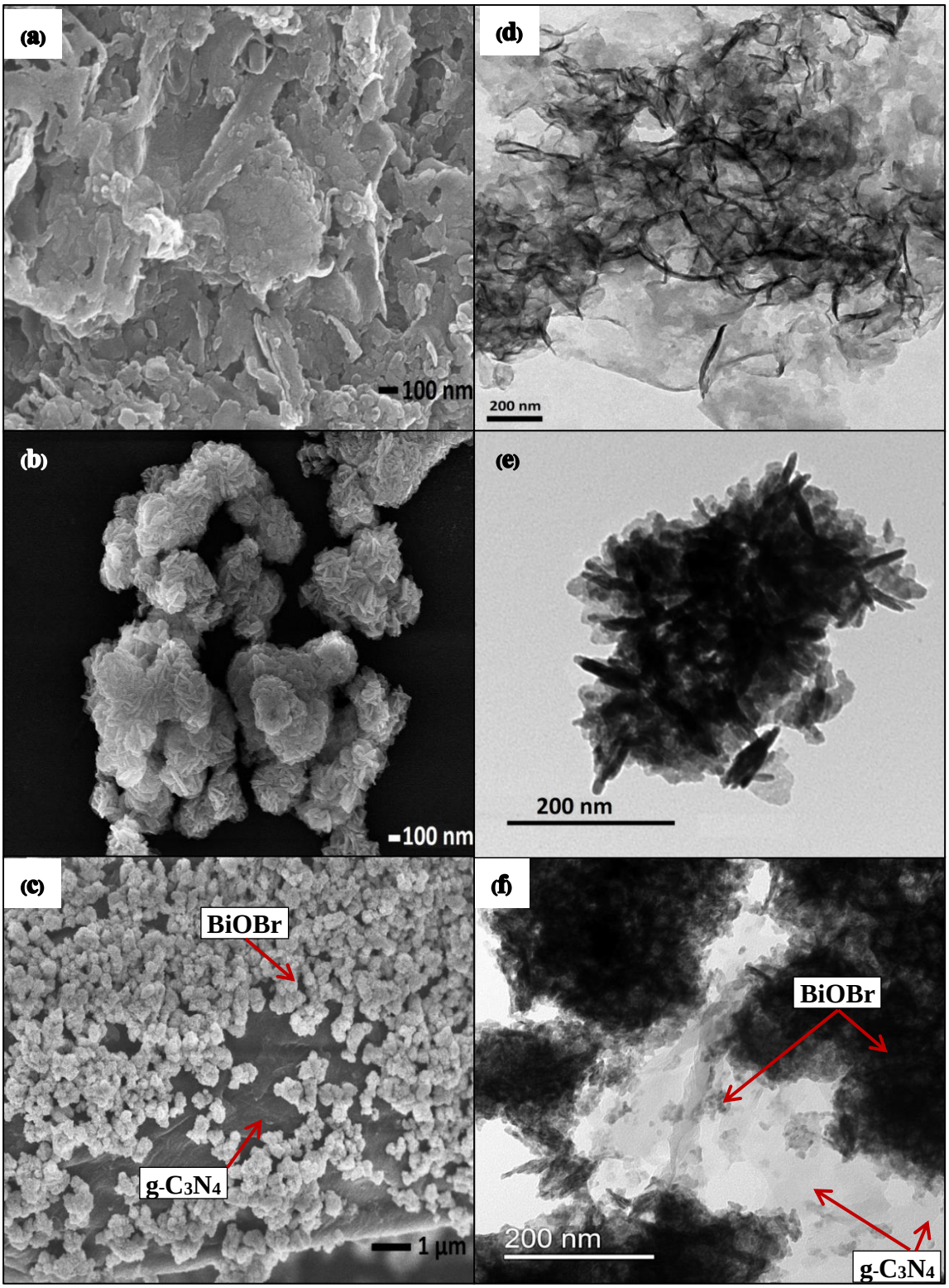

Fig.4.26 FE-SEM images of (a) pure graphite like carbon nitride (g-C_3N_4), (b) pure BiOBr, (c) BiOBr/ g-C_3N_4 composites (2 % g-C_3N_4) and TEM images of (d) pure graphite like carbon nitride (g-C_3N_4), (e) pure BiOBr, (f) BiOBr/ g-C_3N_4 composites (2 % g-C_3N_4).

4.4.3. FT-IR analysis [49]

The FTIR spectra of pure g-C_3N_4, BiOBr/g-C_3N_4 composites and pure BiOBr were presented in Fig. 4.27. The broad absorption peaks of g-C_3N_4 at 3040-3291 cm^{-1} are stretching vibration modes of N-H and O-H groups, indicating the existence of uncondensed amino groups and absorbed H_2O molecules. The peaks in range at 1230-1570 cm^{-1} observed in g-C_3N_4 are related to the typical stretching modes of C-N heterocycle, whereas the peak at 1636 cm^{-1} corresponds to the C=N stretching vibration mode. The intense peak at 811 cm^{-1} represented the out of plane bending modes of s-triazine ring. Moreover, the broad peak at 512 cm^{-1} in the spectrum of BiOBr and BiOBr/g-C_3N_4 composites correspond to the stretching of Bi-O, the peak becomes weak with the introduction of g-C_3N_4. The structures of BiOBr/g-C_3N_4 have little changes during the self-assembly process. All typical absorption regions of g-C_3N_4 appear in the BiOBr/g-C_3N_4 composites, which further confirm that the as-synthesized composites are composed of both g-C_3N_4 and BiOBr.

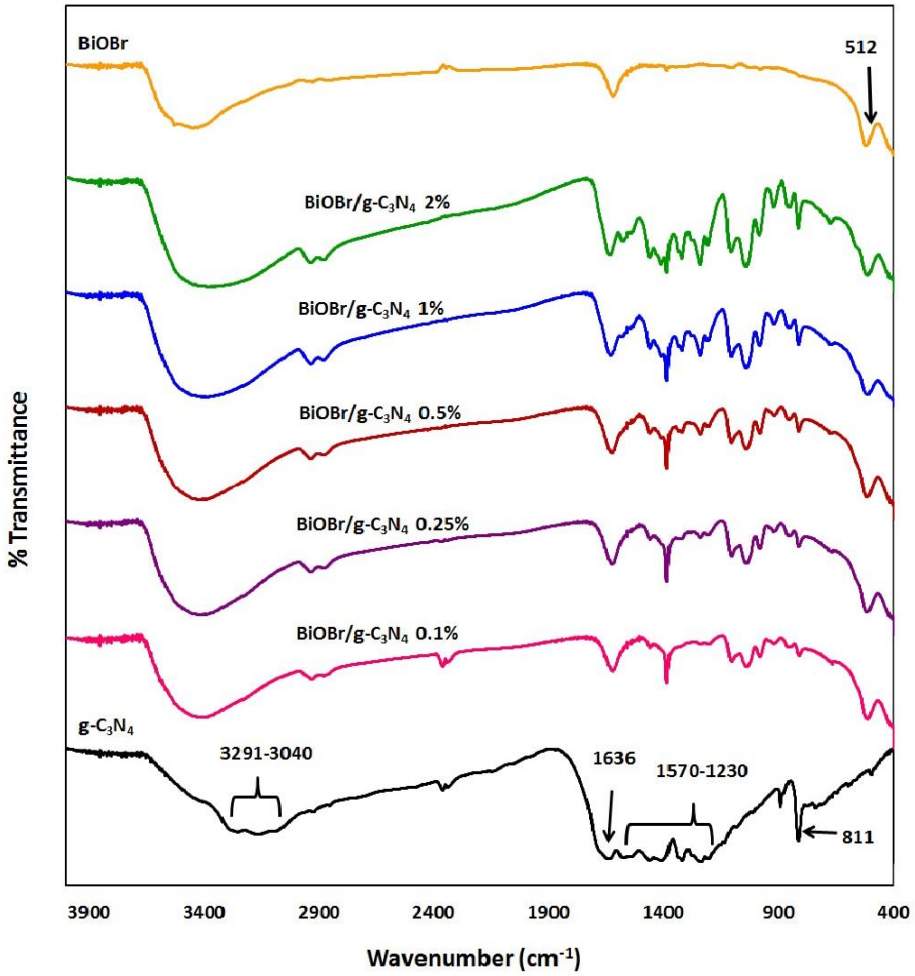

Fig.4.27 FTIR spectra of pure g-C_3N_4, BiOBr/g-C_3N_4 composites and pure BiOBr.

4.4.4 Specific surface area

The specific surface area is an important factor to determine the adsorptive capability of the photocatalysts toward organic contaminant such as dyes. From the results of the nitrogen adsorption-desorption tests, the specific surface area of pure BiOBr and BiOBr/ g-C_3N_4 composites with amount of g-C_3N_4 0.1, 0.25, 0.5, 1 and 2 wt% were shown in Table 4.8. The specific surface area of BiOBr did not change very much by coupling with g-C_3N_4 and the samples possessed the specific surface area about 20 m^2/g.

Table 4.8 Specific surface area and band gap energy value (Eg) of pure BiOBr and BiOBr/g-C_3N_4 composites.

Amount of g-C_3N_4 (wt %)	0 %	0.1%	0.25%	0.5%	1%	2%
Specific surface area (m^2/g)	20.66	20.64	20.43	20.32	20.16	20.15
Band energy (eV)	2.9	2.9	2.9	2.9	2.88	2.88

4.4.5 Optical properties

Absorption spectra measurement

The optical absorption of all of the as-synthesized BiOBr and BiOBr/g-C_3N_4 composites samples were measured by a UV-Vis spectrometer. Fig.4.28 shows the UV-Vis diffuse reflectance spectra of pure BiOBr and BiOBr/g-C_3N_4 composites prepared by the precipitation method and it apparently, all of samples showed the strong absorption edges in the visible-light region corresponding to its band gap energy resulted (2.88-2.9 eV) as shown in Table 4.8.

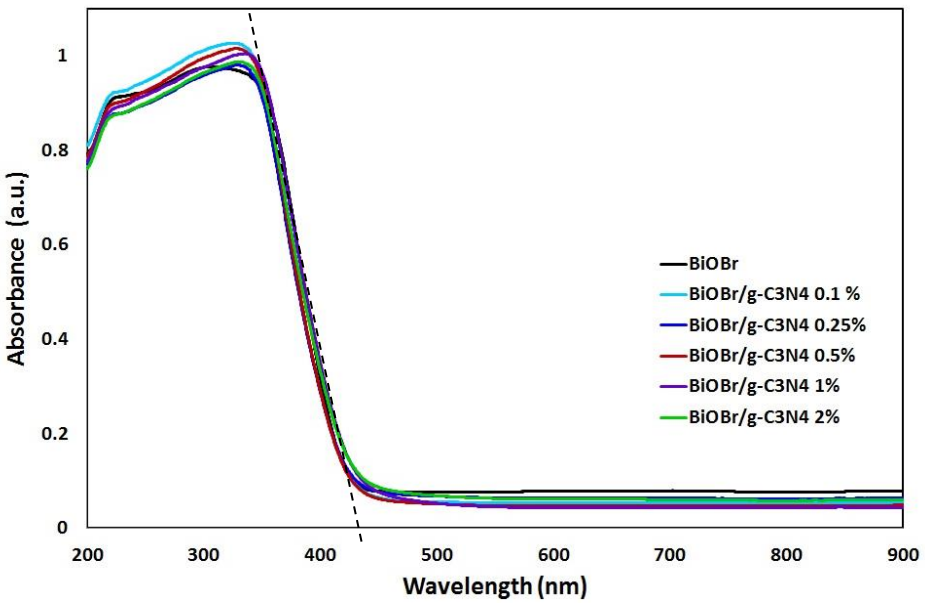

Fig.4.28 The UV-Vis diffuse reflectance spectra of the pure BiOBr and BiOBr/g-C_3N_4 composites

Band gap energy

The optical band gap energy value of as-synthesized BiOBr and BiOBr/g-C_3N_4 composites estimated by linear extrapolation from the inflection point of the $(h\nu A)^{1/2}$ versus $h\nu$ graph to the x-axis was shown in Fig.4.29. It was indicated that pure BiOBr and BiOBr/g-C_3N_4 composites have small band gap energy about 2.88-2.9 eV and it can be expected that this sample could be activated under visible light due to its narrow band gab energy.

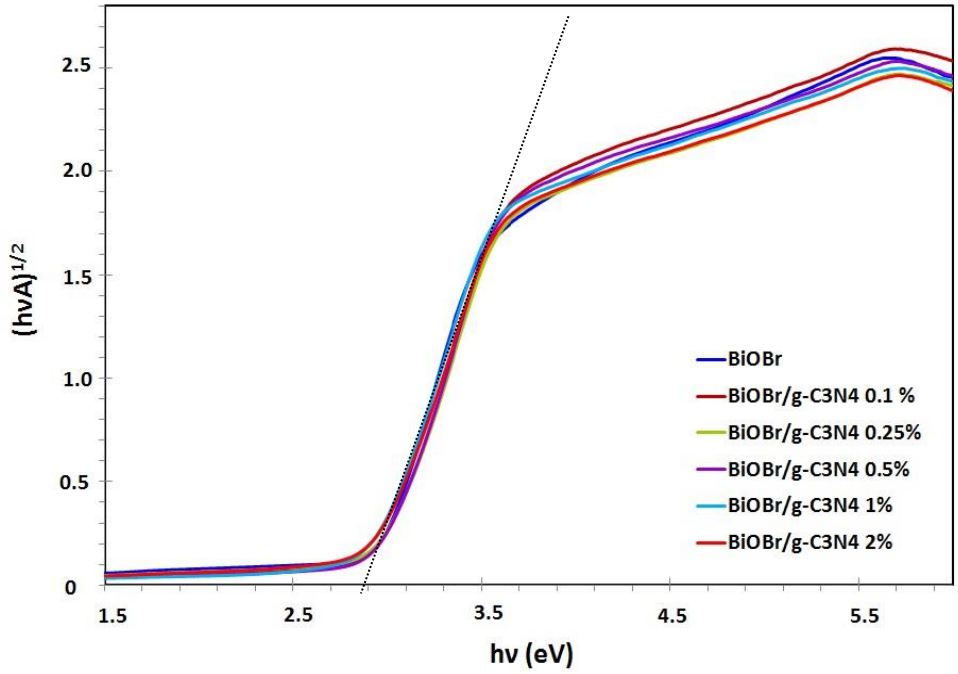

Fig.4.29 Band gap energy of pure BiOBr and BiOBr/g-C_3N_4 composites.

4.4.6. Photocatalytic activity evaluation

4.4.6.1 Rhodamine B (Rh-B) degradation

The results in Fig 4. 30 demonstrating that the adsorption– desorption equilibrium of the Rh-B dye on the surface of BiOBr and BiOBr/g-C_3N_4 composites were attained after keeping in dark for 300 min, confirming they were in equilibrium. It can be observed that the increasing amount of g- C_3N_4 in composites enhanced the adsorption ability. As the results, it can be observed that the composite coupling with

g-C_3N_4 showed higher adsorption of Rh-B dye than that of GO and rGO, in which longer time to attained adsorption-desorption equilibrium was required.

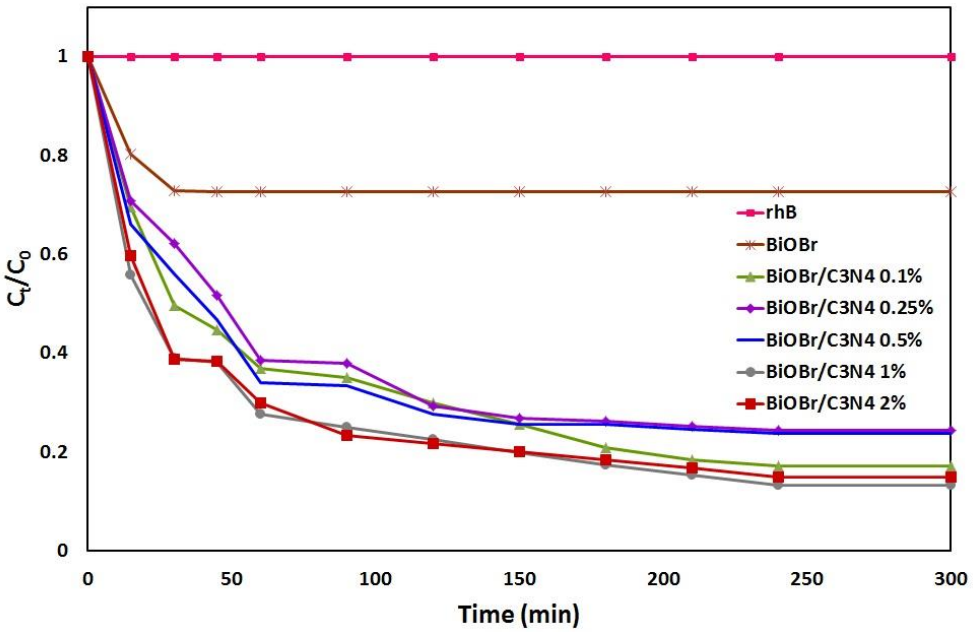

Fig.4.30 The change in concentration of Rh-B solution with time in the presence of BiOBr and BiOBr/g-C_3N_4 composites in dark**.**

The photocatalytic activities of the as-synthesized samples were evaluated by measuring the degradation of Rhodamine B (Rh-B) in the aqueous solution under visible light irradiation. The changes in the concentration of Rh-B were checked by examining the variations in maximal absorption in UV-Vis spectra at 556 nm. As shown in Fig.4.31, the highest photodegradation efficiency reached at 100% in 50 min was obtained with BiOBr/g-C_3N_4 2 % composite. It was demonstrated that the increasing in photocatalytic degradation of Rh-B as the amount of g-C_3N_4 increased in composite, might be due to the synergistic effects of photocatalytic activity from g-C_3N_4 (see appendix C) and charge separation transportation enhancement when coupling with g-C_3N_4 semiconductor. Moreover, the high absorption ability of g-C_3N_4 increased the concentration of dye molecules on the surface of catalysts, resulted in the enhancement photodegradation rate.

At the end of the reaction, colors of BiOBr/g-C_3N_4 composites were turned to cream color which is the original color of BiOBr/g-C_3N_4 composites. This is obviously that BiOBr/g-C_3N_4 composites could almost completely eliminate the dye molecule on their surface. The results of photodegradation efficiency (%) for degradation of Rh-B solution of pure BiOBr and BiOBr/g-C_3N_4 composite were shown in Table 4.9.

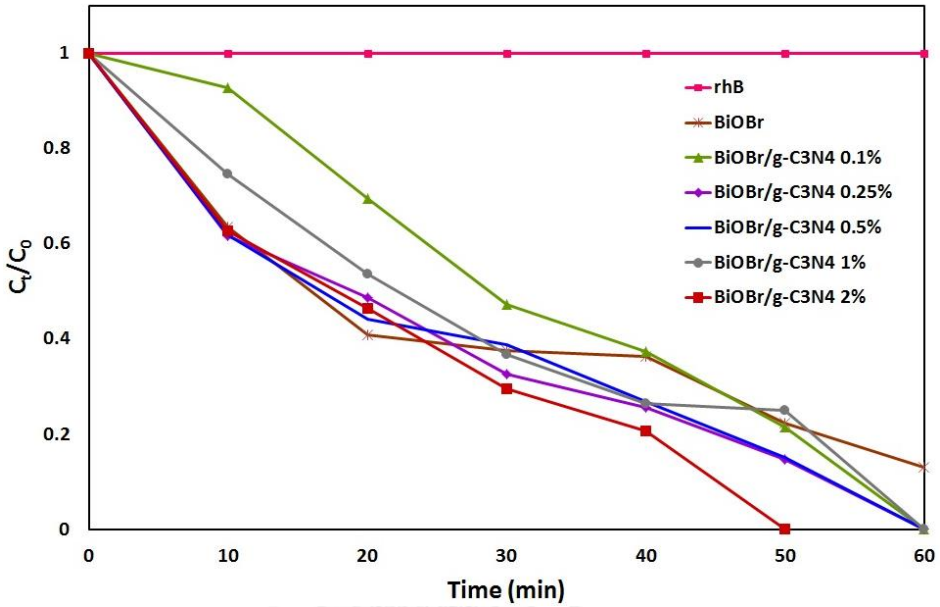

Fig.4.31 The photocatalytic activities for degradation of Rh-B under visible-light irradiation of as-synthesized BiOBr and BiOBr/g-C_3N_4 composites.

Table 4.9 Photodegradation efficiency (%) for degradation of Rh-B solution of pure BiOBr and BiOBr/g-C_3N_4 composites.

Time (min)	Photodegradation efficiency (%)					
	BiOBr	BiOBr/g-C_3N_4 0.1%	BiOBr/g-C_3N_4 0.25%	BiOBr/g-C_3N_4 0.5%	BiOBr/g-C_3N_4 1%	BiOBr/g-C_3N_4 2%
10	36.50	54.66	60.44	56.15	63.01	67.77
20	59.16	66.02	68.70	68.68	73.45	76.12
30	62.49	76.96	79.08	72.44	81.77	84.84
40	63.68	81.76	83.60	81.00	86.92	89.37
50	77.77	89.45	90.52	89.25	87.66	100
60	86.87	100	100	100	100	-

4.4.6.2 Decomposition of nitrogen oxide gas (NO_x)

In the nitrogen oxide gas (NO) decomposition process the prepared sample are presented in Fig.4.32. Under visible light, the sample BiOBr/g-C_3N_4 2 % showed the highest photodegradation efficiency with 52.08 % of nitrogen oxide gas in 10 min this result improved photocatalytic activity of the BiOBr/g-C_3N_4 2 % composites in terms of air purification under visible light irradiation. The results of photodegradation efficiency (%) for removal nitrogen oxide gas of pure BiOBr and BiOBr/g-C_3N_4 composite were shown in Table 4.10.

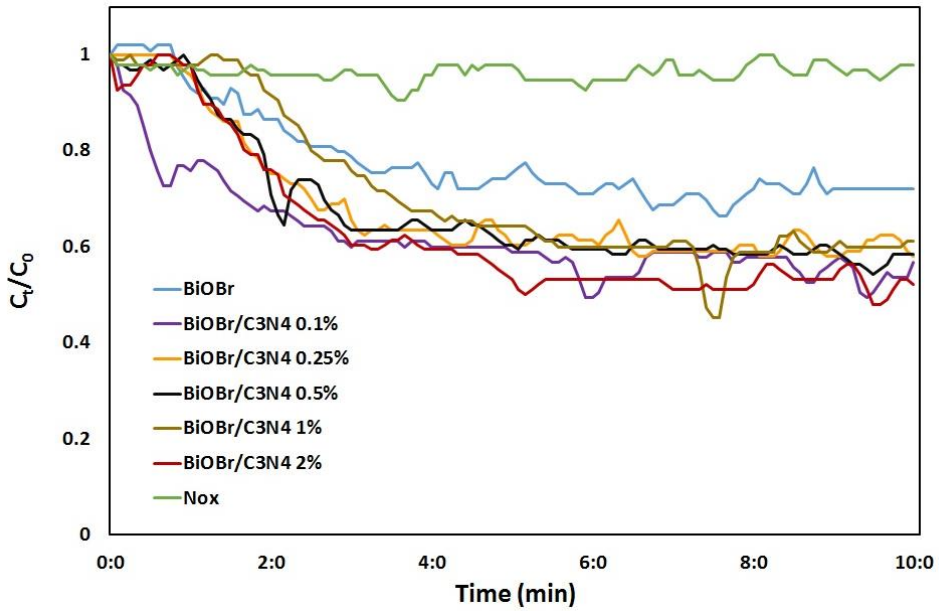

Fig 4.32 Photocatalytic degradation of the nitrogen oxide gas by the as-synthesized BiOBr and BiOBr/g-C_3N_4 composites under visible light irradiation

Table 4.10 Nitrogen oxide gas decomposition efficiency (%) of pure BiOBr and BiOBr/g-C_3N_4 composites.

Catalyst	% Degradation
BiOBr	36.84
BiOBr/g-C_3N_4 0.1%	50.52
BiOBr/g-C_3N_4 0.25%	41.93
BiOBr/g-C_3N_4 0.5%	45.83
BiOBr/g-C_3N_4 1%	44.21
BiOBr/g-C_3N_4 2%	52.08

4.5 Reusability

4.5.1. Rhodamine B (Rh-B) degradation

Reusability of a photocatalyst is a very important parameter from an economical view point. To examine the reusability of the composites, the degradation experiments using recycled sample were carried out 3 cycles and the results are demonstrated in Fig.4.33. In each run, the used composites were separated, washed and dried at 60 °C for 24 h., then they were used repeatedly. As can be seen, after using the photocatalyst for three successive runs under visible light irradiation, the BiOBr/rGO 1% and BiOBr/g-C_3N_4 2% composites revealed a little decrease in its activity. So, suggesting that the BiOBr/rGO 1% and BiOBr/g-C_3N_4 2% composites had high stability which could almost maintain its photocatalytic performance (85-90% degradation efficiency). While pure BiOBr/GO and pure BiOBr showed abrupt decrease in photocatalytic performane to about 40 and 12 %, respectively. As the results, it can be concluded that rGO and g-C_3N_4 enabled to improve stability of BiOBr.

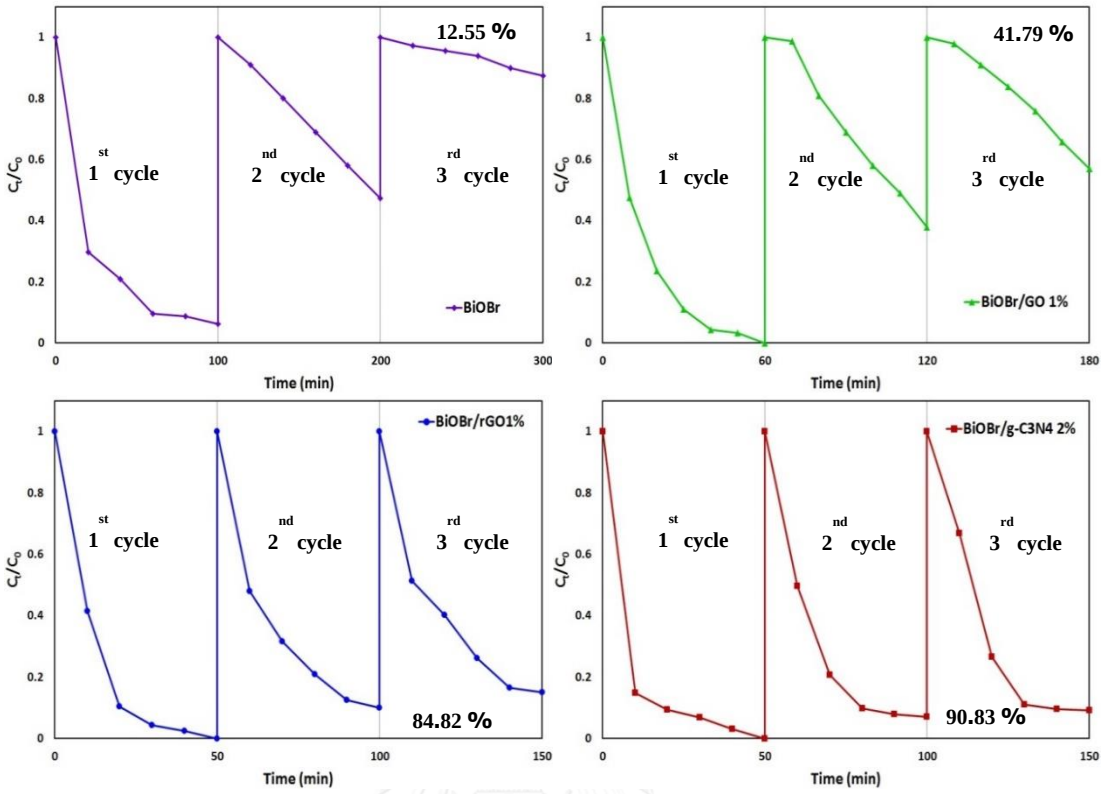

Fig 4.33 Reusability test for the photocatalytic degradation of Rh-B solution over composites for three successive runs under visible light irradiation

4.5.2. Removal of nitrogen oxide gas (NO_x)

Fig 4.34 shows the reusability for the nitrogen oxide gas decomposition of composites. After three successive recycles of samples for photocatalytic reactions under visible light irradiation, the activity of BiOBr/rGO 1% composite remained almost constant and also the BiOBr/g-C_3N_4 2% composite was almost the same. Hence, these photocatalysts have a good life time during the nitrogen oxide gas degradation reaction. The obtained results were corresponded with Rh-B degradation test.

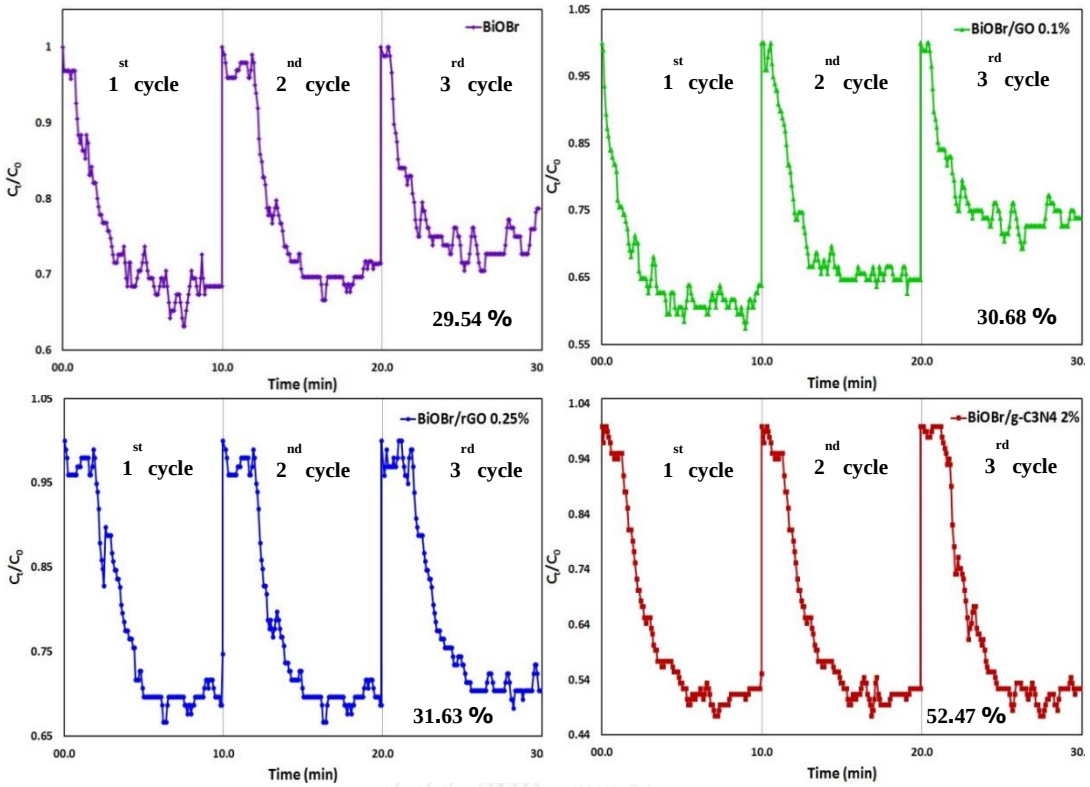

Fig 4.34 Reusability test for the photocatalytic removal of NO gas over composites for three successive runs under visible light irradiation

4.6 Discussion

This study proposed that coupling BiOBr with GO, rGO and g-C_3N_4 could reduce the recombination of photogenerated electron and hole, since higher performance in Rh-B decomposition and NO_x decomposition in BiOBr/GO, rGO and g-C_3N_4 composites comparing with pure BiOBr was observed. To confirm the assumption, advanced characterization apparatus and techniques are required to obtain quantum efficiency [4].

The decrease in recombination of photogenerated electrons and holes pair resulting in the enhanced photocatalytic activity of the BiOBr/GO composites and BiOBr/rGO composites can be attributed to the main reasons:

1) Effective charge transportation and separations arisen from the physical bonding between BiOBr particles and GO/rGO sheet. The enhancement of charge

transportation and separations led to decrease in recombination of photogenerated electron-hole pair by transfer to GO and rGO sheets [6]. The Schematic illustration of the visible light photocatalytic enhancement of BiOBr-based composites was shown in Fig 4.35.

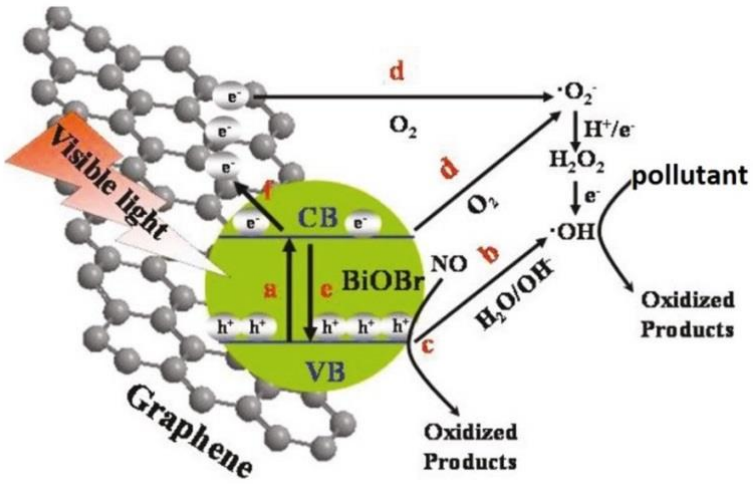

Fig 4.35 The Schematic illustration of the visible light photocatalytic enhancement of BiOBr-based composites [6]

2) Normally, the pure BiOBr shows photocatalytic activity toward •OH. Thereby another presumption (as shown in Fig. 4.36) is the introduction of the GO and rGO might enhance the activity of visible-light responsive BiOBr photocatalyst by elevating the minimum of conduction band of the BiOBr/GO, rGO composites to be higher than the redox potential of E^0 (O_2 / O_2• $^-$). Thus, BiOBr/GO, rGO composites showed high photocatalytic activity for O2• – and •OH photocatalytic production under visible-light irradiation [39].

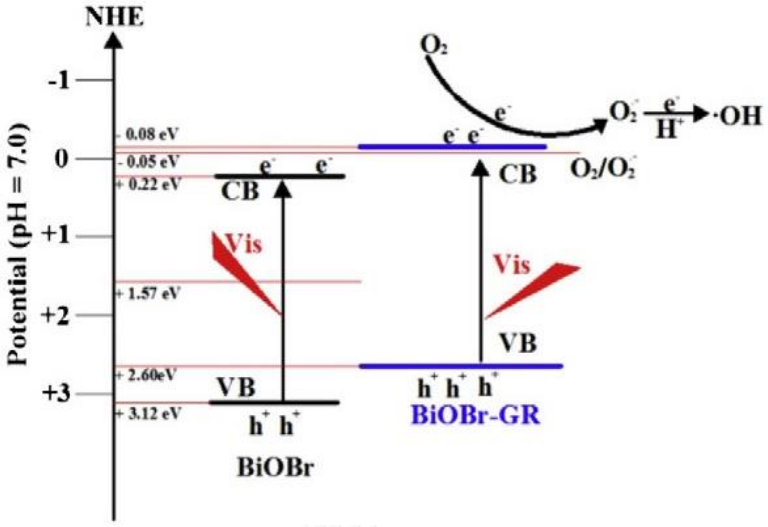

Fig. 4.36 The determined band edges of BiOBr and BiOBr/GR versus NHE [39].

The photocatalytic activity of BiOBr/ g- C_3N_4 composites were significantly enhanced for the degradation of Rh-B dye solution and removal of NO gas in air under visible light irradiation, which can be expected to the highly efficient separation of photo-induced charges transfer between BiOBr and g-C_3N_4. The mechanism was shown in Fig. 4.37, the band structures of the two components are evenly matched with each other. Both of BiOBr and g- C_3N_4 can be excited by visible light and then generate photo- induced electrons and holes. The relative CB and VB edge positions of g- C_3N_4 sheet and BiOBr particle signify that the well- matched band energies can form heterojunctions. The excited electrons in CB of g-C_3N_4 can transfer to CB of BiOBr and excited holes in VB of BiOBr can transfer to VB of g- C_3N_4, which results in efficient separation and transport of photo-induced electrons and holes [47].

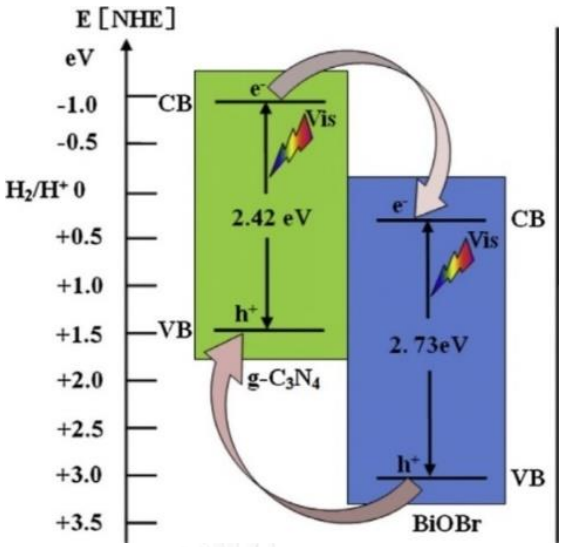

Fig. 4.37 Schematic illustration of the band-gap matching of BiOBr/g-C_3N_4 composites [49]

CHAPTER V

CONCLUSION

In this study, BiOBr and BiOBr-based composites; BiOBr/GO, BiOBr/rGO and BiOBr/g-C_3N_4, have been successfully synthesized by a facile precipitation method at room temperature. The enhanced photocatalytic activity of composites under visible-light evaluated by Rh-B degradation and nitrogen gas decomposition was achieved by hybriding/coupling BiOBr with GO/rGO or g-C_3N_4. It was suggested that the amount of GO/rGO or g-C_3N_4 in the composites played an important role on the enhancement of photocatalytic efficiency. Moreover, it was shown that the hybriding/coupling BiOBr with GO/rGO or g-C_3N_4 could improve the stability of BiOBr for reusing. As the results, it can be summarized that;

- The photocatalytic efficiency for Rh-B degradation under visible light of BiOBr/g-C_3N_4 and BiOBr/rGO was higher than that of BiOBr/GO. The highest activity of each composite was obtained as follow; BiOBr/g-C_3N_4 (2 wt %), BiOBr/rGO (1wt %) and BiOBr/GO (1wt %)
- The photocatalytic efficiency for NO_x gas decomposition under visible light of BiOBr/g-C_3N_4 was higher than that of BiOBr/rGO and BiOBr/GO, respectively. The highest activity of each composite was obtained as follow; BiOBr/g-C_3N_4 (2 wt %), BiOBr/rGO (0.25wt %) and BiOBr/GO (0.1wt %).
- The BiOBr/g-C_3N_4 (2 wt %) composite exhibited the highest reuse ability after photocatalytic activity testing for 3 cycles, followed by BiOBr/rGO and BiOBr/GO, respectively.

The photocatalytic activity of BiOBr-based composites were significantly enhanced for the degradation of Rh-B dye solution and removal of NO_x gas in air under visible light irradiation, which can be ascribed to the highly efficient separation of photo-induced charges transfer between BiOBr - GO, rGO and g-C_3N_4.

The good photocatalytic activity and high stability for recycling of the as synthesized BiOBr- based composites exhibited promising potential to use as photocatalysts for water and air purification applications.

REFERENCES

1. Wang, C.-y., D.W. Bahnemann, and J.K. Dohrmann, *A novel preparation of iron-doped TiO_2 nanoparticles with enhanced photocatalytic activity.* Chemical Communications, 2000(16): p. 1539-1540.

2. Tang, J., Z. Zou, and J. Ye, *Efficient Photocatalytic Decomposition of Organic Contaminants over CaBi2O4 under Visible-Light Irradiation.* Angewandte Chemie International Edition, 2004. **43**(34): p. 4463-4466.

3. Li, Q., et al., *Highly Efficient Visible-Light-Driven Photocatalytic Hydrogen Production of CdS-Cluster-Decorated Graphene Nanosheets.* Journal of the American Chemical Society, 2011. **133**(28): p. 10878-10884.

4. Fujishima, A., T.N. Rao, and D.A. Tryk, *Titanium dioxide photocatalysis.* Journal of Photochemistry and Photobiology C: Photochemistry Reviews, 2000. **1**(1): p. 1-21.

5. Nakata, K. and A. Fujishima, *TiO_2 photocatalysis: Design and applications.* Journal of Photochemistry and Photobiology C: Photochemistry Reviews, 2012. **13**(3): p. 169-189.

6. Ai, Z., W. Ho, and S. Lee, *Efficient Visible Light Photocatalytic Removal of NO with BiOBr-Graphene Nanocomposites.* The Journal of Physical Chemistry C, 2011. **115**(51): p. 25330-25337.

7. An, H., et al., *Photocatalytic properties of BiOX (X = Cl, Br, and I).* Rare Metals, 2008. **27**(3): p. 243-250.

8. Chen, Y., M. Wen, and Q. Wu, *Stepwise blossoming of BiOBr nanoplate-assembled microflowers and their visible-light photocatalytic activities.* CrystEngComm, 2011. **13**(8): p. 3035-3039.

9. Vadivel, S., et al., *Graphene oxide–BiOBr composite material as highly efficient photocatalyst for degradation of methylene blue and rhodamine-B dyes.* Journal of Water Process Engineering, 2014. **1**: p. 17-26.

10. Zhang, W., Q. Zhang, and F. Dong, *Visible-Light Photocatalytic Removal of NO in Air over BiOX (X = Cl, Br, I) Single-Crystal Nanoplates Prepared at Room Temperature.* Industrial & Engineering Chemistry Research, 2013. **52**(20): p. 6740-6746.

11. Yang, X., et al., *Graphene oxide-iron oxide and reduced graphene oxide-iron oxide hybrid materials for the removal of organic and inorganic pollutants.* RSC Advances, 2012. **2**(23): p. 8821-8826.

12. Du, A., et al., *Hybrid Graphene and Graphitic Carbon Nitride Nanocomposite: Gap Opening, Electron–Hole Puddle, Interfacial Charge Transfer, and Enhanced Visible Light Response.* Journal of the American Chemical Society, 2012. **134**(9): p. 4393-4397.

13. Lee, S.-Y. and S.-J. Park, *TiO_2 photocatalyst for water treatment applications.* Journal of Industrial and Engineering Chemistry, 2013. **19**(6): p. 1761-1769.

14. Honsberg, C. and S. Bowden. *Energy of Photon*. 2015 [cited 2017 January 20]; Available from: http://www.pveducation.org/pvcdrom/properties-of-sunlight/energy-of-photon.

15. Pelaez, M., et al., *A review on the visible light active titanium dioxide photocatalysts for environmental applications.* Applied Catalysis B: Environmental, 2012. **125**: p. 331-349.

16. Kitano, M., et al., *Recent developments in titanium oxide-based photocatalysts.* Applied Catalysis A: General, 2007. **325**(1): p. 1-14.

17. Trapalis, A., et al., *TiO_2/graphene composite photocatalysts for NO_x removal: A comparison of surfactant-stabilized graphene and reduced graphene oxide.* Applied Catalysis B: Environmental, 2016. **180**: p. 637-647.

18. Jafari, T., et al., *Photocatalytic Water Splitting-The Untamed Dream: A Review of Recent Advances.* Molecules, 2016. **21**(7).

19. Zhang, H., et al., *Enhanced Photocatalytic Properties in BiOBr Nanosheets with Dominantly Exposed (102) Facets.* The Journal of Physical Chemistry C, 2014. **118**(26): p. 14662-14669.

20. Kittel, C., *Introduction to Solid State Physics*. 8 ed. October 2004. 704, p.186-208.

21. Shang, M., W. Wang, and L. Zhang, *Preparation of BiOBr lamellar structure with high photocatalytic activity by CTAB as Br source and template.* Journal of Hazardous Materials, 2009. **167**(1–3): p. 803-809.

22. organizations, C.C. *Science of Cool Roofs*. 2001 [cited 2017 January 22]; Available from: http://coolcalifornia.org/science-of-cool-roofs.

23. Yalçın, Y., M. Kılıç, and Z. Çınar, *The Role of Non-Metal Doping in TiO_2 Photocatalysis.* Journal of Advanced Oxidation Technologies, 2010. **13**(3).

24. Chen, J., et al., *Recent progress in enhancing photocatalytic efficiency of TiO_2-based materials.* Applied Catalysis A: General, 2015. **495**: p. 131-140.

25. Marschall, R., *Semiconductor Composites: Strategies for Enhancing Charge Carrier Separation to Improve Photocatalytic Activity.* Advanced Functional Materials, 2014. **24**(17): p. 2421-2440.

26. Wei, M., et al. *Structure and composition study of carbon-doped titanium oxide film combined with first principles*. 2014 [cited 2017 Febuary 10]; Available from: http://jac.tsinghuajournals.com/EN/10.1007/s40145-014-0092-2.

27. Sood, S., et al., *Highly effective Fe-doped TiO_2 nanoparticles photocatalysts for visible-light driven photocatalytic degradation of toxic organic compounds.* Journal of Colloid and Interface Science, 2015. **450**: p. 213-223.

28. Lee, H., et al., *Fe-decorated TiO_2 powder photocatalysts with enhanced visible-light-driven degradation activities.* Surface and Coatings Technology, 2016. **307, Part B**: p. 1018-1023.

29. Fontelles-Carceller, O., et al., *UV and Visible Hydrogen photo-production using Pt promoted Nb-doped TiO_2 photo-catalysts: Interpreting Quantum Efficiency.* Applied Catalysis B: Environmental, 2017.

30. Etacheri, V., et al., *Oxygen Rich Titania: A Dopant Free, High Temperature Stable, and Visible-Light Active Anatase Photocatalyst.* Advanced Functional Materials, 2011. **21**(19): p. 3744-3752.

31. Pang, Y.L., et al., *A critical review on the recent progress of synthesizing techniques and fabrication of TiO_2-based nanotubes photocatalysts.* Applied Catalysis A: General, 2014. **481**: p. 127-142.

32. Hongjun, C. and W. Lianzhou. *Nanostructure sensitization of transition metal oxides for visible-light photocatalysis*. 2014 [cited 2017 April 13]; Available from: http://www.beilsteinjournals.org/bjnano/single/articleFullText.htm?publicId=2190-4286-5-82.

33. Wang, Y., et al., *Synthesis, characterization, and photocatalytic properties of BiOBr catalyst.* Journal of Solid State Chemistry, 2013. **199**: p. 224-229.

34. Liu, Z., et al., *Solvothermal synthesis of BiOBr thin film and its photocatalytic performance.* Applied Surface Science, 2014. **288**: p. 369-372.

35. Cao, J., et al., *Chemical etching preparation of BiOI/BiOBr heterostructures with enhanced photocatalytic properties for organic dye removal.* Chemical Engineering Journal, 2012. **185–186**: p. 91-99.

36. Chang, X., et al., *Photodegradation of Rhodamine B over unexcited semiconductor compounds of BiOCl and BiOBr.* Journal of Colloid and Interface Science, 2012. **377**(1): p. 291-298.

37. Vadivel, S., et al., *Solvothermal synthesis of Sm-doped BiOBr/RGO composite as an efficient photocatalytic material for methyl orange degradation.* Materials Letters, 2014. **128**: p. 287-290.

38. Xu, C., H. Wu, and F.L. Gu, *Efficient adsorption and photocatalytic degradation of Rhodamine B under visible light irradiation over BiOBr/montmorillonite composites.* Journal of Hazardous Materials, 2014. **275**: p. 185-192.

39. Liu, J.-Y., et al., *One-pot synthesis of graphene–BiOBr nanosheets composite for enhanced photocatalytic generation of reactive oxygen species.* Catalysis Communications, 2013. **42**: p. 58-61.

40. Sobon, G., et al., *Graphene oxide vs. reduced graphene oxide as saturable absorbers for Er-doped passively mode-locked fiber laser.* Opt Express, 2012. **20**(17): p. 19463-73.

41. Pei, S. and H.-M. Cheng, *The reduction of graphene oxide.* Carbon, 2012. **50**(9): p. 3210-3228.

42. Graphenea Team. (). . Retrieved , from Web site: . *Reduced Graphene Oxide - What Is It? How Is It Created?* 2016 [cited 2016 December 8]; Available from: http://www.graphenea.com/pages/reduced-graphene-oxide#.WPe1k_nyjDd.

43. Zhao, Z., Y. Sun, and F. Dong, *Graphitic carbon nitride based nanocomposites: a review.* Nanoscale, 2015. **7**(1): p. 15-37.

44. Team, A. *Reduced Graphene Oxide: Properties, Applications and Production Methods*. 2015 [cited 2016 December 8]; Available from: http://www.azonano.com/article.aspx?ArticleID=4041.

45. Dong, G., et al., *A fantastic graphitic carbon nitride (g-C_3N_4) material: Electronic structure, photocatalytic and photoelectronic properties.* Journal of Photochemistry and Photobiology C: Photochemistry Reviews, 2014. **20**: p. 33-50.

46. Patil, S.P., et al., *Facile sonochemical synthesis of BiOBr-graphene oxide nanocomposite with enhanced photocatalytic activity for the degradation of Direct green.* Materials Science in Semiconductor Processing, 2016. **52**: p. 55-61.

47. Ye, L., et al., *Facets coupling of BiOBr-g-C_3N_4 composite photocatalyst for enhanced visible-light-driven photocatalytic activity.* Applied Catalysis B: Environmental, 2013. **142–143**: p. 1-7.

48. Xia, J., et al., *Solvothermal synthesis and enhanced visible-light photocatalytic decontamination of bisphenol A (BPA) by g-C_3N_4/BiOBr heterojunctions.* Materials Science in Semiconductor Processing, 2014. **24**: p. 96-103.

49. Sun, Y., et al., *Growth of BiOBr nanosheets on C3N4 nanosheets to construct two-dimensional nanojunctions with enhanced photoreactivity for NO removal.* Journal of Colloid and Interface Science, 2014. **418**: p. 317-323.

50. Liu, B., et al., *Graphene/MxWO3 (M = Na, K) nanohybrids with excellent electrical properties.* Carbon, 2015. **94**: p. 309-316.

51. Wen, J., et al., *Enhanced visible-light H2 evolution of g-C_3N_4 photocatalysts via the synergetic effect of amorphous NiS and cheap metal-free carbon black nanoparticles as co-catalysts.* Applied Surface Science, 2015. **358**: p. 204-212.

52. Patterson, E.M., C.E. Shelden, and B.H. Stockton, *Kubelka-Munk optical properties of a barium sulfate white reflectance standard.* Applied Optics, 1977. **16**(3): p. 729-732.

53. Ibrahim, A. and S.K.J. Al-Ani, *Models of optical absorption in amorphous semiconductors at the absorption edge — A review and re-evaluation.* Czechoslovak Journal of Physics, 1994. **44**(8): p. 785-797.

APPENDIX

Appendix A

JCPDS card no. 73-2061

Pattern : 01-078-0348 *Radiation =* 1.540600 *Quality :* Calculated

BiOBr

Bismuth Oxide Bromide

Lattice : Tetragonal
S.G. : P4/nmm (129)

a = 3.92330
c = 8.10500

Z = 2

Mol. weight = 304.88
Volume [CD] = 124.75
Dx = 8.116
Dm = 8.082
I/Icor = 14.53

ICSD collection code: 061225
Temperature factor: ATF
Remarks from ICSD/CSD: REM TEM 298.
Data collection flag: Ambient.

Ketterer, J., Kraemer, V., Acta Crystallogr., Sec. C,, volume 42, page 1098 (1986)
Calculated from ICSD using POWD-12++ (1997)

Radiation : CuKa1
Lambda : 1.54060
SS/FOM : F30=1000(0.0001,33)

Filter : Not specified
d-sp : Calculated spacings

2th	i	h	k	l
10.907	425	0	0	1
21.915	73	0	0	2
25.199	251	1	0	1
31.719	999	1	0	2
32.242	482	1	1	0
33.132	32	0	0	3
34.133	31	1	1	1
39.327	108	1	1	2
40.508	8	1	0	3
44.687	46	0	0	4
46.243	194	2	0	0
46.905	76	1	1	3
47.659	30	2	0	1
50.665	120	1	0	4
51.732	24	2	0	2
53.385	55	2	1	1
56.168	112	1	1	4
57.163	288	2	1	2
58.061	24	2	0	3
61.883	26	1	0	5
63.133	3	2	1	3
66.262	47	2	0	4
67.467	49	2	2	0
68.583	8	2	2	1
69.534	19	0	0	6
71.007	70	2	1	4
71.883	8	2	2	2
73.259	9	3	0	1
74.184	13	1	0	6
76.476	51	3	0	2
76.761	62	3	1	0
77.254	10	2	2	3
77.822	6	3	1	1
78.728	40	1	1	6
80.626	21	2	1	5
80.981	17	3	1	2
81.748	1	3	0	3
83.407	2	0	0	7
84.597	20	2	2	4
86.191	18	3	1	3
87.636	33	2	0	6
87.839	18	1	0	7
89.022	16	3	0	4

Appendix B

XRD of pure GO, rGO and g-C_3N_4

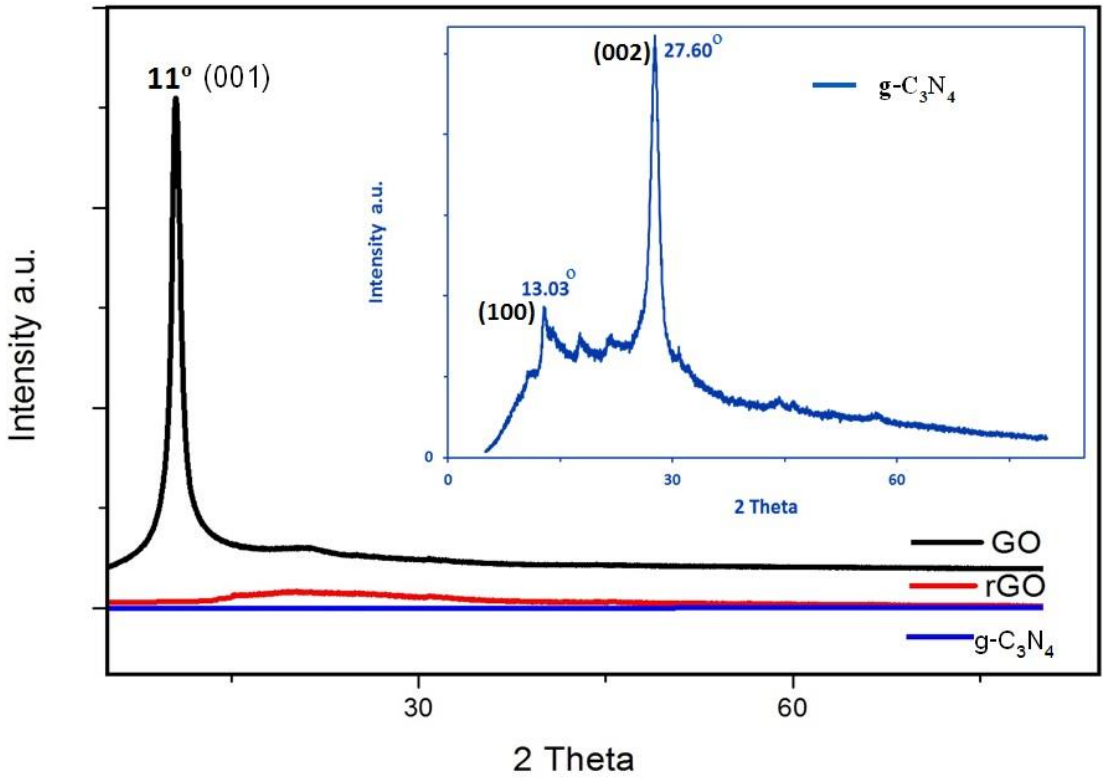

Appendix C

The photocatalytic activities for degradation of Rh-B under visible-light irradiation of pure GO, rGO and g-C_3N_4

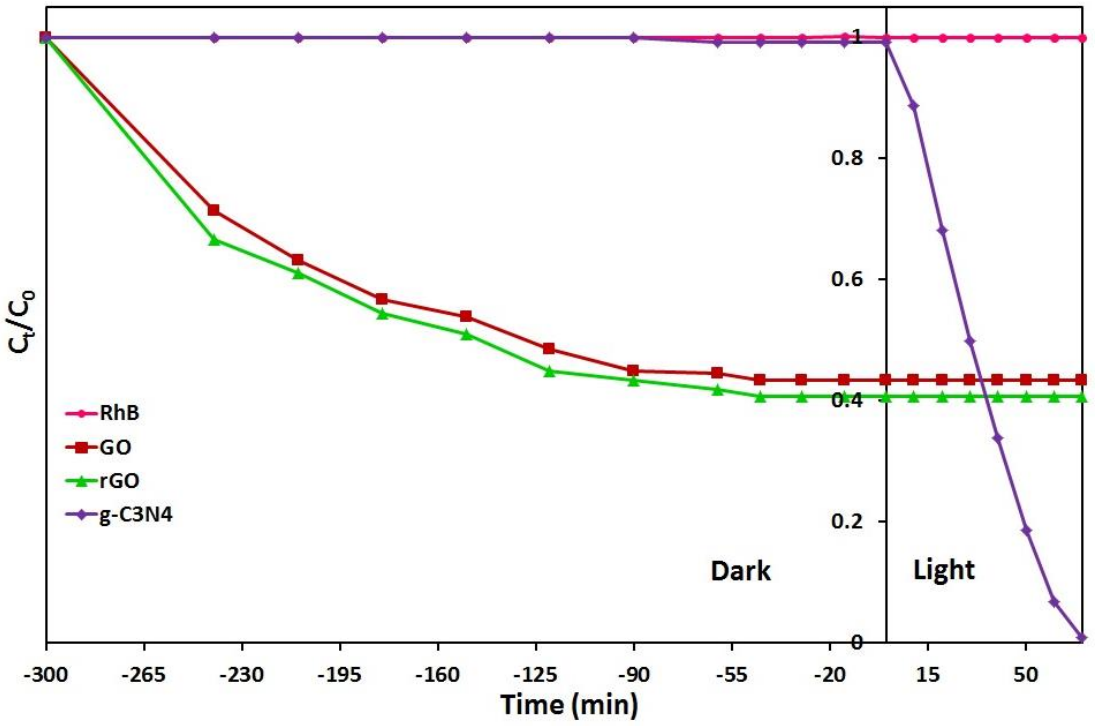

Appendix D

Comparison of Rh-B Degradation efficiency (%) of BiOBr and BiOBr-based composites

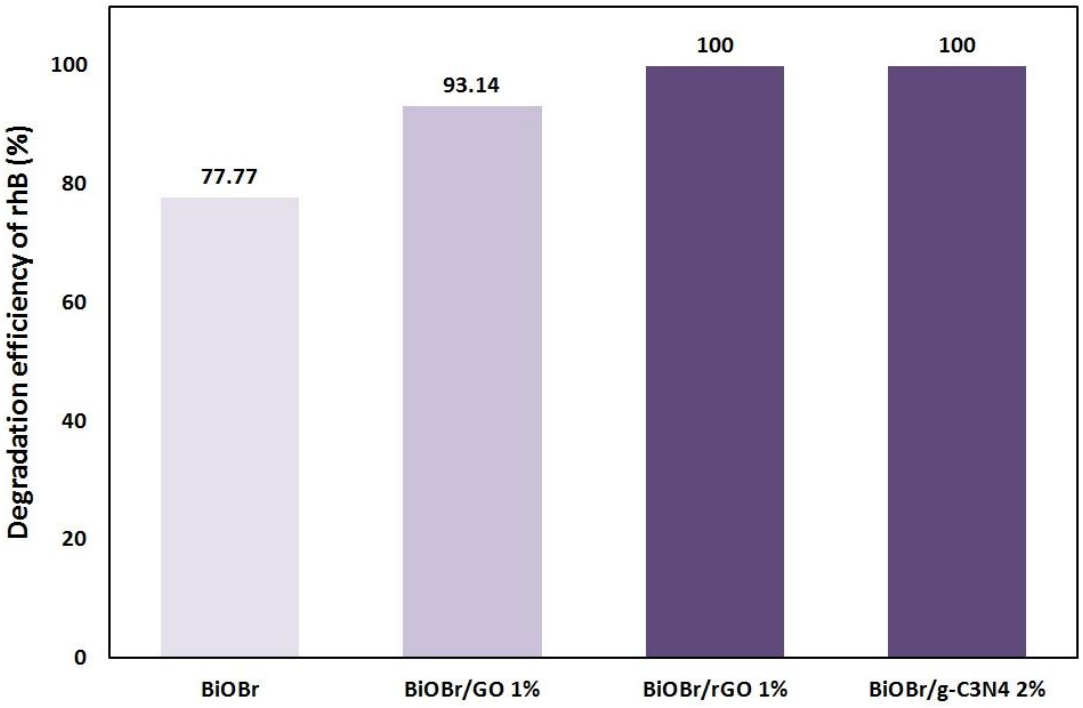

Appendix E

Comparison of NO_x gas Degradation efficiency (%) of BiOBr and BiOBr-based composites

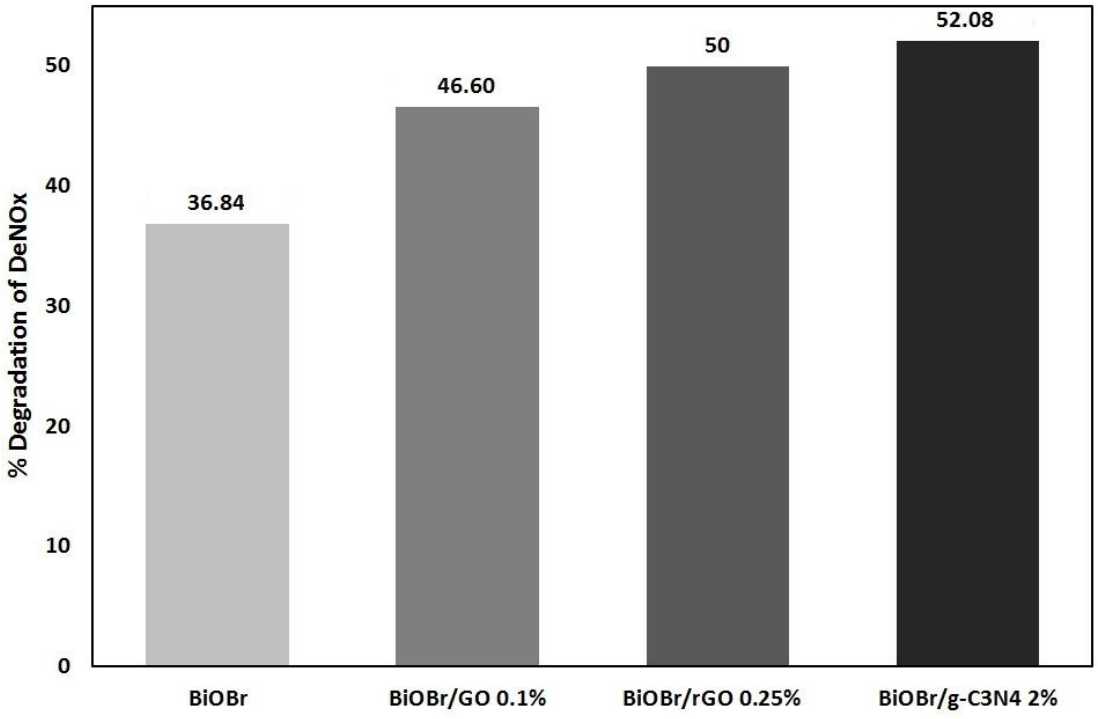

Appendix F

Comparison of reusability for Rh-B decomposition

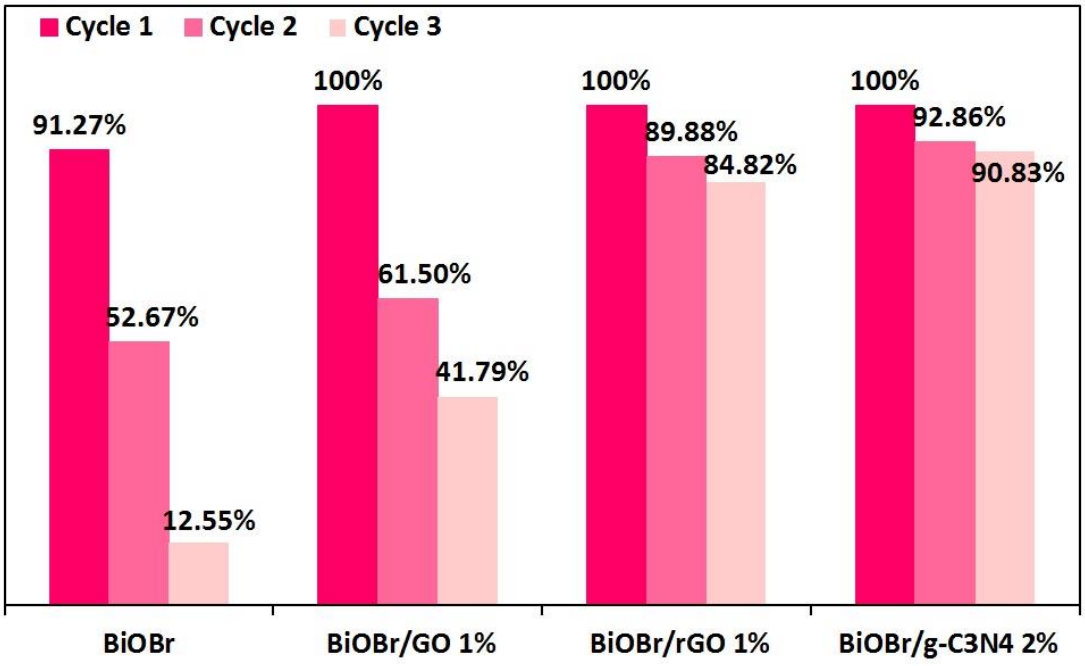

Appendix G

Comparison of reusability for NO_x gas decomposition

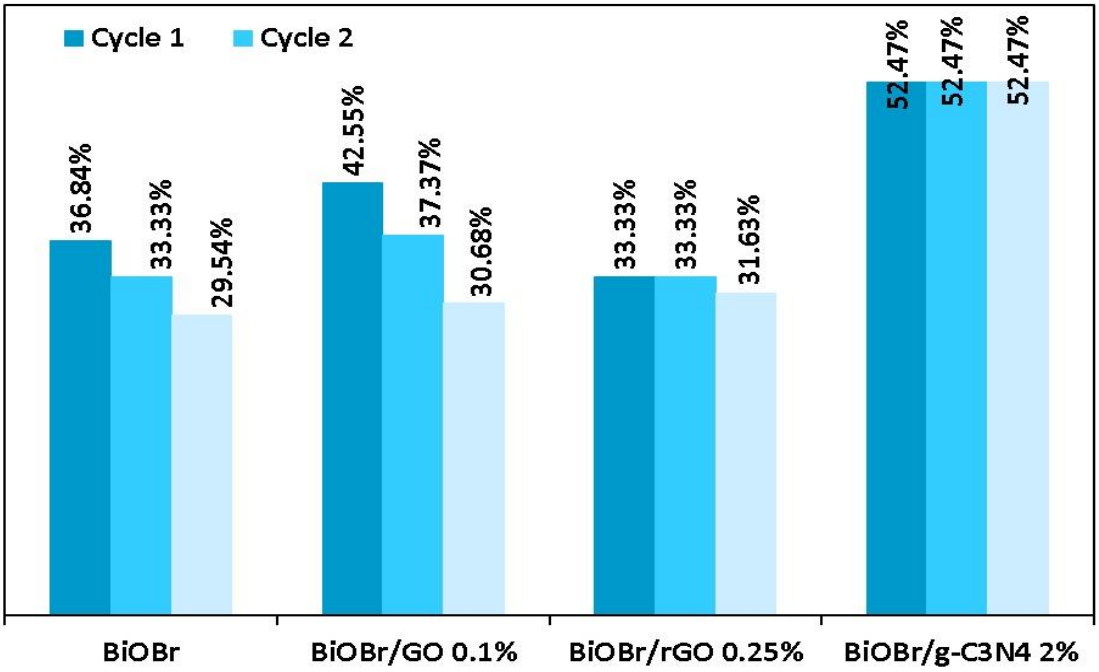

VITA

Miss Tuangphorn Prasitthikun was born in Thailand, Bangkok, on April 23, 1990. She finished her Bachelor's Degree in Materials Science from the Department of Physics, Faculty of Science, Thammasat University. She continued a further study in Master's in the field of Ceramic Technology at Chulalongkorn University and graduated in 2016.

Academic Conference presentation

Prasitthikun T., Wu X. , Sato T., Mongkolkachit C. and Sujaridworakun P. "Room temperature synthesis of visible-light responsive BiOBr and its photocatalytic activity for dye degradation" Pure and Applied Chemistry International Conference (PACCON 2016), Bangkok International Trade and Exhibition Centre (BITEC),Bangkok, Thailand, February 9 –11, 2016. pp 760-764. (Proceeding)

Prasitthikun T., Wu X., Sato T., Mongkolkachit C. and Sujaridworakun P. "Synthesis and Photocatalytic Activity of Visible-Light Responsive BiOBr/GO Composites" International Conference on Materials Science and Technology (MSAT-9), Swissotel Le Concorde Hotel, Bangkok, Thailand, December 14-15, 2016. (Accepted to publish in Key Engineering Materials)

Prasitthikun T., Kiatthanapaiboon W., Chiansirikul W., Mongkolkachit C. and Sujaridworakun P. "Synthesis and Photocatalytic Activity of Visible-Light Responsive BiOBr" International Conference on Advances in Science and Engineering (ICASE-2017), Regent's International College, Bangkok, Thailand, January 21-22, 2017. (Poster presentation; Best presentation award)

Prasitthikun T., Wu X., Sato T., Mongkolkachit C. and Sujaridworakun P. "Synthesis and Characterization of Visible-Light Active BiOBr/GO Composites Photocatalyst" Meiji University – Chulalongkorn University Advanced Material Chemistry Workshop 2017, Chulalongkorn University, Bangkok, Thailand, February 23, 2017. (Poster presentation; Best Poster presentation award)